Optically pumped planar waveguide lasers

Part I: fundamentals and fabrication techniques

C. Grivas

Optoelectronics Research Centre, University of Southampton, SO17 1BJ Southampton, UK

chr.grivas@gmail.com

Abstract: The tremendous interest in the field of waveguide lasers in the past two decades is largely attributed to the geometry of the gain medium, which provides the possibility to store optical energy on a very small dimension in the form of an optical mode. This allows for realization of sources with enhanced optical gain, low lasing threshold, and small footprint and opens up exciting possibilities in the area of integrated optics by facilitating their on-chip integration with different functionalities and highly compact photonic circuits. Moreover, this geometrical concept is compatible with high power diode pumping schemes as it provides exceptional thermal management, minimizing the impact of thermal loading on laser performance. The proliferation of techniques for fabrication and processing capable of producing high optical quality waveguides has greatly contributed to the growth of waveguide lasers from a topic of fundamental research to an area that encompasses a variety of practical applications. In this first part of the review on optically pumped waveguide lasers the properties that distinguish these sources from other classes of lasers will be discussed. Furthermore, the current state-of-the art in terms of fabrication tools used for producing waveguide lasers is reviewed from the aspects of the processes and the materials involved.

1.Introduction

Over the last two decades the field of solid-state planar waveguide lasers has experienced a steady growth, progressing from a laboratory curiosity to an area that demonstrates a broad spectrum of applications, from multiwavelength laser channel arrays for telecommunications to diode-pumped planar structures with multiwatt output powers for sensing and ranging applications. Waveguide lasers are by no means a new field and the first report on such a source dates back in 1961, when laser operation of a waveguide based on an active glass core rod embedded in a low refractive index cladding was demonstrated [1]. However research efforts in the years that followed this report focused primarily on the development of optically pumped laser sources based on high optical quality bulk dielectric laser media in the form of rods and slabs. The merits of the waveguide geometry and the associated optical confinement have been first highlighted in single mode glass optical fibers. Fibers have proven an enabling technology for realization of highly efficient amplifier and laser sources owing to their unrivalled low loss performance and ability to maintain a small spot size and hence high intensities over lengths that are orders of magnitude longer than would normally be allowed by diffraction, [2, 3]. Er-doped fiber amplifiers (EDFAs) in particular have directly contributed to the enormous expansion of the optical communications networks that underpin today's internet infrastructure by allowing for signal regeneration and optical data transmission over long distances. The excellent performance of fiber lasers and amplifiers provided motivation and triggered a major technological interest in their planar analogues, which was initially driven by the prospects of addressing telecom applications, and eventually later applications from a broader spectrum of disciplines. Planar waveguide lasers bridge in a way the gap between solid-state bulk lasers and fiber lasers by combining the best of the two worlds. Unlike bulk lasers, they do not suffer from the trade-off between small spot size and long interaction length, offering the attributes of high gain and

efficient cw performance that characterize fibers; on the other hand, they can attain considerable levels of energy storage, an advantage that is typically conferred by bulk gain media. Furthermore, waveguide geometries allow for easier access to the gain medium, thereby simplifying the addition of extra functionalities to the cavity, such as modulators and gratings.

The combination of enhanced functionality along with the possibility to spatially compress the optical energy and signals has led to the development of small footprint, low threshold laser devices within the reach of modestly powered pump sources, that offer immense scope for on-chip integration in compact and robust packages. The ability to integrate laser sources into a chip scale format is of interest from the perspective of integrated optics since it greatly expands the possibilities for a broad range of applications extending from light-on-chip to lab-on-chip. The main drawback of optically pumped lasers in terms of providing an integrated light source solution is their reliance on external pump lasers for their operation, which prevents them from reaching the ultimate level of integration, that is, a monolithic device requiring no external inputs. However, there is a cost-effective and compact solution to this problem in the existing mature optical pumping technology based on laser diodes.

Another strand of research into these devices is power scaling using diode pumping schemes; the significant advances made in this field were rather unexpected since the small cross-sectional areas of the waveguide cores were initially perceived as being incompatible with high power operation. However, planar waveguide configurations have proven very successful in this respect, ensuring efficient removal of the heat that is generated during laser operation, thereby offering opportunities for full exploitation of the potential of these miniature laser sources in a broad range of applications.

Unlike the electronics industry, where silicon has been the dominant technology platform, photonics is a hybrid technology relying on a broad range of materials and fabrication techniques for producing photonic devices such as waveguide laser sources. For the latter, the need for

improving their performance and functionality and facilitating their interfacing with other components in optical circuits has provided a wealth of opportunities for research into the basic science and development of the underlying capabilities of different fabrication technologies. In fact, the exciting progress made in the field of waveguide lasers has in many respects mirrored advances in fabrication in terms of producing new gain media, establishing new approaches to micro-/nano-structuring and increasing possibilities for hybrid integration.

One of the main challenges in waveguide fabrication with a view to developing laser sources is to maintain the propagation loss in the structures produced at a minimum level since any significant increase would offset the intrinsic benefits offered by the waveguide geometry. Furthermore, any alteration of material properties relevant to laser action is also undesirable as it may compromise the device performance. It is also worth pointing out at this place that each of the available fabrication techniques is not suitable for every class of material and in order to ensure low propagation loss and preserve the intrinsic material properties of the waveguide gain medium the optimum technique has to be identified and applied.

Following the introduction, this review is structured as follows: In Section 2, general principles of waveguiding and parameters that are usually considered when designing waveguide laser sources, such as the numerical aperture and the modal properties, are briefly discussed. Section 3 illustrates the advantages to be gained by implementing planar waveguide geometries for laser cavities in terms of lasing threshold, gain, simplicity of pumping schemes, and efficient thermal management. Discussed are also other useful features of the planar geometry, such as the potential for integration with different functions and photonic circuits and the possibility to tailor both nonlinearity and dispersion in waveguides by suitably choosing their design, which is useful for non-linear frequency conversion devices and mode-locked lasers. Sections 4 and 5 consider possible sources of loss in waveguides and review existing loss measurement techniques, while in

section 6, key waveguide fabrication technologies that are commonly used for development of amplifier and laser sources are presented. Finally, concluding remarks are made in section 7.

2. Waveguide structures

Optical waveguiding is based on Snell's law, which states that light propagating from a medium with a higher refractive index to one with a lower refractive index can be completely reflected by total internal reflection (TIR). The simplest conceivable form of a planar optical waveguide is that with slab geometry; such a structure is composed of a core material that is deposited on a substrate and has its top surface exposed to the surrounding medium. In an alternative configuration of a planar slab waveguide, the core is embedded in-between a substrate and a cladding material, as shown in Fig. 1(a). In these schemes, the core has a higher refractive index (n_2) than the substrate (n_1) and the cladding (n_3) and therefore, any light beam coupled into it through the waveguide end face would be confined in the vertical direction by TIR and propagate along its length maintaining its intensity. To establish a refractive index step, the cladding layer and the substrate are required to have a thickness that exceeds the penetration depth of the evanescent field of the modes that are guided in the core. Depending on whether the refractive index of the cladding layer is equal to or, different than that of the substrate, the index and mode profiles in the waveguide are symmetric or, asymmetric, respectively. Assuming for simplicity a symmetric waveguide with both its cladding and substrate having the same refractive index n_1 [Fig. 1(b)], the critical angle ϕ_c for TIR at the core–cladding interface for a ray of light propagating in the core is given by [4]

$$\varphi_c \geq \varphi = \sin^{-1}\left(n_1 / n_2\right) \tag{1}$$

The reflected ray will subsequently experience successive total internal reflections at the interfaces of the core with the substrate and the cladding layer and hence it will propagate within the core along its length. Applying the Snell's law at the interface of the core with a surrounding medium with a refractive index n_0, for a ray with an angle of incidence θ with respect to the waveguide axis gives

$$\frac{\sin i}{\sin \phi} = \frac{n_2}{n_0} = \frac{\sin i}{\cos \theta} \tag{2}$$

From Eq. (1) and Eq. (2) the condition for this ray to be totally reflected at the core-cladding interface is

$$\sin \theta < \sqrt{1 - \left(n_1 / n_2 \right)^2} \tag{3}$$

Using Eq. (3) in Eq. (2), the condition for TIR is given by the following expression

$$\sin i < \frac{n_2}{n_0} \cdot \sqrt{1 - \left(n_1 / n_2 \right)^2} = \sqrt{n_2^2 - n_1^2 / n_0^2} \tag{4}$$

If $(n_2^2 - n_1^2) \geq n_0^2$ then TIR will occur at the core-cladding interface for any value of the incident angle i. Assuming that the waveguide is surrounded by air and therefore, $n_0 = 1$, the maximum acceptance angle i_m with respect to the waveguide axis for an incident ray to be guided in the core will be given by

$$\sin i_m = \sqrt{n_2^2 - n_1^2} = NA \tag{5}$$

As it becomes evident from the last equation, the sine of the maximum angle of acceptance defines the numerical aperture (NA) of the waveguide, which is an important parameter since it essentially determines the coupling efficiency from a light source. The NA is related to the refractive index contrast Δn between the core and the surrounding material and from Eq. (5), it can be seen that it increases with increasing Δn. High-NA waveguides are particularly suitable for pumping with diode lasers since they can easily capture and confine the fast diverging beams of

these sources. The key waveguide parameters, which determine the size and number of propagation modes at a given wavelength, are its thickness and NA. The number of propagation modes supported by a planar waveguide at a given wavelength λ is given by the quantity p, as defined below, increased to the lowest integer [5]

$$p = \frac{2 \cdot d \cdot NA}{\lambda} \tag{6}$$

The waveguide is characterized as single-moded when $p \leq 1$, that is when its transverse size is equal to, or, smaller than about half of the quantity λ/NA, which yields an approximation for the number of modes in a waveguide without having to resort to any elaborated analysis. In a single-mode waveguide, all propagating modes other than the fundamental will be cut off. From Eq. (6) it also becomes clear that the number of guided modes in a waveguide core with a given thickness, *d,* can be minimized by reducing its NA, which however, has the obvious disadvantage of weakening the light guidance. On the other hand, in waveguides with high NA the thickness required for maintaining single-mode propagation is smaller. The existing waveguide fabrication technologies provide very interesting possibilities to define channel waveguides in different materials. Waveguides with channel geometry ensure confinement in both lateral directions and the different designs that have been used for waveguide lasers are illustrated in Figure 2. They include (a) embedded strips in the substrate material, which can be realized with a number of methods such as thermal ion-indifusion, ion- or, proton exchange, optical (laser) direct writing ion- or, proton implantation, and proton beam writing (b) strip and (c) rib or, ridge waveguides formed by direct etching of the core layer and (d) strip-loaded waveguides whose fabrication involves etching of a cladding layer deposited over the core layer.

3. Advantages of the waveguide geometry

3.1. Lasing Threshold

The two most important performance metrics of a laser are its threshold pump power and the efficiency with which it converts the pump power into laser power once it has reached threshold. There are a number of reports in the literature on theoretical models that have been developed to simulate the operation of longitudinally pumped lasers, predicting their performance with varying degrees of complexity [6-10]. In this section, an analysis is followed [9, 10] in which the key expressions for pump power threshold, slope efficiency, and gain are derived for a waveguide laser and its bulk counterpart by solving the rate equations describing the population-inversion density and the cavity photon number. The rate equations are suitably modified to include Gaussian spatial distributions for the laser and pump beams and the effect of their overlap, while the effect of re-absorption loss at the laser wavelength as a result of thermally induced population in (quasi-) three-level laser systems is also taken into account. Since the model is described in detail in the respective papers, in the remainder of this section the analytical expressions for the key laser parameters that have been derived will only be presented and used to discuss the advantage of employing waveguides geometries; starting from the absorbed pump power threshold, it can be estimated by

$$P_{th}(b) = \frac{\pi \cdot h \cdot \nu_p \cdot [\overline{w_{P,bulk}^2} + \overline{w_{L,bulk}^2}]}{4 \cdot \sigma_e \cdot f \cdot \tau \cdot [1 - \exp(-\alpha_p \cdot l)]} \cdot (L_{bulk} + T + 2 \cdot N_1^0 \cdot \sigma_\alpha \cdot l) \qquad (7)$$

Here the parameters are as follows: h is the Planck's constant, ν_p is the frequency of the pump irradiation, σ_e is the laser emission cross section, τ is the upper laser level lifetime, $f = f_1 + f_2$, with f_1 and f_2 being the fractions of the populations of the upper and lower laser level manifolds, of the corresponding Stark-levels, respectively, and $[1-\exp(-\alpha_p \cdot l)]$ is the absorption efficiency of the launched pump light, with a_p being the absorption coefficient of the pump beam in the gain medium. In the last term in Eq. (7), $L_{bulk} = 2 \cdot \alpha_L \cdot l$ is the intracavity round trip loss

exponent with α_L being the propagation loss coefficient, T is the natural logarithm of the reflectivity of the outcoupling mirror at the laser wavelength, while the product $2 \cdot N_1^0 \cdot \sigma_a \cdot l$ stands for the re-absorption loss with N_1^0, σ_a, and l being correspondingly the equilibrium population density of the lower laser level, the absorption cross section and the length of the gain medium. The re-absorption loss is relevant to (quasi)-three-level laser systems and enters the expression for the pump power threshold as an additional cavity loss. Since bulk lasers are restricted to the use of focused pump laser light, diffraction effects of the pump and laser beams have to be taken into account; therefore, the average pump and laser spot sizes $\overline{w_{P,bulk}}$ and $\overline{w_{L,bulk}}$, respectively, have been introduced in Eq. (7). The optimal pumping configuration for minimizing $\overline{w_{P,bulk}}$ and $\overline{w_{L,bulk}}$ and maximizing their overlap in the gain medium requires slightly tighter focusing than confocal. The Rayleigh length of the focused pump beam should ideally be equal to the waveguide length, in which case its beam waist radius can be expressed as [11]

$$w_0 = \sqrt{\lambda_{P(L)} \cdot l \Big/ 2 \cdot \sqrt{3} \cdot \pi \cdot n} \tag{8}$$

where $\lambda_{P(L)}$ is the pump (laser) wavelength and n is the refractive index of the laser medium. Assuming such a pumping configuration, the pump (laser) spot size radius averaged over the gain medium will then be given by [11]

$$\overline{w_{P(L),bulk}} = \sqrt{\lambda_{P(L)} \cdot l \Big/ \sqrt{3} \cdot \pi \cdot n} \tag{9}$$

Using Eq. (9) into Eq. (7), the following expression is obtained for the threshold of the bulk laser

$$P_{th}(b) = \frac{l \cdot h \cdot \nu_p \cdot [\lambda_P + \lambda_L]}{4 \cdot \sqrt{3} \cdot \sigma_e \cdot f \cdot \tau \cdot n \cdot [1 - \exp(-\alpha_p \cdot l)]} \cdot (L_{bulk} + T + 2 \cdot N_1^0 \cdot \sigma_\alpha \cdot l) \tag{10}$$

For longitudinally pumped slab and channel waveguide lasers, the corresponding to Eq. (7) analytical expressions for the absorbed pump power threshold are the following, respectively,

$$P_{th}(sl)=\frac{\pi\cdot h\cdot v_p\cdot[(\overline{w_{PX}}^2+\overline{w_{LX}}^2)^{1/2}\cdot(w_{PY}^2+w_{LY}^2)^{1/2}]}{4\cdot\sigma_e\cdot f\cdot\tau\cdot[1-\exp(-\alpha_p\cdot l)]}\cdot(L_{sl}+T+2\cdot N_1^0\cdot\sigma_\alpha\cdot l) \tag{11}$$

$$P_{th}(ch)=\frac{\pi\cdot h\cdot v_p\cdot[(w_{PX}^2+w_{LX}^2)^{1/2}\cdot(w_{PY}^2+w_{LY}^2)^{1/2}]}{4\cdot\sigma_e\cdot f\cdot\tau\cdot[1-\exp(-\alpha_p\cdot l)]}\cdot(L_{ch}+T+2\cdot N_1^0\cdot\sigma_\alpha\cdot l) \tag{12}$$

where, L_{bulk}, L_{sl}, and L_{ch} correspond to the round trip loss in bulk, slab waveguide, and channel waveguide cavities, and w refer to the $1/e^2$ intensity radii for the pump (P) and laser (L) modes in the horizontal (X) and vertical (Y) planes. Here, one notes that for slab waveguides in Eq. (11), the average values $\overline{w_{PX}}$ and $\overline{w_{LY}}$ have been used for the pump and laser spot sizes, respectively, in the horizontal, unguided direction; they can be both estimated from Eq. (9).

In three-level laser systems re-absorption loss is significantly high compared to propagation loss, and therefore, the effect of L_{bulk}, L_{sl}, and L_{ch} on the corresponding laser thresholds is negligible. The ratios of pump power thresholds of the slab and channel waveguide lasers to that of the bulk laser can be obtained by diving Eq. (11) and Eq. (12) by Eq. (10), respectively,

$$\frac{P_{th}(sl)}{P_{th}(b)}=\left[\frac{\sqrt{3\cdot\pi\cdot n}}{l\cdot(\lambda_P+\lambda_L)}\right]^{1/2}\cdot(w_{PY}^2+w_{LY}^2)^{1/2} \tag{13}$$

$$\frac{P_{th}(ch)}{P_{th}(b)}=\frac{\sqrt{3}\cdot\pi\cdot n\cdot[(w_{PX}^2+w_{LX}^2)^{1/2}\cdot(w_{PY}^2+w_{LY}^2)^{1/2}]}{l\cdot(\lambda_P+\lambda_L)} \tag{14}$$

Similar expressions can be derived for four-level laser systems by setting the re-absorption loss term in Eqs. (10), (11) and (12) to zero

$$\frac{P_{th}(sl)}{P_{th}(b)}=\left[\frac{\sqrt{3\cdot\pi\cdot n}}{l\cdot(\lambda_P+\lambda_L)}\right]^{1/2}\cdot(w_{PY}^2+w_{LY}^2)^{1/2}\cdot\left[\frac{L_{sl}+T}{L_b+T}\right] \tag{15}$$

$$\frac{P_{th}(ch)}{P_{th}(b)}=\frac{\sqrt{3}\cdot\pi\cdot n\cdot[(w_{PX}^2+w_{LX}^2)^{1/2}\cdot(w_{PY}^2+w_{LY}^2)^{1/2}]}{l\cdot(\lambda_P+\lambda_L)}\cdot\left[\frac{L_{ch}+T}{L_b+T}\right] \tag{16}$$

From Eqs. (13) - (16), it is clear that waveguide geometries have an advantage over bulk in terms of low lasing threshold as they can ensure tight confinement of both the pump and laser beam. In this respect, channels waveguides are clearly superior to their slab counterparts since they provide confinement in two dimensions allowing for larger threshold reductions. The advantage in terms of low laser threshold increases with increasing waveguide length and decreasing pump and laser beam spot sizes and is more evident for (quasi)-three-level laser systems. In contrast, in four-level lasers, due to the absence of reabsorption loss in their gain media, propagation loss could become an issue for planar waveguides only in cases when their fabrication introduces significant loss with respect to the corresponding bulk material. This extra loss, which is higher in channel waveguides than in their slab counterparts because of the larger number of fabrication steps required for their realization, can compromise or even outweigh their potential to provide low lasing thresholds and therefore, it should be minimized in order to optimize laser operation.

3.2. Slope efficiency

The slope efficiency η, of a waveguide laser describes the conversion efficiency of the input (absorbed) pump power into output signal power. Taking into account potential reabsorption loss in the cavity an expression derived for η is [9]

$$\eta = \left(\frac{T}{T+L}\right)\cdot\left(\frac{\nu_L}{\nu_P}\right)\cdot\left[1-\exp\left(a_p\cdot l\right)\right]\cdot\left(\frac{dS}{dF}\right) \tag{17}$$

In the last equation the new term is dS/dF, which is a quantity that indicates the conversion efficiency of the pump light. It strongly depends on reabsorption losses and the overlap, η_{PL} of the pump with the laser mode, which is given by [12]

$$\eta_{PL} = \frac{w_{lx}\cdot w_{ly}\cdot(2w_{px}^2+w_{lx}^2)^{1/2}\cdot(2w_{py}^2+w_{ly}^2)^{1/2}}{(w_{px}^2+w_{lx}^2)\cdot(w_{py}^2+w_{ly}^2)} \tag{18}$$

From Eq. (17) it becomes evident that waveguide lasers are generally expected to yield lower slope efficiencies than the corresponding bulk systems since they exhibit higher propagation losses. Similar slope efficiencies for both laser systems can be achieved by using outcoupling mirrors with higher transmission to form the waveguide cavity, which however, according to Eqs. (11) and (12), would be at the cost of an increased pump power threshold. Here, one notes that the effect of loss on slope efficiency can be to a certain extend compensated by the waveguide geometry, which ensures high overlap efficiencies of the pump and laser beams compared to an unguided configuration. Since channel waveguide lasers have higher overlap efficiencies than their slab waveguide and bulk counterparts, it follows that if all three systems have the same level of loss, sources based on channel geometries are expected to exhibit comparable slope efficiencies with the other two types of lasers but lower lasing thresholds. As an example to illustrate this fact the laser characteristics of two Ti:sapphire waveguide lasers with slab and channel geometry, respectively, with similar levels of loss are shown in Fig. 3. As it becomes clear from the plot, for about the same outcoupling level both lasers exhibit similar slope efficiencies however, the observed threshold for the channel waveguide laser is half that of its planar counterpart. Whilst, for fundamental mode laser operation the overlap efficiencies that can be achieved in bulk slab or rod lasers approach 0.5 and 0.36, respectively [15], in waveguide lasers the corresponding value is considerably higher and for channel geometries can even reach unity.

3.3. Gain

To demonstrate the potential of a waveguide gain medium to provide higher gain than its bulk counterpart in the following the small signal gain expressions for both systems are derived and compared. Assuming a Gaussian signal beam that is perfectly aligned with the pumped region and taking into account that the condition for lasing is for the gain to compensate the cavity

losses occurring during each round trip by replacing the loss terms in Eqs. (7), (11) and (12) with the corresponding small signal gain $\ln(G_0^{(bulk)})$ and $\ln(G_0^{(sl)})$, and $\ln(G_0^{(sl)})$ for the bulk and the slab and channel waveguide gain media the following expressions can be obtained correspondingly

$$\ln\left(G_0^b\right)=\frac{2\cdot\sqrt{3}\cdot\sigma_e\cdot\tau\cdot n\cdot P_{in}\cdot[1-\exp(-\alpha_p\cdot l)]}{l\cdot h\cdot v_p\cdot(\lambda_p+\lambda_l)} \tag{19}$$

$$\ln(G_0^{(sl)})=\frac{2\cdot\sigma_e\cdot\tau\cdot P_{in}\cdot[1-\exp(-\alpha_p\cdot l)]}{\pi\cdot h\cdot v_p}\cdot\frac{1}{(w_{PY}^2+w_{LY}^2)^{1/2}}\cdot\left(\frac{\sqrt{3}\cdot\pi\cdot n}{l\cdot(\lambda_P+\lambda_L)}\right)^{1/2} \tag{20}$$

$$\ln(G_0^{(ch)})=\frac{2\cdot\sigma_e\cdot\tau\cdot P_{in}\cdot[1-\exp(-\alpha_p\cdot l)]}{\pi\cdot h\cdot v_p}\cdot\frac{1}{(w_{PX}^2+w_{LX}^2)^{1/2}\cdot(w_{PY}^2+w_{LY}^2)^{1/2}} \tag{21}$$

In Eqs. (19) - (21) the term $P_{in}\cdot[1-\exp(-\alpha_p\cdot l)]$ is the absorbed pump power with P_{in} being the power of the launched pump light. Dividing Eqs. (20), and (21) by Eq. (19) provides the ratios of the small signal gain of the slab and channel waveguide to that of the bulk laser, respectively,

$$\frac{\ln(G_0^{(sl)})}{\ln(G_0^{(b)})}=\frac{l\cdot(\lambda_P+\lambda_L)}{\sqrt{3}\cdot\pi\cdot n}\cdot\frac{1}{(w_{PY}^2+w_{LY}^2)^{1/2}} \tag{22}$$

$$\frac{\ln(G_0^{(ch)})}{\ln(G_0^{(b)})}=\frac{l\cdot(\lambda_P+\lambda_L)}{\sqrt{3}\cdot\pi\cdot n}\cdot\frac{1}{(w_{PX}^2+w_{LX}^2)^{1/2}\cdot(w_{PY}^2+w_{LY}^2)^{1/2}} \tag{23}$$

The last two equations indicate that the optical confinement in one or two planes that can be achieved in waveguides with slab or channel geometry, respectively, provides linear (slab) or quadratic (channel) enhancement of the small signal gain with respect to that obtained from an unguided configuration. It becomes also evident that this enhancement scales with the length of the gain medium.

3.4. Thermal management

Progress in scaling the output power from waveguide lasers has been facilitated by the use of high-power diode lasers for pumping. In-plane pumping schemes (end- or side-pumping) are inherently compatible with high power laser-diode bars and stacks, due to the good beam quality of these sources in the fast axis and the excellent match of their cross sections to the profile of planar waveguides. This eases the need for shaping of the pump beam, and for waveguides with high NA it allows implementation of efficient coupling designs involving simple focusing optics or, even proximity coupling [16]. In contrast to fiber lasers, where the thermal limit for power scaling is usually determined by the onset of damage due to the increase in temperature, in bulk lasers, power limitations originate from the development of temperature gradients in the laser medium. They are induced by the non-uniform deposition of heat from the diode pump laser and the propagation of that heat through the gain medium to the heat sink. The severity of this effect depends on a number of factors, including thermo-mechanical, thermo-optical properties and geometry of the laser medium, pump deposition profile, cavity configuration, and heat-sinking arrangements [17]. Heat itself results from the quantum defect of the pumping cycle, q, which is defined as the energy difference of the pump photons with the laser photons

$$q = \left(h \cdot \nu_p - h \cdot \nu_L\right) \tag{24}$$

This energy loss and the associated temperature rise produce an unwanted feedback by reducing the thermal conductivity of the gain medium, which in turn leads to a further increase in the amount of the heat deposited. The latter can trigger various thermo-optical effects in the gain medium such as thermal lensing, thermal-stress-induced birefringence, and fracture, which have a detrimental effect on laser operation. Thermal lensing is related to the variation of the refractive index of the gain medium with the temperature (dn / dT), and results in tighter or weaker mode confinement if, $dn / dT > 0$ or, $dn / dT < 0$, respectively. Under normal operating conditions, index guidance is the prevailing waveguiding mechanism. However, with increasing pump power

a level is eventually reached when the temperature gradients in the laser medium become significant and thermal guiding dominates over index guiding. The effect of thermal guiding has been recently highlighted with the demonstration of a thermal-induced refractive index planar slab waveguide laser emitting 23.1 W of optical power for a pump power of 50 W, which corresponds to an optical-to-optical conversion efficiency of 46% [18]. Thermal guiding leads in general to a decrease in the fundamental mode size and in turn to excitation of higher order modes and degradation in the quality of the laser beam. Whilst in high-power solid-state bulk lasers cooling systems that are costly, complex, and large in size, are required to mitigate these effects, in planar waveguide lasers they can be alleviated by virtue of their geometry.

The effect of the waveguide geometry in this respect can be appreciated by deriving the upper limit for the thermal power density Q_{max} at which thermal lensing starts having an impact on laser performance. For a waveguide core with a step index profile and a uniform rare earth ion doping distribution the following expression is derived for Q_{max} [19, 20]

$$Q_{\max} = \frac{k \cdot \lambda^2 \cdot \pi^2}{n \cdot \left(dn/dT\right) \cdot d^4} \tag{25}$$

where k, and d are the thermal conductivity and the waveguide thickness, respectively. In the last equation, it was assumed that index guidance would dominate over thermal lensing as long as the propagating mode is smaller than that of the thermal guide. Since Q_{max} in Eq. (25) scales with the inverse power to the four on the thickness of the gain medium, it becomes clear that thin slab waveguides have a higher thermal limit for the onset of thermal lensing than their bulk counterparts. One further issue when moving to higher pump powers is the appearance of differential thermal expansion and in turn of thermal stress in the gain medium. Thermal stress deteriorates the laser performance by introducing birefringence in the gain medium and may even cause its fracture if a certain pump power level is exceeded. Based on an analysis on thermal effects in uniformly heated bulk laser media with slab and rod geometries the limit for Q_{max}

before the onset of surface stress fracture can be estimated by the following expressions, respectively, [21]

$$Q_{\max}^{slab} = \left(\frac{12 \cdot R_S}{d^2} \right) \tag{26}$$

$$Q_{\max}^{rod} = \left(\frac{8 \cdot R_S}{d^2} \right) \tag{27}$$

where R_s is the thermal stress resistance of the gain medium. From the last two equations, it becomes clear that bulk slabs can withstand higher thermal loads than rods before the stress fracture sets in. Therefore, the slab geometry is more suitable for pumping with high-power diode lasers and for this reason it is preferred for (quasi)-three-level bulk laser systems that require pumping with high intensities. Planar slab waveguides can be considered as an extreme case of the slab geometry with a small thickness *d*, and therefore have a significantly higher fracture limit when compared to bulk slab systems.

The excellent thermal management properties that characterize planar waveguides by virtue of their large aspect ratio can be appreciated by comparing the maximum temperature rise, $\Delta T_{\max}$ that is induced during laser operation in the waveguide gain medium with that in the bulk. $\Delta T_{\max}$, has been calculated for an optically pumped YAG:Yb^{3+} bulk slab crystal using the diffusion model of the heat flow [22]. The assumptions made were first, that the profile of the pump beam is approximately flat in the horizontal direction, and fills the full width *w* of the slab and second, that its extension in the vertical direction is considerably smaller than the slab thickness *d*. In this case, the dependence of $\Delta T_{\max}$ on pump power P_p can be calculated by [22]

$$\Delta T_{\max} = \frac{\eta_{\mathrm{h}} \cdot \eta_a \cdot \mathrm{P_P} \cdot d}{2 \cdot K_c \cdot l \cdot w} \tag{28}$$

where K_c is the thermal conductivity, η_h is the heat conversion efficiency, and η_a is the absorption efficiency. For this calculation it was assumed that $K_c = 0.14$ W/cm·K, $l = 50$ mm, $\eta_a = 0.85$, and $\eta_h = 0.087$. In Fig. 4, ΔT_{max} is plotted as a function of P_p for several width-to-thickness *(w/d)*

ratios, assuming a constant value for the cross section of the slab of $S = w \cdot d = 2$ mm. It becomes clear that ΔT_{max} decreases with decreasing d, that is when moving from bulk to planar slab waveguides; in the latter there is effectively an one-dimensional heat flow, since heat only needs to pass through a very thin layer of high thermal impedance before reaching the heat sink. This highlights the favorable effect of the large cooling-surface-area-to-volume ratio in waveguides in terms of enabling efficient heat removal from the pumped region and maintaining the temperature rise in the gain medium at a manageable level during laser operation, thereby allowing power scaling.

3.5. Nonlinear optical devices

Since many nonlinear optical effects including, nonlinear frequency conversion, parametric amplification and oscillation, sum and difference frequency generation, frequency doubling and four-wave mixing have an intensity dependence that can be quadratic or even of higher order, maintaining high intensities over long distances can have a strong impact on the nonlinearities of the material. By virtue of their geometry, waveguides are capable of dramatically enhancing nonlinear interactions, which can be triggered at low pump powers compared to the same interactions in the bulk, allowing for use of readily available laser diodes as pump sources. Nonlinear waveguides, based on dielectric materials such as periodically-poled lithium niobate ($LiNbO_3$) [23], lithium tantalate ($LiTaO_3$) [24], potassium titanyl phosphate ($KTiOPO_4$) [25] and semiconductors such as periodically-reversed GaAs [26-28] can provide frequency conversion over the entire transparency range of the host, spanning from 350 nm to 4.5 μm, by utilizing quasi-phase matching (QPM) [29, 30]. Coupling of the periodically poled/reversed waveguides to IR semiconductor diode lasers allows generation of blue–green coherent radiation by nonlinear wavelength conversion, which is useful for optical data storage, color printing, medical applications, and displays requiring higher powers and longer wavelengths than those produced

by InGaN diodes [31]. Advances in the technology of periodic poling enabled integration of different types of waveguide lasers with quasi-phase-matched nonlinear frequency converters even in the same waveguide structure as exemplified by the self-frequency doubling lasers reported in the literature [32, 33]. The advantage of waveguides in enhancing nonlinear interactions can be appreciated by comparing the efficiencies for second harmonic generation (SHG) that can be achieved in a QPM waveguide and in the corresponding bulk material. For a waveguide the conversion efficiency η_{wg}, can be estimated from [34]

$$\eta_{wg} = \frac{P_{2\omega}(l)}{P_{\omega}(0)} \propto \frac{d_{eff}^2 \cdot l^2 \cdot P_{\omega}(0)}{n_{\omega}^2 \cdot n_{2\omega} \cdot A_{eff}} \tag{29}$$

where, $P_{\omega}(0)$ and $P_{2\omega}(L)$ are the incident and the generated second harmonic power, respectively, d_{eff} is the effective nonlinear coefficient, l is the waveguide length, while n_{ω} and $n_{2\omega}$ are the effective refractive indices of the transverse mode at the fundamental and the second harmonic frequencies, respectively. The term A_{eff} in Eq. (29) represents the effective interaction area between the fundamental and second harmonic modes and depends on their actual spot sizes and overlap. A similar expression for the conversion efficiency from fundamental to second harmonic is valid for the bulk material with the only difference being that the term A_{eff} in Eq. (29), should be replaced by the spot size of the pump beam. In this case the diffraction behavior of the unguided pump beam should be considered, for which the optimum focusing for maximum enhancement of the nonlinear interactions is somewhat tighter than confocal focusing, with the spot size of the pumping beam at the ends of the medium being $\sqrt{2}$ times that at the centre [35]. This condition is satisfied if the focused beam spot size is $W_{bulk} \sim \lambda \cdot l/2 \cdot n$. Since the generated second harmonic power is inversely proportional to the beam spot size, it follows that the conversion efficiency η_b in the bulk would only scale linearly with the interaction length. A convenient way to present the enhancement of SHG is to estimate the ratio of the conversion efficiencies in a waveguide η_{wg} and in its bulk counterpart η_b

$$\frac{\eta_{wg}}{\eta_b} = \frac{W_{bulk}(l)}{A_{eff}} \propto \frac{\lambda \cdot l \cdot}{2 \cdot n \cdot A_{eff}} \tag{30}$$

In the last equation it can be seen that the enhancement conferred by a waveguide geometry, increases with increasing interaction length and decreasing A_{eff} (and hence increasing optical intensity). Assuming a value of 30 μm^2 for the A_{eff} and a length of l = 1 cm for both the QPM waveguide and the bulk crystal an efficiency improvement of two orders of magnitude can be derived from Eq. (30). The same efficiency for frequency doubling in bulk nonlinear crystals can only be achieved by using significantly higher input powers. Figure 5 shows a SHG tuning curve as obtained from a periodically-poled, QPM $LiNbO_3$ channel waveguide, exhibiting propagation loss of less than 1 $dB \cdot cm^{-1}$ by pumping at 1.55 μm. The peak normalized second-harmonic conversion efficiency obtained exceeded 150%/W-cm^2 [36], a value that is several orders of magnitude larger than those typically obtained in bulk media.

Another notable example of the benefit of using a waveguide geometry for nonlinear optical devices is the recent demonstration of parametric frequency comb generation in chip-size optical parametric oscillators (OPOs) based on silicon nitride ring resonators [37] (Fig. 6a), and doped high-index silicon dioxide ring resonators [38]. Because of inversion symmetry in these materials, the parametric gain and frequency conversion were provided through four-wave mixing (FWM), thereby exploiting the $\chi^{(3)}$ nonlinearity of these materials. Oscillation based on parametric gain requires phase matching, which is determined by the frequency detuning $\Delta\omega = 2\omega_p - \omega_S - \omega_I$, where ω refer to the frequency of the pump (p), signal (s), and idler (i). $\Delta\omega$ indicates the irregularity in the spacing of resonant frequencies due to both cavity and material dispersion, and for achieving phase-matching it should not exceed the parametric gain bandwidth Ω given by [39]

$$\Omega = \frac{4 \cdot c \cdot \gamma \cdot P}{n} \tag{31}$$

where n is the refractive index, c is the speed of light, P is the circulating power within the ring resonator and γ is the waveguide nonlinear parameter, which can be expressed as

$$\gamma = \frac{\omega_p \cdot n_2}{c \cdot A_{eff}}$$

(32)

where n_2 is the non-linear refractive index. The waveguide geometry is critical to the successful operation of these OPO sources in two ways. First, the small modal effective areas A_{eff}, of the ring waveguides that can be achieved because of the enhanced index contrast with the substrate increase their nonlinear parameter, γ, and in turn the gain bandwidth, Ω. Second, the waveguide design provides a convenient mean to engineering anomalous dispersion (in particular with flattened profile, exhibiting near zero-dispersion at the pump wavelength) that is necessary to reduce $\Delta\omega$ and achieve phase matching. Tuning the pump wavelength to a cavity resonance in the anomalous dispersion regime near the zero-dispersion wavelength and increasing the pump power allows, for broad-bandwidth phase matching and hence generation of simultaneous parametric oscillations at a number of equally spaced wavelengths through cascaded FWM in the ring (Fig. 6b). Minimizing the power demands for nonlinear interactions is of outmost importance for the development of all-optical devices. The theoretical value for parametric oscillation threshold is

$$P_{th} = 2 \cdot \pi^2 \cdot n^2 \cdot \frac{D \cdot A_{eff}}{\lambda \cdot n_2 \cdot Q^2} \tag{33}$$

The high transverse optical confinement of the ring waveguides in combination with the high optical quality factor, Q, of the ring microresonator significantly reduced the pump power required for the FWM process, allowing OPO operation above a pump threshold of only a few milliwatts.

As well as demonstrating low power frequency conversion, the capability to control the nonlinear and dispersive properties of the waveguides can also been exploited for generation of

laser pulses of short duration through soliton mode-locking and phase matching. Recently, generation of subpicosecond pulses at 200 GHz-repetition rate has been reported in a passively mode-locked Er-doped fiber laser, whose operation was based on high-harmonic FWM in a high-Q nonlinear planar ring resonator integrated in the cavity [40].

3.6. Potential for integration

The low-threshold $\chi^{(3)}$ OPOs described in the previous paragraph represent an excellent example of the device miniaturization that can be achieved by exploiting waveguide geometries and sets conveniently the context for the discussion in this paragraph on the integreability of chip-scale waveguide laser cavities. Integrated light sources are vital parts of optical circuits and have an important impact on practical applications. Therefore, in addition to work targeting at waveguide lasers as discrete elements, there has also been considerable research activity in integrated versions of these sources. Combining the latter with different optical functions, such as Q-switching and mode-locking, feedback gratings, nonlinear conversion devices, mode-control, and tuning or frequency selecting elements on the same substrate, has led to the demonstration of sophisticated miniature devices.

Although it is most desirable to build integrated circuits from a single material, in practice no material system can effectively offer full passive and active functionality on the same chip. Hybrid integration, in which a material is used as a platform to accommodate different materials that excel in providing the functionalities envisaged, has emerged as a monolithic solution for photonic chips. An important parameter in choosing suitable waveguide material-substrate pairs is their refractive index contrast, since it determines the device footprint and the overall dimensions of the photonic integrated circuit. Silicon-on-insulator (SOI) is one of the most attractive systems for all-optical devices because of its compatibility with the complementary metal oxide semiconductor (CMOS) fabrication technology and the high-index contrast between

the silicon (*n=3.5*) core, and the silica (*n=1.45*) (that is usually employed as a substrate and cladding), allowing for strong optical confinement and large effective nonlinearities. Despite the lack of efficient optical transitions in materials with indirect band gap structure and hence their limited potential as laser media, important progress has been made with silicon Raman lasers using waveguide ring-type resonators. Although these devices are not fully optimized, their realization strengthens the prospects for fully functional on-chip integration [41-43].

Silica-on-silicon is another extremely versatile platform for integrated optics offering the attractions of CMOS-compatibility and proximity of the silica core refractive index to that of optical fibers, allowing for low loss fiber-chip coupling. The high refractive index of silicon represents a difficulty when this material is used as a substrate for waveguides, however, this problem can be avoided by applying a SiO_2 buffer layer between the substrate and the device. One example of an integrated source based on this material system is the femtosecond waveguide laser shown in Fig. 7, which can generate 440 fs pulses at a repetition rate of 394 MHz [44]. The approach followed for its realization was to combine waveguides with normal and anomalous dispersion within the laser cavity for obtaining net anomalous intracavity dispersion, which is required for soliton mode-locking. This eases the dependence on the dispersive contribution of the saturable Bragg reflector (SBR) and hence the requirement to predict the lasing wavelength precisely enough to engineer an SBR device with the appropriate characteristics for a specific target repetition rate.

Polymer-on-silicon is an attractive, hybrid system that exploits the ease of processing and tailoring of the optical properties of organic materials for developing integrated light sources on silicon platforms for a variety of applications. One attractive feature of this material system is its CMOS-compatibility, which follows from the possibility to synthesize polymers independently of other fabrication processes and then simply add them at the end of the fabrication flow after all of the high-temperature processing is completed [45]. Ferroelectrics are also convenient for

integrated optics because their excellent electro-optic and nonlinear properties and wide transparency can support a broad range of functionalities. However, the difficulty to grow high quality single crystalline thin films of these materials with the existing epitaxial methods, in particular on substrates conventionally used in integrated optics, where lattice-matching constraints imposes an additional limitation, inhibits integration with other material platforms. Nevertheless, a range of integrated waveguide lasers with different temporal output properties have been realized by thermal indiffusion of active rare-earth ions in ferroelectric crystals, in particular $LiNbO_3$ [33]. Figure 8 shows an integrated DFB–DBR coupled cavity laser that has been produced following this fabrication approach for applications related to wavelength division multiplexing (WDM) and interferometric instrumentation [46]. It consists of a Ti:Fe:Er:$LiNbO_3$ section with a photorefractive Bragg grating, representing the DFB laser, and the Ti:Er:$LiNbO_3$ gain section with a broadband multi-layer dielectric mirror of high reflectivity attached on its endface. The laser produced single-frequency emission of up to 8 mW optical power at a wavelength of 1557.2 nm, and the slope efficiency derived was ~22% (Fig. 9).

4. Loss in optical waveguides

From the discussion in the previous section is becomes clear that one of the most critical issues with regard to designing and realizing efficient waveguide lasers is to reduce as much as possible the level of propagation loss in the waveguide. Since the first demonstration of a waveguide laser, many efficient sources have been developed capitalizing on improvements in waveguide fabrication processes and the suppression of loss that the latter brought with them. The main loss mechanisms in waveguides are: (i) scattering, (ii) optical absorption, and (iii) radiation loss, in particular that induced by directional changes in the waveguide.

4.1. Scattering loss

The main source of loss in dielectric waveguides is scattering of the propagating waves at the surface of the waveguide or at its interfaces with the cladding layer and the substrate and can be significant even for surfaces with relatively smooth features. The scattering loss coefficient α for a symmetric waveguide is given by [47]

$$\alpha = \left(\frac{4 \cdot \pi^2 \cdot \sigma^2}{\lambda_o^2} \right) \cdot \left(\frac{1}{d + \left(\frac{2}{p} \right)} \right) \cdot \left(\frac{\cos^3 \theta_i}{\sin \theta_i} \right) \tag{34}$$

In this expression it can be seen that α scales with the square of the ratio of the surface roughness, σ, to the wavelength of the guided mode, λ_o, and is inversely proportional to the waveguide thickness d. In Eq. (34), p represents the extinction coefficient in the substrate and cladding layer; the term $2/p$ is in effect related to the evanescent tails of the mode, indicating that modes with large tails compared to the waveguide thickness are less affected by surface scattering than well-confined ones in high-index contrast waveguides. The last term in Eq. (34) involves the angle of incidence, θ_i, of the launched light beam at the waveguide cladding interface and depends on the waveguide mode that is considered. Higher order modes are associated with higher values of θ_i and hence exhibit higher scattering loss because of the larger number of reflections per unit length that they experience in the direction of propagation. It should be noted that scattering loss may also arise from material imperfections or defects produced within the volume of the structure during the fabrication process. In glass waveguides, volume scattering loss is induced by inhomogeneities due to composition or density fluctuation in the material and the intensity of the scattered light is proportional to $1/\lambda_o^4$. On the other hand, in crystalline waveguides volume scattering loss may originate from poor crystallinity, mixed growth phases or incorrect stoichiometry.

4.2 Optical absorption loss

Modes propagating in a waveguide may experience losses through absorption by contaminant atoms that are either introduced in the waveguide during its fabrication or, are inherently present in the host material. In glass and polymer waveguides a serious source of optical absorption loss associated with the fabrication process adopted is the formation of hydroxyl ions (OH^-). Their fundamental vibrational absorption peak lies at a wavelength of ~2.73 μm, while overtones of this peak introduce absorption loss at wavelengths around 0.72, 0.88, 0.95, 1.24 and 1.38 μm. The formation mechanism and the possible ways for eliminating OH^- ions will be discussed later in this review when details of various waveguide fabrication techniques will be presented. On the other hand, a typical example of intrinsic absorption loss in a waveguide is the non-linear two-photon absorption (TPA) in optically pumped semiconductor waveguides with indirect band gap structure, such as silicon. The effect of TPA is more severe at high optical pump intensities and results in the generation of a significant amount of free carriers, which are responsible for linear photon absorption. The latter compromises the operation of silicon-based waveguide amplifiers, lasers and wavelength converters because the photo-generated free-carriers have a relatively long recombination time. Silicon Raman waveguide lasers [41-43] for example, suffer from free carrier absorption at wavelengths in the range from 1.1 μm, which is the absorption-edge wavelength of silicon, to approximately 2 μm, affecting both the pump and Raman signal. The loss coefficient α_{FC} due to free carrier absorption is given by [48]

$$\alpha_{FC} = \sigma^{FC} \cdot \left(\frac{\lambda}{\lambda_{ref}} \right)^2 \cdot \left(\frac{\beta \cdot I_p^2 \cdot \tau_{eff}}{2 \cdot h \cdot \nu} \right) \tag{35}$$

In the last equation, the product $h \cdot \nu$ is the photon energy, while the last term corresponds to the density of the electron-hole pairs created through pump-induced TPA, with τ_{eff} being the effective recombination time, β the TPA coefficient in silicon, $\sigma^{FC} = 1.45x10^{-17}$ the free carrier absorption

cross section at the wavelength of λ_{ref} = 1.55 μm [49], and I_p the pump intensity. In optically pumped waveguide lasers the effect of free carrier absorption can be mitigated either by pulsed pumping with repetition rates that are longer than the carrier lifetime or, by applying an electric field to remove the carriers and/or by doping with non-radiative recombination centers.

4.3. Radiation loss

Radiation loss occurs when light that is confined and guided in a waveguide is coupled to radiation modes and starts propagating in the substrate or cladding region. In slab or, straight channel waveguides such effects can be triggered by coupling of the guided light from the fundamental or, lower order modes to higher order modes. This coupling results from perturbations along the waveguide, such as structural irregularities and inhomogeneities, diameter fluctuations, build-up of stress or, strain fields in the material, and most importantly from changes in the propagation direction of the mode [50]. Higher order modes are more affected by radiation losses since they are closer to the cut-off condition, where all the energy is transferred to substrate radiation modes. In high-optical-quality straight waveguides the contribution of radiation loss to the total loss is generally negligible when compared to those of scattering and absorption. However, it becomes an issue for devices that are based on curved waveguides, such as for example waveguide lasers with ring resonators. In this case, when the guided mode enters a curved waveguide section the proportion of the evanescent tail at the outer edge of the waveguide cannot travel sufficiently quickly to stay in phase with the remainder of the guided mode and therefore, it separates from the guide and radiates into the surrounding medium. The radiation bending loss coefficient, α, can be derived from the following expression [51]

$$\alpha = K \cdot \exp\left[-\beta \cdot R \cdot \left(\frac{2 \cdot \Delta n_{eff}}{n_{eff}} \right)^{3/2} \right] \tag{36}$$

where K is a constant that depends on waveguide thickness and the refractive indices of its core and cladding, β is a modal propagation constant, R is the radius of curvature of the waveguide, and Δn_{eff} is the difference between the modal effective index n_{eff} and the cladding index. It is clear from Eq. (37) that radiation loss depends exponentially on R, and it can be significant when the refractive index contrast between the waveguide and the surrounding medium is very small.

5. Loss measurement techniques

To measure losses in waveguide structures a number of simple or, more elaborate methods have been proposed and implemented over the years. Aspects that need to be considered when choosing a loss measurement technique amongst the existing methods are the type of waveguide in terms of geometry and material/optical characteristics, the type of predominant loss and the anticipated loss level. The techniques most commonly used for measuring loss in waveguides, are reviewed below.

5.1. Cut-back

The most straightforward way to measure propagation loss is the cut-back method, which relies on successive single-pass transmission measurements through the waveguide at the wavelength of interest, followed by reductions in its length after each measurement. In these measurements light is coupled in and out of the waveguide through its end faces respectively, by means of microscope objectives. The in-coupled power P_o is maintained constant for all the transmission measurements and the power transmission ratio (ratio of transmitted to incident power) for a waveguide length x is [5]

$$\frac{P(x)}{P_o} = 10^{-\alpha \cdot x / 10} \Rightarrow log[P(x)] = log(P_o) - \left(\alpha / 10\right) \cdot x \tag{37}$$

From Eq. (37) it is clear that by plotting the logarithm of the transmitted power as a function of x, a line is obtained the gradient of which provides the propagation loss coefficient α. Whilst, this method can be easily applied to optical fibers because of their long length and the possibility to reduce it without changing the in-coupled optical power, it may prove inaccurate for determining loss in planar waveguides. This is because the waveguide must be removed from the optical setup after each optical power transmission measurement for shortening its length and polishing its end faces, which makes it difficult to reproduce the input coupling during different measurements. In practice, propagation loss with this method is often derived by comparing transmission through waveguides of different lengths, which can be achieved for example by angle polishing the sample, and then fitting the length dependence. Although practical, this approach may compromise measurement accuracy since it is based on the assumption of identical coupling conditions and surface roughness for each waveguide.

5.2. Sliding prism technique

In this technique a pair of prisms is clamped onto the waveguide surface to act as an input and output coupler, respectively [52, 53]. The material of the prisms has a higher refractive index than that of the waveguide and coupling of light into and out of the latter is enabled when the prism-surface separation is sufficiently reduced. Measurements are conducted by keeping the position of the incoupling prism fixed, and moving the outcoupling one to different positions along the waveguide that correspond to different effective lengths. The propagation loss is derived by measuring the outcoupled power in each of these positions and then plotting the logarithm of these values as a function of the distance x between the two prisms using Eq. (37). The slope of the line obtained from this plot yields a value for the propagation loss coefficient α.

Notably, this method can also be applied to multimode waveguides for measuring the loss that is associated with each of the propagating modes separately. Selective coupling of light into each

mode can be achieved by suitably choosing the incidence angle of the laser beam. Loss can then be measured accurately by positioning and masking the detector in a way that it can collect only the transmitted light from the m-line corresponding to the desired mode. In this case, the occurrence of mode conversion is indicated by the presence of multiple m-lines. Limitations to the accuracy of this loss measurement technique are defined by the difficulty to ensure that the outcoupling prism has the same coupling efficiency when it is moved to a new position. Another practical difficulty is to ensure efficient coupling without inflicting any damage on the waveguide surface each time the prism is clamped onto it.

5.3 Fabry-Perot method

This loss measurement method is applied to single-mode waveguides the end faces of which are polished parallel to each other and to an optical quality so as to act as mirrors [54-56]. In this case the waveguide forms a low finesse symmetric resonator and loss is evaluated by coupling it to a laser beam through its end faces with the use of a microscope objective. Changes in the optical path length of the waveguide are subsequently induced by tuning the wavelength of the laser beam or, by heating the waveguide itself. Either of these modulations leads to variations of the internal phase difference $\varphi=2\cdot\beta\cdot l$ with β being the propagation constant of the mode in a waveguide of length l. The fraction of the incident light I_T transmitted through the cavity depends both on φ and the propagation loss α [55, 56]

$$I_T = \frac{(1-R)^2 \exp(-\alpha \cdot l)}{[1-R\cdot\exp(-\alpha\cdot l)]^2 + 4R\cdot\exp(-\alpha\cdot l)\cdot\sin^2(\varphi/2)} \cdot I_O \cdot \eta \tag{38}$$

where I_o is the intensity of the incident laser beam, η is the coupling efficiency to the fundamental waveguide mode and R is the effective reflectivity given by

$$R = \left[\frac{(n_{eff}-1)}{(n_{eff}+1)}\right]^2 \tag{39}$$

with n_{eff} being the effective index. The latter can be directly calculated from the free spectral range of the cavity, defined as $\Delta\nu = c / (2 \cdot n_{eff} \cdot L)$. By measuring the transmission through the waveguide cavity at phase delay values that correspond to periodic maxima (I_{max}) and minima (I_{min}), α can be estimated from the following expression

$$\alpha\left[\frac{dB}{cm}\right] = \frac{4.343}{l} \cdot \ln\left(\frac{R \cdot K}{1-\sqrt{1-K^2}}\right) \tag{40}$$

where $K = (I_{\max} - I_{\min})/(I_{\max} + I_{\min})$ is the modulation ratio. One attractive feature of the Fabry-Perot method is that the loss calculation is independent of the coupling efficiency of the probe laser beam.

5.4. Self-pumped phase conjugation (SPPC) method

This is a non-destructive technique that exploits the self-pumped phase conjugation (SPPC) effect for measurement of propagation loss in channel waveguides [57]. A typical SPPC configuration that has been used for determining loss in Ti:sapphire rib waveguides [58], is shown in Fig. 10. Measurements involve the use of a laser beam with a wavelength that falls outside the absorption band of the waveguide material and can trigger optimal crystal response in terms of intensity and build-up time of the phase conjugated signal. The laser beam is coupled into and transmitted through the waveguide and the outcoupled mode propagates towards a photorefractive crystal ($BaTiO_3$), where it undergoes phase conjugation. Using the standard total internal reflection (TIR) geometry, the crystal response can be optimized by varying the transverse position of the beam input and the angle of incidence. The phase-conjugated beam is retro-reflected and automatically coupled back into the waveguide following exactly the path of the outcoupled beam without experiencing any losses other than the Fresnel reflections at the two waveguide end face-air interfaces. The main advantage of this method is that it ensures optimal efficiency for the coupling of the phase-conjugated light back into the waveguide. Propagation

loss can be therefore precisely determined by measuring and comparing the intensity of the retro-reflected light prior to its coupling into, and after its coupling out of the waveguide, respectively. In the configuration in Fig. 9 the loss α in dB per unit length for a waveguide with a length l, can be derived from the following equation [58]

$$\alpha\left[\frac{dB}{cm}\right]=\left(\frac{1}{l}\right)\cdot 10\cdot\log_{10}\left[\left(\frac{1}{K}\right)\cdot\left(\frac{I_{PD1}}{I_{PD2}}\right)\right] \tag{41}$$

where K is a constant that includes all power losses due to the optical elements and the Fresnel reflections from the coupling and outcoupling faces of the waveguide, and is given by

$$\mathrm{K}=\left(\frac{\mathrm{T_{BS2}}}{\mathrm{R_{BS2}}}\right)\cdot(\mathrm{R_{BS1}})\cdot(\mathrm{T_{O1}})\cdot(\mathrm{T_{O2}})\,(\mathrm{T_{FR}})^2 \tag{42}$$

In the last equation, R_{BS1} and R_{BS2} are the reflection coefficients of the wedged beam splitters WSB1 and WSB2 respectively, T_{BS2} is the transmission coefficient of the beam splitter WSB2, T_{O1} and T_{O2} represent the transmission coefficients for the incoupling and outcoupling objective, respectively, and T_{FR} stands for the Fresnel transmission coefficient at the waveguide-air interface. The SPPC method can provide a systematic error in the measurements of less than 5% [57, 58].

5.5. Streak imaging

With the method of streak imaging, loss is determined by measuring the longitudinal distribution of the light that is scattered from the waveguide at different positions along the guiding direction, z. This can be achieved by using either an optical fiber to collect it [59] or a CCD camera to image and measure its streak [60]. A prerequisite for the implementation of this approach is that the scattering centers in the waveguide should be homogeneously distributed such that it becomes possible to determine accurately the light intensity $I(z)$ in the structure from

the detected scattered intensity $I_{sc}(z)$. The latter is proportional to the light intensity $I(z)$ in the film, which is given by

$$I(z) = I(0) \cdot \exp(-\alpha \cdot z) \tag{43}$$

where $I(0)$ is the intensity of the incoupled light, and α is the attenuation coefficient, which can be derived through fitting with Eq. (43). A practical difficulty that needs to be overcome in order to achieve accurate loss measurements is related to the residual light that propagates in the sample, which although is not directly coupled into the waveguide it can be still detected as scattered light after propagating some distance in the substrate. Another problem arises from the fact that in low loss waveguides the streak intensities produced are weak and therefore difficult to measure. This essentially means that this technique is less precise when applied for loss measurements in high optical quality waveguides.

5.6. Fluorescence imaging

The technique of fluorescence imaging has the same underlying concept with the streak imaging one discussed in the preceding paragraph, allowing for measurement of loss due to scattering and optical absorption in active waveguides. However, in contrast to streak imaging, which relies on detection of scattered light, here, loss is instead determined from the longitudinal distribution of fluorescence light generated by the waveguide along the waveguiding direction by optical pumping with a wavelength that falls within the absorption band of the gain medium [61]. A typical arrangement for such measurements is shown in Fig. 11, where the moveable slit in front of the photodiode is used to determine the intensity of the fluorescence light $I_{flu}(z)$ as a function of the position z of its origin within the waveguide. This allows for the coefficient α of the total loss (scattering and absorption) to be derived in a similar way to the streak imaging technique. However, there also exists the possibility, as recently demonstrated [62], of

distinguishing between scattering α_{sc}, and absorption loss $L_{abs}(\lambda)$, from the detected spatially resolved fluorescence by using different excitation wavelengths. For each of these wavelengths besides α, the relative effective absorption cross sections $\sigma(\lambda)/\sigma_{\max}$ is also obtained by excitation or absorption spectroscopy using the same excitation light employed for loss measurement in order to account for the dependence of $L_{abs}(\lambda)$ on pump linewidth. In this case the expression that provides α as a function of the individual loss components is given by

$$\alpha\left(\frac{\sigma(\lambda)}{\sigma_{\max}}\right) = \alpha_{sc} + L_{abs}(\lambda) = \alpha_{sc} + \kappa \times \frac{\sigma(\lambda)}{\sigma_{\max}} \tag{44}$$

where k represents the absorption loss for $\sigma = \sigma_{\max}$. In deriving the last equation, it was assumed that the dependence of α_{sc} on λ is negligible relative to that of $L_{abs}(\lambda)$, and that the latter is proportional to $\sigma(\lambda)/\sigma_{\max}$. According to Eq. (44), by plotting α as a function of $\sigma(\lambda)/\sigma_{\max}$ the slope of the resulting line and its intersection with the abscissa would yield the values of k, and α_{sc}, respectively. It should be noted that the accuracy of these measurements increases with the number of excitation wavelengths used and the wavelength stability of the pump source.

5.7. Findlay-Clay method

The Findlay-Clay method allows evaluation of an upper limit for the propagation loss in an active waveguide by utilizing the overall performance of the laser source that is based on this waveguide. It is applicable to four-level laser systems that inherently show negligible depopulation of the ground state, and for which the absorbed power threshold, P_{th} is dependent on the level of the output coupling as follows [63]:

$$P_{th} = K \cdot [(2 \cdot \alpha_L \cdot l) - \ln(R_1 R_2)] \tag{45}$$

where α_L is the propagation loss coefficient in the laser cavity, l is the waveguide length, R_1 and R_2 are the intensity reflectivities of the in- and out-coupling mirrors, respectively, and K is a

constant, which for a longitudinally pumped system is given by

$$K = \frac{\pi \cdot h \cdot \nu_p}{4 \cdot \tau \cdot \sigma_e} \cdot \sqrt{w_{lx}^2 + w_{px}^2} \cdot \sqrt{w_{ly}^2 + w_{py}^2} \tag{46}$$

where, h is the Planck's constant, ν_p is the frequency of the pump irradiation, w refer to the $1/e^2$ radii of intensity of the pump *(p)* and laser (*l*) modes, in the horizontal *(x)* and vertical *(y)* planes, respectively, τ is the fluorescence lifetime, and σ_e is the emission cross section. The loss in the waveguide is derived by measuring the absorbed pump power threshold for lasing using output coupling mirrors with different values of reflectivity. By inserting the absorbed power threshold obtained for each of the outcoupling mirrors used in Eq. (45) and then plotting $P_{th}/2 \cdot l$ as a function of $-\ln(R_1 \cdot R_2)/2 \cdot l$, a straight line is obtained the intercept of which with the abscissa yields the value of the loss coefficient α_L. An upper value for propagation loss *L*, (in reality *L* also accounts for losses due to imperfections in the attachment of the cavity mirrors), in units of $dB \cdot cm^{-1}$ can then be derived loss from the expression

$$L[\,dB\,] = 10 \cdot log_{10}\left[\frac{I_{out}}{I_{in}}\right] \Rightarrow L\left[\frac{dB}{cm}\right] = 10 \cdot log_{10}\left[exp(-a_L)\right] \tag{47}$$

where I_{in} and $I_{out} = I_{in} \cdot exp(-\alpha \cdot l)$ are the intensities at the input and output endface of the waveguide, respectively.

6. Fabrication techniques

A key factor in fully exploiting the enormous potential of the waveguide laser sources is their fabrication, which includes the technologies required for the waveguide formation and the the development of the materials used as gain media. There is a wealth of fabrication techniques that have been employed for realization of waveguide lasers, which can be grouped in two broad

categories: those involving growth of a film onto a substrate of lower refractive index to produce a step index change, and those relying on definition of a waveguiding region inside an existing material, either by inducing a localized refractive index modification or, by surface microstructuring. Several criteria exist for the selection of the suitable technique in each specific case. These include simplicity and cost-effectiveness of the fabrication process, its applicability to a specific laser medium, optical quality of the structures produced, attainability of the desired waveguide geometry, flexibility in waveguide design, device footprint and scalability of fabrication area. In cases when integration of the waveguide laser with an optical circuit or functionality is the intended goal, a factor that also needs to be considered is whether the process leaves unaffected any components or devices on the chip that have been produced in earlier steps of the fabrication flow. A summary of the most commonly applied fabrication methods for developing waveguide laser sources is given below. Since many of their aspects have been well documented in reviews of specific technical areas, the remaining of this article is not intended to be a comprehensive review of each individual technique. It will instead illustrate the basic principles behind their operation and highlight their advantages and shortcomings with regard to their application for development of waveguide lasers.

6.1. Techniques involving waveguide deposition on an existing substrate

6.1.1 Epitaxial growth

Liquid phase epitaxy (LPE) and the vapor phase deposition techniques of pulsed laser deposition (PLD) and molecular beam epitaxy (MBE) that will be discussed in the following paragraphs have emerged as the key technologies for epitaxial growth of planar crystalline waveguides. An attractive feature that all of these methods have in common is the capability of producing single crystalline films, which are very favorable for waveguide applications as they inherently exhibit lower scattering loss than their polycrystalline counterparts. Furthermore, these

deposition approaches can ensure substitutional inclusion of rare-earth dopant ions in the layers grown, thereby minimizing broadening of the absorption and emission spectral lines, which is associated with increased laser thresholds and reduced gain.

6.1.1.1. Liquid Phase Epitaxy (LPE)

By contrast to MBE and PLD, LPE is a non-vacuum process that can be carried out using simple and low-cost apparatus [64]. As shown in the schematic in Fig. 12, growth of dielectric waveguide layers involves vertical dipping and rotation of an oriented, single-crystal substrate into a crucible that contains a supersaturated molten solution of oxide precursors of the layer constituents (i.e. the host material and for optically active layers the rare-earth dopant ions). The LPE deposition process takes place within a furnace, where a wide zone of uniform temperature is established and maintained, to ensure near-zero temperature gradients in the solution. Prior to the growth phase of the process, the solution is heated above its saturation temperature and is maintained at this level for sufficient time to allow homogenization of the liquid. The solution temperature is subsequently gradually reduced, and in the course of this process, the crystal substrate is slowly introduced in the furnace and kept in close proximity with the solution until thermal equilibrium with the latter is established. It is then immersed in the solution when the temperature of the latter is still slightly higher than the saturation value in order to dissolve an outer thin layer of the crystal and hence prevent potential introduction of defects in the film to be grown. By further cooling, the solution is finally brought to the supersaturation regime, at which spontaneous crystallization occurs in the presence of a seed of a critical size (in this case the substrate) [64]. The supersaturation temperature depends on the composition of the melt and tends to increase slightly with increasing rare-earth doping level. Once growth has been completed, the substrate is removed from the solution and maintained at close proximity with it, while the whole system is slowly cooled to room temperature. The whole process results in the

growth of the desired crystal layer on the front and backside of the substrate at a speed that is typically about 2 $\mu m \cdot min^{-1}$. The critical process parameters for the quality of the films produced include the melt composition and temperature, the substrate temperature and orientation, the growth time, and the cooling rate of the substrate after film growth.

LPE allows a reasonable freedom of choice over fundamental waveguide design parameters such as core thickness and NA. The constraints imposed on the choice of materials for the substrate and the film are related to their lattice constants and thermal expansion coefficients, which should exhibit minimal mismatch in order to minimize loss contribution from the build-up of stress at the film-substrate interface and prevent formation of cracks due to differential thermal expansion during the film deposition process. In contrast to vapor phase epitaxial techniques, LPE is a near thermodynamic equilibrium process, since the supersaturations imposed for the growth are very low. This enables fabrication of single crystalline layers of exceptional optical quality, with thicknesses that can exceed 100 μm. Furthermore, LPE-grown layers exhibit extremely low propagation loss, reaching in some cases that of the corresponding bulk crystals (< 0.05 $dB \cdot cm^{-1}$) [66], which is the lowest value reported to date for a crystalline planar waveguide device. One of the advantageous features of LPE is the feasibility of lattice-matched growth [67], which can be achieved by introducing passive ions with suitably chosen relative concentrations in the film composition. This is an efficient way of reducing scattering loss and ensuring enhanced index contrast between film and substrate, which, as discussed previously, is advantageous for integrated waveguide devices. Figure 13(a) shows electron probe microanalysis (EPMA) results obtained for an epitaxially, lattice-matched grown $KY_{0.59}Gd_{0.19}Lu_{0.22}(WO_4)_2$ layer on a $KY(WO_4)_2$ substrate, revealing that the atomic percentage of the Y, Gd and Lu ions across the layer remains constant, which in turn indicates that LPE can ensure homogenous composition across the film thickness. In Figs. 13(b) and (c) an environmental scanning electron microscopy

(ESEM) picture of the $KY_{0.59}Gd_{0.19}Lu_{0.22}(WO_4)_2/KY(WO_4)_2$ interface and a photograph of the whole structure are presented, respectively.

Fabrication of multi-layered structures by LPE is in principle feasible however, it is a time-consuming process, requiring use of several different melt compositions and optimization of deposition for each of them. The main limitations of this method are the lack of accurate thickness control and the poor surface uniformity of the layer, which however, can be overcome by polishing. LPE has been extensively used for growth of oxide layers and for waveguide lasers in particular, early work focused on development of rare-earth doped garnet films [66, 68-75]. Research interest in recent years has shifted towards deposition of rare-earth doped double tungstate structures [65, 76-85], due to a number of favorable properties of these crystals, such as the possibility of doping with high concentrations of rare earth ions and the large emission and absorption cross sections of the latter in this family of crystals. Finally, there is only one report to date on a waveguide laser based on other crystals, namely on YLF:Nd^{3+} [86].

6.1.1.2. Pulsed laser deposition (PLD)

PLD is a fast and versatile technique for fabricating a wide range of thin-film devices including waveguide lasers [87-89]. As shown in Fig. 14 the growth process is carried out in a vacuum chamber, where a pulsed laser beam is focused onto a solid target, thereby inducing material ablation. The material ejected from the target forms a forward–directed plume and is deposited onto a substrate located opposite to the target at a distance of a few centimeters. Depositions are often performed in a background gas environment, which is either a buffer gas, if reduction of the kinetic energies of the ablated species is desirable or, an oxygen agent (typically molecular oxygen), if oxygenization of the ejected species is required. Although in most cases excimer lasers with nanosecond pulse duration have been employed to induce material ablation, use of picosecond and femtosecond lasers has also been reported, primarily for studying the

effect of pulse length on the formation of particulates in the film, which represent a significant source of optical loss. The results obtained in these works suggested that the success of this approach in eliminating these particulates depends on the target material [90-92].

Attractive features of the PLD technique include its capability in yielding stoichiometric material transfer from the target to the substrate, the high growth rates that can be achieved, which even for hard crystalline materials such as sapphire can be up to 25 $\mu m \cdot h^{-1}$ [87], as well as the possibility to control the location and valence state of dopant inclusions and the layer thickness. PLD provides the same degree of flexibility with LPE in the choice of the combination of layer and substrate material, requiring minimum mismatches between their respective thermal expansion coefficients and lattice constants. Sophisticated PLD-configurations involving multiple-target carousels and multiple laser sources [Fig. 15(a)] enable fabrication of capped or clad waveguides, mixed materials, or multilayer structures with step or graded interfaces [93]. Figure 15(b) shows a scanning electron microscopy (SEM) micrograph of a 5-layer garnet crystal structure deposited on a YAG substrate using such elaborated configurations. Since PLD operates at far from equilibrium conditions, growth is relatively easy for simple oxides with cubic structure, such as garnets and sesquioxides or, hexagonal structures like α-Al_2O_3:Ti^{3+} (Ti:sapphire). However, it becomes considerably difficult for materials with more complex lattice structures, such as the biaxial crystals $YAlO_3$:Nd^{3+} [92, 94, 95] and $KGd(WO_4)_2$:Nd^{3+} [96], in which unwanted crystalline phases were obtained in the films produced. For this reason reports on waveguide lasers fabricated by PLD are limited to a small group of crystals that includes GGG:Nd^{3+} [97-102], (Gd, Lu)$_2O_3$:Nd^{3+} [103], (Gd, Lu)$_2O_3$:Yb^{3+} [104], and Ti:sapphire [13, 14, 105]. Recently, lasing has also been obtained from polycrystalline semiconducting films based on chromium doped zinc selenide (ZnSe:Cr^{2+}) grown on sapphire substrates [106]. Although PLD is particularly suitable for deposition of glass films from the viewpoint of the very large and controllable photosensitivity [107-110] that these structures exhibit, there is no report to date on

laser operation of active glass waveguides produced by this technique, largely due to the relatively high propagation losses. Use of alternating targets allowed for engineering of the rare-earth dopant ion profiles and their distribution either in-depth, or both the in-depth and in-plane in PLD-grown amorphous $Al_2O_3:Er^{3+}$ [111, 112], and $Al_2O_3:Er^{3+}:Yb^{3+}$ [113] waveguide layers. This approach has the advantage of reducing ion-ion interactions that are detrimental for laser operation.

As mentioned earlier in this subsection, propagation loss in PLD-grown layers often originates from micron-size particulates that are present on their surfaces or embedded in their bulk. Their formation is arguably the main drawback of PLD and can limit the prospects for development of functional waveguide devices. Besides the use of picosecond and femtosecond pulsed lasers for target ablation, other approaches to limiting this effect that have been reported in the literature, include colliding plumes and synchronized pulsed gas-jet configurations, spinning targets, mechanical shutters, and velocity selectors with mixed success [87, 114, 115]. Another route that has proven successful in suppressing loss is to bury the PLD-grown waveguide by growing on top of it a capping layer [87].

To date, the lowest propagation loss measured in a PLD-fabricated waveguide laser has been reported for a $GGG:Nd^{3+}$ structure with slab geometry [102]; the loss value obtained was less than 0.1 $dB \cdot cm^{-1}$, which is only twice as high as that of the bulk crystal material (~0.04 $dB \cdot cm^{-1}$). An interesting feature of the PLD technology is its potential to produce films of materials with a very high melting point at significantly lower temperatures. A testament of this ability is the growth of rare-earth-doped sesquisoxide waveguide layers at a temperature around 650°C [103, 104], well below their melting temperature of over 2400°C. The high melting temperature of these crystals in combination with their phase transition point that lies below their melting point, make their growth in bulk form very challenging [116]. In this respect, another notable example is the deposition of Ti:sapphire layers with a degree of crystal perfection comparable with the

commercial bulk crystals used as targets, at temperatures around 975ºC, which is well below the melting temperature of the bulk crystal (~2200ºC) [117]. Finally, it is worth noting that PLD has also proven suitable for two-dimensional, lattice matched, layer-by-layer growth of rare-earth-activated planar waveguides [103, 104, 118]. This mode of growth is an effective approach to engineering enhanced index contrast between film and substrate, which is important for integrated optics devices.

6.1.1.3. Molecular beam epitaxy (MBE)

Molecular beam epitaxy (MBE) is a sophisticated, ultra-high-vacuum (UHV) technique that is conventionally employed for epitaxial growth of compound semiconductor layers. However, considerable effort has also been directed towards development of rare-earth doped dielectric, single-crystal waveguide layers, in particular fluorides [119]. In a typical MBE configuration, the precursor materials of the crystalline host and the rare-earth dopant ions are contained in shuttered, Knudsen-type effusion cells, which are isothermal cavities that can be resistively heated to a suitable temperature. Due to the elevated temperature, the precursor materials evaporate through an existing hole in each cell to produce direct beams of thermally accelerated atoms/molecules that are combined on a heated substrate to form a film. It should be noted that for materials with high melting temperature, evaporation is induced with electron beam guns. The growth rate, composition and doping level of the films produced are determined by the beam fluxes, which are in turn controlled by the temperature of the effusion cells. The growth rate also depends on the distance of the effusion cells from the substrate. The entire deposition assembly is enclosed in a UHV chamber, which is in turn part of a system that also includes two other separate units, a load-lock and an analysis chamber. MBE offers a number of attractive features when compared to other epitaxial growth methods, of which the most important are the possibility to produce ultra-high purity layers and the ability to maintain precise control over their

composition and thickness at the single atomic level. Such an accurate control allows refractive index and lattice engineering of the film and is enabled by the inherently low growth rates of the MBE technique and the possibility to promptly start and interrupt the deposition process by turning on and off the molecular beams.

Although there are reports in the literature on MBE growth of waveguide films of complex ternary oxide materials such as $LiNbO_3$ [120] and $BaTiO_3$ [121], most of the work on dielectric waveguide layers to date has focused on hetero-epitaxial deposition of rare-earth doped fluoride waveguides, such as ZnF_2, PbF_2, [122] CaF_2, [123] and LaF_3 [124-127]. They were grown on different dielectric and semiconductor substrates and their propagation loss was on the order of 1 $dB \cdot cm^{-1}$ [122, 126, 127]. Reports on waveguide lasers are limited to $LaF_3:Nd^{3+}$ structures with slab and channel geometries [126, 127]. The reasons behind this interest in implementing this method for growth of fluoride crystal layers rather than for their oxide counterparts are: (i) the fluoride molecules have a higher dissociation energy, and therefore can withstand the processes of evaporation and transport to the substrate without decomposing, and (ii) the combination of the low temperatures required for growth of fluoride layers and the inherently low growth rates of the MBE method ensures homogeneous distribution of the rare earth ions within the layers and thus minimization of clustering. This latter feature allows doping with significantly higher rare-earth ion concentrations compared to the corresponding fluoride bulk crystals without luminescence quenching. Notably MBE is ideally suited for fabrication of rare-earth doped divalent fluoride waveguide layers. The growth of the latter can be accomplished with the use of rare-earth trifluoride precursors, which conveniently provide a quasi-intrinsic charge compensation mechanism in the layer thanks to the excessive number of F-interstitials that is available when a trivalent rare-earth ion replaces a divalent cation. A barrier to the widespread adoption of MBE for waveguide fabrication is the equipment cost and the limited flexibility in terms of using the same equipment for depositing a range of different materials. Equipment is usually dedicated to

growth of a single material in order to preserve the ultra-high vacuum, ultra-clean growth conditions and the ability to control accurately the whole process. Finally, it should be noted that MBE is not ideal for fabrication of thick films due to the low deposition rates that can be achieved, which for rare-earth doped fluoride crystalline layers do not exceed ~ 0.7 $\mu m \cdot h^{-1}$ [126].

6.1.2. Chemical Vapor Deposition (CVD)

Chemical vapor deposition (CVD) is capable of producing crystallographically oriented and amorphous layers and has been used for development of active waveguide devices based on glasses [128-130], oxides [131], and semiconductor alloys [132]. The CVD process involves growth of a solid film on a substrate either through chemical reactions in the gas phase or, by decomposition of a gaseous precursor of the material intended for deposition. The applicability of this method depends on the availability of volatile precursors, which should also be stable enough to withstand delivery through suitable feed lines to the vacuum chamber where the deposition process takes place. In standard (thermal) CVD the substrate is maintained at an elevated temperature, typically between 400 and 1500°C, and the chemical reaction that leads to film growth is thermally activated. The substrate temperature in this case is a critical parameter for the deposition since it determines the pathway of the underlying chemical reaction. The latter occurs either within the gas medium that surrounds the heated substrate (homogeneous reaction), or, on the surface of substrate (heterogeneous reaction), where the reactants are adsorbed and undergo migration and film-forming reactions.

Several variants of the standard CVD technique exist, involving different gaseous precursors, gas pressure regimes or, means to induce the chemical reaction that leads to film deposition. Amongst these methods, plasma-enhanced CVD (PECVD) is the most commonly used for fabrication of optical waveguides. The PECVD apparatus consists of a vacuum chamber with a two parallel electrode plates, of which the lower electrode usually serves as a substrate holder and

can be heated to 350ºC, whereas the upper electrode is driven by an RF power supply. A discharge that is ignited and maintained by the RF field in the mixture of the precursor gases between the electrodes and away from the substrate results in the formation of a low-pressure plasma (2-5 Torr). The average electron energies in this plasma typically range from 1 to 20 eV, a level that is sufficient for the ionization and dissociation of the gas molecules. Gas-phase or surface chemical reactions between the highly energetic molecular and atomic fragments produced by this process lead to the deposition of a solid layer on the substrate. By contrast, to standard CVD, both deposition rate and film properties in PECVD depend on plasma parameters. Fabrication of pure silica layers, which is an interesting host for optical devices, usually involves a chemical reaction between silane (SiH_4) and nitrous oxide (N_2O)

$$SiH_4(g) + 2N_2O(g) \leftrightarrow SiO_2(s) + 2H_2(g) + 2N_2(g) \tag{48}$$

Various glass network-forming oxides such as P_2O_5, GeO_2, and B_2O_3 can be introduced in the silica glass network to modify its properties (i.e. refractive index, photosensitivity, viscosity, and capability of dissolving rare-earth ions) by co-deposition using their respective precursors, phosphine (PH_3), germane (GeH_4), and diborane (B_2H_6) that can be for this purpose transported to the reaction site. Similarly, doping with rare-earth ions is performed by vapor delivery of organic complex rare-earth precursors, such as chelates. The schematic of a typical PECVD set-up that has been used for the growth of Al_2O_3 films [133] is shown in Fig. 16. Films in this case were produced by a chemical reaction between the trimethyl-amine alane $(CH_3)_3NAlH_3$, (TMAA) precursor and N_2O and deposited on substrate heated at 300 ºC.

Despite the complexity of the apparatus and the large number of control variables, PECVD has a number of attractive features, of which the most important is arguably that film growth can be accomplished at relatively low substrate temperatures. This is exemplified by the fact that whilst temperatures between 650 and 850ºC are needed for growing high-quality SiO_2 films with standard CVD, layers with similar quality can be produced by PECVD at temperatures from 300

to 350ºC. This temperature difference exists because a part of the energy needed for the activation of chemical reactions that lead to material deposition is provided by the plasma. The low deposition temperatures offer flexibility in the choice of the substrates that can be used for the growth, allowing film deposition even on temperature-sensitive materials. Furthermore, they are greatly beneficial for growth of rare-earth doped glass waveguides as they significantly reduce the possibility of ion clustering that tends to appear at high temperatures due to the increased diffusivity of the rare-earth ions. Finally, PECVD is also associated with low deposition rates, which allow for accurate control over film stoichiometry and doping level thus ensuring deposition of high quality layers.

Difficulties in the implementation of this technique arise from the harmful nature of the precursor gases that are often required for waveguide fabrication, which imposes limitations on the range of materials that can be grown. Similar problems are encountered with the gaseous by-products of the process, which may be toxic, flammable or corrosive and require appropriate handling. These gases however, are in a way useful because their analysis provides a mean to understand the chemical reaction mechanisms involved in the CVD process and in turn to optimize the quality of the films produced. Another intrinsic problem of this technique is the presence of hydroxyl groups (OH^-) in the deposit, originating directly from the reactants. They are responsible for luminescence quenching of the rare-earth ions through coupling of their excited states to high energy vibrational modes of the O-H bonds and their removal requires post-fabrication annealing at high temperatures.

PECVD allowed fabrication of planar silica slab waveguides with a propagation loss as low as 0.01 $dB \cdot cm^{-1}$ [134], and was often used in combination with photolithographic and ion-beam etching techniques for development of active channel waveguide devices. The latter include $Al_2O_3:Er^{3+}$ amplifiers, exhibiting a broad emission bandwidth of about 55 nm [131] and integrated silica/silicate-on-silicon laser sources, in particular Er/Al- and Yb/Al-doped

germanosilicate glass waveguide lasers [128-130]. Figure 17(a) shows a schematic of a DBR laser array based on Er/Al-doped germanosilicate glass fabricated by a combination of PECVD and reactive ion etching (RIE). The cavity was defined by Bragg gratings imprinted in one-step using a single phase mask. Since the waveguides have different widths and hence different effective refractive indices, it follows that the optical path length between the grating periods for each waveguide will also be different, leading to laser emission at multiple wavelengths [Fig. 17(b)].

6.1.3. Flame hydrolysis deposition (FHD)

Flame hydrolysis deposition (FHD) is one of the most important techniques for fabrication of rare-earth doped glass optical waveguides, and has been extensively applied to produce waveguide components for silica-on-silicon planar photonic circuits [135, 136]. In the FHD process, a layer of the eventual glass is deposited in the form of a low-density soot on a planar substrate, which is typically a silicon wafer covered with a thermal oxide layer of approximately 10-μm thickness. The latter is used to improve the adhesion of the deposited layer and to isolate the waveguide from the high index silicon substrate. Deposition involves oxidation and hydrolysis of metal halide precursors (in most cases chlorides), which both take place in an oxy-hydrogen flame. The precursors are transported to the flame by a carrier gas, usually oxygen or, nitrogen (Fig. 18). In this process, oxidation is the dominant reaction at relatively high temperatures, above 1200 °C, that are reached along the central axis of the flame, where the temperature can be as high as 2000 °C. Hydrolysis on the other hand prevails at temperatures below 1200 °C and can even take place at room temperature. The most commonly used precursor for synthesis of silica soots is silicon tetrachloride ($SiCl_4$) and its oxidation and hydrolysis can be described by the following chemical equations, respectively

$$SiCl_4(g) + O_2(g) \leftrightarrow SiO_2(s) + 2Cl_2(g) \tag{49}$$

$$SiCl_4(g) + 2H_2O(g) \leftrightarrow SiO_2(s) + 4HCl(g) \quad (50)$$

The soot has a porous structure and consists of particles with a typical diameter of 0.1 μm, which then form aggregates with a diameter of approximately 0.2 μm via collision and coalescence [137]. Following its deposition, the soot is consolidated into a full density amorphous solid film, by viscous sintering in a suitable furnace, at a temperature close to its melting point, which depending on its composition can range from 1000 to 1500 °C. Soots of phosphate, germanate, and borate glasses that are commonly used for waveguide amplifiers and lasers are usually produced by using phosphorous oxychloride ($POCl_3$), silicon tetrachloride ($GeCl_4$), and boron trichloride (BCl_3) as precursors, respectively, in a similar way to that described by Eqs. (49) and (50). Other exciting possibilities offered by the FHD method include fabrication of multicomponent and rare-earth ion doped glasses by co-deposition and development of layered structures of different glass compositions by sequential deposition using different gaseous halide precursors. The latter are contained in columns that can be heated to produce vapors that are subsequently transported to the deposition zone through separate delivery lines. In such configurations, the glass composition can be precisely controlled by varying the relative amounts of the precursor elements. Organic compounds, such as chelates are often preferred for use as rare-earth-ion precursors due to their high vapor pressure, which allows delivery in lines that are maintained at considerably lower temperatures (~200ºC) than those required for transport of the less volatile halide precursors (several hundred degrees) [138]. A typical FHD configuration for growth of rare-earth multicomponet glass films is shown in Fig. 19(a).

Besides the standard vapor-transport based technique for doping, additional approaches such as aerosol [139, 140], and solution doping [141] can be used to incorporate rare earth ions into the soot. Figure 19(b) shows a typical implementation of the former method, which relies on feeding aerosol droplets of an aqueous solution of the dopants together with the halide precursors to the oxy-hydrogen flame, where after oxidation and hydrolysis a doped soot layer is produced

and deposited on a substrate in a single-step process. On the other hand, solution doping is accomplished after the soot has been formed and partially sintered into a robust sponge-like layer. In this process, the soot is immersed into a solution of the chosen rare-earth precursor (typically a chloride precursor in an alcohol solution) for a certain period of time and then removed, dried and consolidated into a uniform fully solid layer. The doping level of the latter is determined by the concentration of the rare-earth precursor in the solution, the duration of the immersion and the degree of pre-sintering of the soot layer. FHD is capable of producing waveguide films with low propagation loss (0.01 $dB \cdot cm^{-1}$ [135]) and very good uniformity, exhibiting a thickness variation and a surface roughness that can be as low as 0.1 μm and 0.1 nm, respectively. A disadvantage of this technique is the difficulty to control precisely the dopant concentration and ensure its uniform distribution in the layer. Laser operation has been reported for FHD-deposited Nd-doped [138, 142-145] and Er-doped [146, 147] silica waveguides as well as for Er-doped phospho-silicate waveguides [148].

6.1.4. Sol-gel deposition

Sol-gel deposition is a low-cost, simple and versatile technique for fabrication of planar waveguides based on various glasses and organic-inorganic hybrid materials [149-151]. The versatility of this approach in terms of potential to process a broad range of materials and produce different type of structures is illustrated in Fig. 20. In the conventional sol-gel process, one or a mixture of metal alkoxide precursors with the generic formula $M(OR)_n$, where $R = C_nH_{2n+1}$ is the alkyl group, are hydrolyzed to form hydroxyl groups. The latter are subsequently subjected to (poly) condensation to produce a colloidal suspension (sol) using an acid or, a base, such as hydrochloric acid (HCl) or, ammonia (NH_3), respectively, as a catalyst for the process. The hydrolysis and (poly) condensation reactions are schematically expressed by the following equations, respectively,

$$M(OR)_n + n \cdot H_2O \leftrightarrow M(OH)_n + n \cdot ROH \quad (51)$$

$$m \cdot M(OH)_n \leftrightarrow m \cdot MO_{n/2} + (m \cdot n/2) \cdot H_2O \quad (52)$$

The sol produced by this process is deposited on a substrate either by dipping or, spin coating or, spraying, where then coagulation of the colloids leads to the formation of a porous network of solid material (gel) that is permeated by the liquid solvent (acid or base). The gel is ultimately densified to form a glass film by sintering at temperatures slightly above the glass transition temperature of the eventual glass. Arguably the most investigated metal alkoxide precursor for formation of silica/silicate glass waveguides is tetraethylorthosilicate, with the chemical formula $Si(OC_2H_5)_4$ (also known as $Si(OEt)_4$ or TEOS).

One important feature of the sol-gel process is the possibility to tailor the molecular structure of the layer to an intended application by suitably choosing the precursor materials and processing chemistry conditions. This has allowed fabrication of multicomponent silicate glass films that contain a large amount of refractory materials, such as Al_2O_3 [152], TiO_2 [153], ZrO_2, [154], and GeO_2 [155] from suitable mixtures of alkoxide precursors. Furthermore, doping with rare earth ions [150, 156], dyes [157], or, unstable non-oxide semiconductors [158] is also feasible and can be accomplished either in the hydrolysis step, when the layer is still in the sol form or, after the formation of the gel. A drawback of the conventional sol-gel method is the appearance of cracks in the films produced due to the large amount of shrinkage experienced by their wet gel during drying. This effect places a limitation on the maximum waveguide thickness that can be achieved in practice, to values that do not exceed 200 nm, which is insufficient for on-chip integration with other waveguide components. This problem can be overcome by multiple successive depositions and thermal annealing treatments at a suitable temperature after the formation of each individual layer. Fabrication of multi-component glasses from mixtures of alkoxide precursors may also pose a practical challenge, since the shrinkage in their volume often results in preferential precipitation of a particular oxide during sol formation. Nevertheless, sol-

gel-fabricated waveguides with propagation loss as low as 0.7 $dB \cdot cm^{-1}$ were reported [153] and a number of waveguides laser sources were demonstrated, including dye-doped silica [159, 160], zirconia [161-167], titania–silica [168], and Nd-doped silica-hafnia [169] layers.

An intriguing possibility offered by the sol-gel method is the growth of hybrid organic–inorganic optical materials, a route that has been exploited for fabrication of organic-silica/silicate optical waveguide devices. This approach relies on the use of organically modified silica/silicate (ORMOSIL) precursors, which are modified silicon alkoxides, having one or, more of their alkoxy groups replaced by a nonhydrolyzable group (usually trialkoxysilanes and tetralkoxysilanes). In this case, the remaining three alkoxy groups form the silica network while the organic component acts as a network modifier [170, 171]. The ORMOSIL's organic ligand may carry either a simple nonhydrolyzable organic group, such as an alkyl or an organic dye, which are bonded to the inorganic network as network modifiers or, alternatively, reactive groups that can polymerize or copolymerize (methacryloyl, styryl, or epoxy groups that facilitate densification at low temperatures) or, undergo hydrolysis-condensation (trialkoxysilyl groups) and act together with the inorganic components as network formers. In this latter case, the sols that are used contain besides the ORMOSIL precursor a metal alkoxide precursor and the solvent(s). The role of the metal alkoxide precursor is twofold: to serve as a catalyst for the organic polymerization and to contribute to the formation of the inorganic oxide. In the hybrid layers produced, the organic and inorganic constituents are connected with each other by strong covalent or, ionic bonds. Their thermo-mechanical properties are superior to those of polymers and their homogeneity is considerably enhanced with respect to inorganic sol-gel materials, without however reaching that of polymers.

An advantage of the hybrid sol-gel approach is that the temperature required for the polymerization and consolidation of the layer to its final density is low compared to the conventional sol-gel process. The process temperature can be further reduced by introducing a

photosensitizer in the sol, to allow for photopolymerization by exposure to UV light [172]. Furthermore, the hybrid inorganic-organic sol-gel route provides an effective means of engineering optical properties of the films, such as refractive index and transparency, and most importantly, it represents an effective solution to the problem of film cracking, allowing for single-step fabrication of up to 10-μm-thick, crack-free structures. Such thicknesses are feasible because the inclusion of a significant fraction of nonhydrolyzable organic groups in the gel network increases the flexibility of the layers, making them less prone to cracking during the sintering process. Reports on laser emission from hybrid waveguides are of dye-doped titania-ORMOSIL [159], zirconia-ORMOSIL [161, 173] and zirconia–titania-ORMOSIL [174] layers.

The sol-gel chemistry is also used in combination with self-assembled surfactants that serve as templates, to produce nanostructured hybrid materials [175, 176]. This approach ensures enhanced control over the local structures in the mesoscopic scale (2-100 nm) and has been successfully implemented for synthesis of mesostructured hybrid waveguide gain media. The templates used were amphiphilic triblock copolymers, which have the generic formula ABA with A and B being a hydrophilic and a hydrophobic block, respectively [176, 177]. Variation of their chemical structure allows for structuring of inorganic networks with controlled segregation at the nanoscopic level and tuning of hybrid interfaces and hence of the material properties. Using poly(ethylene oxide)-b-(polypropylene oxide)-b-poly(ethylene oxide) (EO_x-PO_y-EO_x) triblock copolymer surfactants, in particular $(EO)_{20}(PO)_{70}(EO)_{20}$ (P123) and $(EO)_{106}(PO)_{20}(EO)_{106}$ (F127), waveguide ASE sources [178] and lasers [179, 180] based on Rhodamine 6G-doped mesostructured silica composites were produced from a mesostructured precursor solution containing the hydrolyzed metal alkoxide precursor of the silica network TEOS, the self-assembled block co-polymer template diluted in an organic solvent and the dye.

6.1.5. Thermal sublimation

Deposition of layers by thermal sublimation is considerably less demanding compared to epitaxial growth methods and has proven to be an effective approach to fabricating planar slab waveguides based on dye-doped small-molecular-weight organic semiconductors for laser sources. The deposition process is carried out in a vacuum chamber and involves heating of a solid source material by a resistance or, an electron beam. The chamber is maintained at a sufficiently low pressure, such that the sublimated material can freely propagate towards a substrate positioned opposite to the source material, where it condenses to form a film. The sublimation process is carried out at temperatures and pressures below the triple point in the phase diagram of the source material to ensure that the latter undergoes an endothermic phase transition directly to the gas phase without intermediate liquification. To enhance the adhesion of the layer, the substrate is often maintained at a moderate temperature (~200 ºC) during deposition by using a second heating element. Thermal sublimation is capable of producing layers of superior chemical purity and optical quality compared to those produced by solution processing [181, 182]. Furthermore, it offers good control over film uniformity and is particularly suitable for small-molecule organic materials that can be damaged by exposure to solvents. A shortcoming of this method is that it cannot ensure precise control over the composition of the dye-doped organic films produced, due to the difficulty in modulating the transport rates of the sublimated precursor materials. This difficulty arises from the fact that these rates can only be controlled through the temperature of the organic precurors and change rapidly within a few degrees.

Lasing has been reported for slab waveguides based on the small semiconductor molecules tris-(8-hydroxyquinoline) aluminum (Alq_3) and 2-napthyl-4,5-bis(4-methoxyphenyl)-1,3-oxazole (NAPOXA); the former was doped with different dyes such as DCM [182, 183], DCM2, rhodamine 6G, or pyrromethene 546 [183], and the latter with DCM2 [184, 185]. Deposition of these structures was performed in vacuum chambers by simultaneous sublimation of the host and

dopant molecules at background pressures of about $2x10^{-6}$ mbar. Deposition rates and film thickness of up to 50 Å·min^{-1} and 350 nm, respectively, were achieved. Figure 21 shows laser spectra obtained for two different pump powers from a DBR waveguide laser based on a Alq_3:DMC2 film formed by thermal sublimation together with a schematic of the structure itself.

6.1.6. Sputtering

Sputtering is a vacuum process that has been used for deposition of amorphous dielectric waveguide layers based on rare-earth doped oxides. There are several variations of this technique, involving use of different potentials, gas pressure regimes and physical arrangements, which all fall under two broad categories, namely *diode-* and *magnetron* sputtering. Diode sputtering systems employ a parallel plate reactor with the cathode and the anode containing the target material and the substrate, respectively. In this process, a discharge of an inert gas such as argon, neon or krypton, that is ignited between the electrodes and maintained by either a DC or a RF power source produces high-energy (from 2 to 30 eV), positively charged ions. The latter are accelerated towards the electrode with the target, which is kept at a high negative potential, and bombard the target material, thereby transferring their kinetic energy into it. As a result, material is ejected from the target, mainly as neutral atoms, and deposited on a substrate positioned on the opposite electrode to form a layer. For the deposition of insulating materials, such as the various dielectric oxides employed for waveguide lasers, the RF variant is the preferred option because it prevents charge build-up on the surface of the substrate and deposition of the insulator material on the electrodes. Beside configurations involving a single composite target material, co-sputtering from two targets (host material and rare-earth dopant ion precursor) or multiple targets have also been implemented for fabrication of rare-earth ion doped or co-doped waveguides, respectively. The growth process can be controlled through variation of a number of parameters, including process gas pressure and flow rate, substrate temperature, sputter power bias voltage,

and electrode distance. Films produced are characterized by low propagation loss as demonstrated with the growth of $Al_2O_3:Er^{3+}$ slab waveguides by co-sputtering, in which loss did not exceed 0.11 $dB \cdot cm^{-1}$ [186].

Diode sputtering is characterized by slow deposition rates and in many cases leads to overheating and structural damage of the substrate due to the extensive bombardment by the secondary electrons created in the ionization process. These issues can be simultaneously addressed with the use of *magnetron* sputtering. In the latter, magnets placed behind the electrode with the target material create a magnetic field that traps secondary electrons produced by collisions of inert gas atoms with free electrons near the cathode and above the target surface, forcing them to follow longer helical paths. This presents a twofold advantage: first, it prevents the electrons from bombarding the substrate and hence causing an increase in its temperature, and second, it increases the probability of ionizing collisions between electrons and neutral gas molecules by several orders of magnitude. The larger number of ions produced in this way increase the sputtering yields, allowing for use of low pressures compared to those required in diode sputtering (10^{-2} to 10^{-1} Torr). They also lead to high deposition rates on the substrate that range from 0.5 to 5 $\mu m \cdot min^{-1}$, as compared to values between 0.02 and 0.2 $\mu m \cdot min^{-1}$ typically attainable in diode sputtering.

Considerable work has also been carried out using a variant of the standard technique referred to as “reactive sputtering”, in which deposition is performed in the presence of a reactive gas. The latter is usually oxygen or nitrogen and reacts chemically with the atoms that are ejected from the target to form a compound layer (oxide or nitride) on the substrate. Depending on the reactive gas pressure in the chamber the reaction between the sputtered species and the gas species occurs either at the substrate or, near the cathode, with the compound in the latter case being subsequently transported to the substrate.

Sputtering is attractive in that it is carried out at relatively low temperatures and provided that no high temperature annealing of the sputtered layers is required, it allows for material growth on substrates with existing devices or functionalities produced in earlier steps of the fabrication flow without disturbing them. On the other hand, a disadvantage of this method is that it cannot ensure stoichiometric transfer of multicomponent target materials to the deposited films. This is related to changes in the target composition during its bombardment due to the different sputtering yields of the component materials, which in turn leads to a variation of the deposition reactions involved in the process with the time. Another practical challenge posed for the implementation of this method is that the discharge ignited to produce the plasma can be maintained only for a very narrow range of operating parameters. Amongst the different sputtering variants, RF-magnetron sputtering has attracted a lot of interest for fabrication of active waveguide devices and in most cases it has been implemented in combination with dry etching techniques. A great deal of efforts was directed to the development of $Al_2O_3:Er^{3+}$ amplifiers [187-189], leading to the demonstration of devices with an amplification bandwidth of 80 nm, covering the entire C-band [183]. Laser emission has been obtained from Nd-doped [190, 191], Er-doped [192] tantalum pentoxide (Ta_2O_5) ribs, Yb-doped aluminum oxide ($Al_2O_3:Yb^{3+}$) DBR channels [193], $Al_2O_3:Er^{3+}$ ring [194] and DFB channel waveguides [195] produced in sputtered layers of the corresponding materials, as well as from Nd-doped phosphate glass slab waveguides [196]. Recently, emission of 440-fs-short laser pulses from Er-doped aluminosilicate glass rib waveguides based on RF-sputtered films has been reported [44].

6.1.7. Contact and diffusion bonding

Contact- and diffusion bonding cannot be classified as material growth techniques, since they both rely on glueless bonding of existing bulk materials with reversed geometrical shapes for producing waveguides [197, 198]. Contact bonding, also known as thermal bonding, is a very

simple approach to fabricating high optical quality waveguides and the only difficulty in its implementation arises from the need for thorough treatment of the surfaces to be brought into contact to eliminate any defects or inclusions from their whole area. For this purpose, prior to bonding, their quality is enhanced through a stringent process that includes polishing to an atomically flat finish (the root-mean-square value should be within the sub-nanometer range), chemical treatment, and cleaning in aqueous environments to remove any organic or inorganic chemical residuals that can reduce the bond energy. After the completion of this process the surfaces are covered by a layer of hydroxyl (OH^-) groups and become hydrophilic, having the ability to adsorb a monolayer of water molecules under ambient conditions. When two surfaces that have been subjected to such a treatment are brought to close proximity, a strong adhesive bond would form between them at room temperature without any aid from chemical agents, solely as a result of long–range Van der Waal's attractive intermolecular forces. Once the materials are in contact and during the settling process of the bond a chemical reaction takes place, whereby the hydroxyl bonds (van der Waals bonds) are transformed to hydrogen bonds (covalent bonds), which are characterized by an enhanced strength. The bonding process can be accelerated by thermal annealing at a temperature that is sufficiently low to prevent inter-diffusion between the adjacent polished surfaces. To avoid thermal deformation or, build up of stress in the component materials, their heating and cooling rates prior and after thermal annealing are very slow, about ~10°C per hour. This process results in an increase of the strength of the covalent bonds across the interface of the two materials by several orders of magnitude, reaching eventually that of the chemical bonds in the starting materials. In this way the bond becomes monolithic, providing the waveguide structure with sufficient mechanical and chemical stability to withstand the polishing process of its end faces or, potential deposition of further cladding layers that may follow.

Thermal annealing is particularly useful for contact-bonded planar waveguides that are pumped with high-power diode lasers because it prevents separation of the bonded layers due to differential thermal expansion that can develop during laser operation. Furthermore, it assists the removal of absorbed gases and residual hydroxyl groups that are trapped at the interface of the bonded structures. Compared to the epitaxial growth techniques of LPE, MBE, and PLD discussed previously, contact bonding is largely independent of the material properties, allowing flexibility in the waveguide design. The only constraint imposed on the choice of materials is that they should have similar thermal expansion coefficients to prevent the development of stress and thermal gradients during thermal annealing and laser operation. One attractive feature of contact-bonded waveguides is that they exhibit low scattering losses (< 0.5 $dB \cdot cm^{-1}$ [20]) as a result of the atomically smooth interfaces of the bonded materials.

Development of diode-pumped planar waveguide lasers largely relies on the use of this technique, capitalizing on its ability to produce high-NA waveguides with large thickness that can easily capture the highly divergent pump beams. Therefore, it is not surprising that there is large number of reports on such devices, almost all of which are based on YAG:Nd^{3+} [16, 199-215] slab waveguides, largely due to the favorable thermo-mechanical properties of this crystal, which make it suitable for high-power diode pumping. Lasing was also reported for Nd^{3+}-doped BK7 glass-based waveguides fabricated by a combination contact bonding and ion exchange [216].

Finally, it should be noted that waveguide lasers have also been developed by diffusion bonding, which differs from contact bonding in that the bond formation is achieved via interdiffusion between the contacted surfaces. The process in this case is carried out in a vacuum chamber at considerably higher temperatures, by simultaneously heating and pressing the two materials. Parameters that determine the quality of the bond formed are the bonding temperature, the pressure exerted on the composite structure and the holding time. Laser operation was achieved in diffusion-bonded, YAG:Yb^{3+} channel waveguides [217, 218] using the configuration

shown in Fig. 22(a). The structures produced output powers of up to 1 W for approximately 3.5 W of absorbed pump power, corresponding to a slope efficiency of 43% [Fig. 22(b)].

6.1.8. Deposition from solutions

Solution processing is routinely used for formation of polymer planar waveguides and one of its main advantages is the simplicity of the whole process, which solely involves dilution of the polymer gain medium in an organic solvent and then its deposition on a substrate by spin coating, casting or injection molding techniques. The deposited layer is subsequently air-dried and baked at a temperature that depending on the polymer could range from 60 to 100ºC and last several hours. Other attractive features of this method are the low cost of the process equipment and its capability of producing low-loss waveguides, typically on the order of 0.1 $dB \cdot cm^{-1}$. However, there are also some drawbacks, which are related to the difficulty in obtaining high purity layers, the lack of precise thickness control and poor layer uniformity, and the relatively weak film adhesion to the substrate of interest.

It should be appreciated that the application of solution processing is not straightforward for all the polymer gain media. In the case of rare-earth doped polymer waveguides, fabrication has proven quite challenging due to the immiscibility of the rare-earth salt precursors with organic solvents. A convenient way of addressing this issue is to encapsulate the rare-earth ions with organic ligands [219], which provide enough co-ordination sites to bind the ions and form a stable complex that can be easily dispersed in polymer solutions. An additional advantage of this approach is that the complex shields the dopant ions from impurities in the surrounding polymer matrix that may quench their luminescence. Figure 23(a) shows the chemical structure of the organic complex $Nd(TTA)_3phen$ (where TTA and phen stand for thenoyltrifluoro-acetone and 1,10-phen anthroline, respectively) that has been used for development of Nd-doped channel waveguides lasers [220]. Conjugated polymers similarly exhibit poor solubility in organic

solvents, a problem that can be overcome by attaching soluble side chains to their backbone [221].

Another potential issue with regard to the operation of laser sources fabricated by solution processing is the emission quenching induced by overtone vibrations of C-H and O-H bonds that exist in the complex and the polymer (in its organic solvent), respectively. The impact of this effect can be mitigated by reducing the energy of the fundamental vibration through substitution of the hydrogen atoms by lower mass atoms, such as deuterium, fluorine, or chlorine [222]. This substitution process has little impact on the loss level of the waveguides produced, allowing for example development of fluorinated polymer waveguides with losses below the level of 0.2 $dB \cdot cm^{-1}$ at the telecommunication wavelength window around 1.5 μm. Finally, it is worth mentioning that the end faces of films fabricated by solution processing cannot be easily polished to an optical quality sufficiently high to allow formation of Fabry-Perot waveguide resonators. Therefore, in optically pumped waveguide lasers optical feedback in the resonator is often provided by distributed Bragg reflectors (DBR) or, distributed feedback (DFB) gratings of second-order that support out-of-plane emission.

Since solution processing is the main approach for fabricating polymer waveguide lasers, there is a large number of publications in the literature on operation of sources produced by this technique. These sources were primarily based on dye-doped [223, 224] and semiconductor polymers [221], while very recently laser emission has also been obtained from rare-earth doped polymer channel waveguides [220, 225]. In the latter, the polymer host was produced by crosslinking of 4, 4′-(hexafluoroisopropylidene)diphthalic anhydride (6-FDA) and 3, 4-epoxycyclohexylmethyl-3, 4-epoxycyclo-hexane carboxylate (UVR) [220] and subsequently doped with the organic complex $Nd(TTA)_3phen$. As it can be seen in Fig. 23(b), these lasers operated either on the quasi-three-level ($^4F_{3/2} \rightarrow {}^4I_{9/2}$) or, on the four-level ($^4F_{3/2} \rightarrow {}^4I_{11/2}$) transition near 878.0 nm and 1060.2 nm, respectively [225].

6.2. Methods for waveguide definition in an existing host

There is a wide range of fabrication methods that fall under this category and each of them is based on localized processing of the material either for inducing a refractive index change in its bulk or, surface or, for microstructuring its surface. All of these methods are applied for development of channel waveguides however, some of them can also be used for fabrication of slab waveguides. As discussed in preceding sections, provided that channel fabrication does not significantly increase loss, the laser sources produced exhibit lower laser thresholds and improved efficiency compared to their slab waveguide counterparts as a result of the enhanced lateral confinement of the pump and laser modes in the formerly unguided plane. Furthermore, they are capable of providing a near diffraction-limited, near circular, single-transverse-mode output beam, which is interesting for various applications requiring coupling with single-mode fibers.

6.2.1. Thermal ion indiffusion

The introduction of transition metal- or rare earth ions into crystalline materials by thermal in-diffusion is a well-established technique for fabrication of planar or channel waveguides of optical quality that is comparable to that of the corresponding bulk crystal. The first step of the fabrication process involves deposition of a uniform metal layer (the ion donor) with a thickness between 20 and 150 nm on a substrate (the ion acceptor) [226]. If fabrication of channel waveguides is intended, the deposited film is photolithographically structured to produce metal strip patterns. The crystal is subsequently subjected to high-temperature annealing either in an inert gas atmosphere or in a mixture of an inert gas and oxygen, whereby metal ions from the film or the strips diffuse into the surface region of the substrate due to the concentration gradient that

they experience. For planar slab waveguides an analytical expression for the concentration profile $C(y, t)$ of the indiffused ions can be derived by solving the one-dimensional diffusion equation

$$\frac{\partial C(y,t)}{\partial t} = D(T) \cdot \frac{\partial^2 C(y,t)}{\partial x^2} \tag{53}$$

where $D(T)$ is the diffusion coefficient of the dopant ion in the host material, given by the Arrhenius equation

$$D(T) = D_o \cdot \exp\left(-\frac{E_A}{k \cdot T}\right) \tag{54}$$

In the last expression, D_o and T are the diffusion constant and temperature, respectively, E_A is the activation energy for the diffusion process, and k is the Boltzmann constant. For a source of diffusant ions that is fully depleted after the completion of the diffusion process, the function describing $C(y,t)$ can be obtained by solving Eq. (53) and has a Gaussian form [227]

$$C(y,t) = \frac{N_{tot}}{2 \cdot \sqrt{\pi \cdot D \cdot t}} \cdot \exp\left(-\frac{y^2}{4 \cdot D \cdot t}\right) \tag{55}$$

where the term N_{tot}, is the total number of diffusant ions supplied per unit area and the product $2\sqrt{D \cdot t}$ is the effective diffusion depth, representing the depth at which the surface concentration is decreased by a ratio of 1/e. As it becomes evident from Eq. (55), $C(y, t)$ peaks at the surface [$C(0, t)$] and, as expected for sources completely depleted by the diffusion process, $C(0, t)$ decreases with diffusion time since the number of diffusant ions within the crystal is constant. The duration and the temperature of the annealing process depend on the diffusion coefficient, D; the temperature can indicatively span from 1000°C to 1950°C for the in-diffusion of Ti-ions into $LiNbO_3$ [228] and sapphire [229], respectively. It should be noted at this point that the diffusion process is in reality more complex and can be affected by a number of various other factors such as diffusion through existing crystal defects, varying diffusion rates with direction in the crystal lattice, outdiffusion of the diffusant ions from the crystal, chemical reactions that may occur between the diffusant ions and the crystal as well as existence of more than one diffusion

mechanism. The presence of dopant ions in parts of the substrate modifies the local refractive index in a way that its profile can be identified with that of the ion concentration. Since for most materials the refractive index exhibits a linear dependence on the ion concentration, it follows that the index profile of slab waveguides produced by thermal indifussion is graded in the vertical direction, while that of channel waveguides is graded in both the vertical and the horizontal direction. Graded-index waveguides have wavelength dependent modes, with the higher order ones preferentially propagating in the outermost areas of the waveguide, where the index contrast with the host material is lower. This makes essential the use of high-brightness pump sources for their longitudinal pumping in order to ensure a good spatial overlap of the pump mode with the fundamental mode of the in the channel and hence efficient laser operation. Figs. 24(a) and (b) show SEM pictures of a $LiNbO_3$ rib waveguide before, and after its indiffusion with Ti ions, respectively. As displayed in Fig. 24(c), the TE-and TM-mode profiles obtained from this structure are asymmetric due to the graded index profile in the rib.

An effective approach to optimizing laser performance is to introduce apart from the active ion, a second optically passive ion into the substrate by sequential indiffusion [33]. This provides flexibility in the waveguide design, allowing independent control of the waveguide parameters and its spectroscopic properties through variation of the concentration of the passive and the active dopant ions, respectively. The method of ion indiffusion can produce low-loss (< 0.1 $dB \cdot cm^{-1}$) waveguides with channel or, slab geometry and is suitable for fabrication of complex channel waveguide circuits. An obstacle to its implementation however, is that the choice of the diffusion pairs (host material and ions) is often limited by the lack of data on the diffusion characteristics. Furthermore, the need for simultaneously maintaining high temperatures and accurately controlling the temperature over extended processing times, which may extend up to tens of hours, poses a technical challenge. Ion-indiffused $LiNbO_3$:Er:Ti waveguide lasers have been the topic of vigorous research and there are a number of reviews summarizing their performance [33,

228, 231, 232]. Besides this material system, there are also reports on laser operation of channel waveguides defined by thermal ion indiffusion in a broad range of crystals, including $LiNbO_3$:Nd [233], $LiNbO_3$:Yb:Ti [234], $LiNbO_3$:Nd:Ti [235-238], $LiNbO_3$:Tm:Ti [239], $LiNbO_3$:Nd:Zn [240, 241], $LiNbO_3$:Tm:Zn [242], $LiTaO_3$:Nd [243], and Ti:sapphire [244].

6.2.2. Ion-exchange

Ion exchange is one of the most important and thorough researched techniques for fabrication of channel waveguides in glasses [245, 246]. Its underlying principle is similar to that of ion indiffusion, with the concentration gradient of ions being the force that drives the whole process. Ion exchange requires use of very simple instrumentation and is carried out by immersing a glass substrate into a low-temperature eutectic salt melt containing the diffusant ions, which are either monovalent alkali metal ions, usually Li^+, Cs^+, Rb^+, or K^+ or, other monovalent metal ions such as Ti^+, Ag^+ and Cu^+ [247]. To define channel waveguides, a mask of suitable material is applied on the substrate that leaves uncovered the areas to be transformed to waveguiding regions. The temperature of the melt is required to be lower than the glass transition temperature of the host substrate in order to preserve the original quality of the latter and mitigate undesirable ion diffusion in the lateral direction. For this reason, salts with relatively low melting temperature, such as nitrates (200-400ºC), are preferred for use as diffusant ion sources. Once the substrate is in the salt bath, ions from the latter diffuse into the glass and exchange with monovalent ions of smaller size and/or polarizability, usually Na^+, K^+ and occasionally Li^+, which are subsequently released into the melt [248]. For ion-exchanged waveguides with slab geometry, the normalized concentration profile $C(y,t)$ produced in the glass can be described by the one-dimensional diffusion equation [247]

$$\frac{\partial C(y,t)}{\partial t} = \frac{\partial}{\partial y}\left(\frac{D}{1-\alpha \cdot C(y,t)} \cdot \frac{\partial C(y,t)}{\partial y}\right) \tag{56}$$

Here, $\alpha = 1 - (D_{in}/D_{out})$ indicates the difference in mobilities of the in- and out-diffused ions with D_{in} and D_{out} being their self-diffusion coefficients, respectively. If the exchanged ions are equally mobile (α = 0), or, the concentration fraction of the in-diffused ions in the host is very small compared to that of the out-diffusing ions that are still present in the glass, then Eq. (56) takes the form of Eq. (53). Taking into account that the salt melt is practically an undepleted source of diffusant ions, and assuming that the field due to space charge effects is negligible the solution of Eq. (53) providing $C(y,t)$ is [227]

$$C(y,t) = C_s \cdot \left[1 - \int \exp\left(-\frac{y^2}{4 \cdot D \cdot t}\right)\right] = C_s erfc\left(\frac{y}{2\sqrt{D \cdot t}}\right) \tag{57}$$

where the term C_s is the maximum solubility of the incoming ions at the diffusion temperature and equals their concentration at the surface, and the product $2\sqrt{D \cdot t}$ is the effective diffusion depth d_{eff}, which corresponds to the point *erfc*(1) and indicates the depth of the waveguide produced. As it can be seen in Eq. (57), $C(y,t)$ and d_{eff}, both increase with increasing diffusion time.

Owing to the difference in size and polarizability of the exchanged ions, the parts of the glass that have been affected by this process exhibit a higher refractive index with respect to the substrate and therefore, can support light guidance. For planar waveguides the index profile $n(y,t)$ produced in the glass is given by

$$n(y) = n_S + \Delta n \cdot erfc\left(\frac{y}{2\sqrt{D \cdot t}}\right) \tag{58}$$

where Δn is the maximum index change at the surface of the waveguide and n_S is the refractive index of the substrate. A corresponding expression for channel waveguides can be derived by solving the two-dimensional diffusion equation; however, due to its complexity and lack of accurate boundary conditions at the mask edges this problem is often solved numerically [249].

Such an analytical expression for the index profile $n(x,y)$ has been derived for K^+–Na^+-exchanged waveguides in BK7 glass by a combination of experiment and modeling and is given by [250]

$$n(x,y) = n_S + \Delta n \cdot \exp\left(-\frac{x^2}{d_x^2}\right) erfc\left(\frac{y}{d_y}\right) \tag{59}$$

where d_x, and d_y refer to the half-width and the $erfc(1)$, of the width and depth of the ion indiffused area in the substrate, respectively. From Eqs. (58) and (59) it can be seen that the index of the ion-exchanged waveguides has a graded profile since it gradually decreases with increasing diffusion depth and width. The profile can become near circular by burying the waveguides after their fabrication via thermal annealing [251, 252]. Fabrication of buried waveguides with enhanced control over both their refractive index profile and the ion-exchange speed can be achieved by applying an electric field to the substrate [253, 254]. In this approach, known as *field-assisted* ion exchange, a metal film is deposited on one side of the substrate to serve as the negative electrode, while the molten salt solution where the substrate is immersed into, resumes the roles of the positive electrode and the source of cations [254]. Burying the waveguides brings with it the additional advantage of lower propagation loss, which for channel waveguides can be as low as 0.1 $dB \cdot cm^{-1}$. Figure 25(a) shows the index profile of an Ag-Na ion-exchanged phosphate glass channel waveguide produced with the field-assisted process. Its almost circular near-field mode profile at 1550 nm shown in Fig. 25(b) is similar to that of standard SMF-28 fibers, indicating the index symmetrization that can be achieved by the burying step. Waveguides fabricated with this approach were successfully operated as lasers, using the arrangement shown in Fig. 26, delivering an output power in excess of 160 mW with 46% slope efficiency [255].

Waveguide lasers in multicomponent glasses were also produced by *film-diffused* ion exchange [256], another variant of the standard technique, which similar to *field-assisted* ion exchange relies on the application of an electric field to drive the exchange process, allowing for single-step fabrication of buried waveguides. However, in this case the source of diffusant ions is

the deposited metal layer itself. The latter is overgrown by a gold or aluminum film, which serves as the cathode for the application of the electric field, whereas the anode can be a metal film applied on the back side of the substrate or, a melt of a mixture of salts. The salts are chosen such that the ionic proportions in their melt are nearly the same as those in the glass substrate in order to ensure that changes induced in the glass surface composition are only due to ions originating from the film. Film-diffused ion exchange has been applied for diffusion of copper [256] and silver ions [257] since these materials are amongst the few diffusant ions precursors that can produce stable metallic films. The refractive index of waveguides formed by either *field-assisted* or *film-diffused* ion exchange have step index profiles described by [258]

$$n(y) = n_S + \frac{1}{2} \cdot \Delta n \cdot \left[erfc\left(\frac{y - \mu \cdot E \cdot t}{2\sqrt{D \cdot t}} \right) + \exp\left(\frac{\mu \cdot E \cdot y}{D} \right) \cdot erfc\left(\frac{y + \mu \cdot E \cdot t}{2\sqrt{D \cdot t}} \right) \right] \qquad (60)$$

In the last equation, the product $\mu \cdot E$ is the drift velocity of the diffusant ions, with μ being their mobility and E the electric field applied. An advantage of these two processes relative to the standard ion exchange technique is that they can be accomplished at lower temperatures since the index profile of the waveguides produced is determined by the magnitude of the external field. Furthermore, they increase the speed of the exchange process and most importantly offer the possibility to control the spatial profile of the waveguides. There is a large number of reports in the literature on laser operation of rare-earth activated channel waveguides fabricated by thermal- or electric field-activated ion exchange in different glasses including phosphates [255, 259-273], silicates [274-280], and borosilicates [281-286].

6.2.3. Proton exchange

Proton exchange (PE) has been extensively used for fabrication of channel waveguides in photorefractive crystals, in particular $LiNbO_3$ and to a lesser extent $LiTaO_3$ [287]. The fabrication process is similar to the ion-exchange one described in the preceding paragraph, entailing immersion of the crystal substrate in an acid bath. The substrate is covered by a mask, which

leaves exposed the areas where the channel waveguides would be defined. The bath is usually based on a benzoic acid (C_6H_5COOH), although occasionally also stearic, succinic, nonane, palmic, pyro-phosphoric, phosphoric and sulphuric acids have been used, and is maintained at a relatively low temperature, typically between 150 and 300ºC. The acid acts as the proton (H^+) source since it dissociates at equilibrium as follows

$$C_6H_5COOH \leftrightarrow C_6H_5COO^- + H^+ \tag{61}$$

The presence of the crystal in the acid triggers a one-to-one replacement process of a part of the lithium ions in the exposed areas of the crystal by protons, the net result of which is the formation of a proton-rich layer ($H_xLi_{1-x}NbO_3$ or, $H_xLi_{1-x}TaO_3$) at the surface with a thickness that is typically between 1 and 10 μm. The corresponding reactions that describe this effect in $LiNbO_3$ and $LiTaO_3$ crystals are

$$LiNbO_3 + xH^+ \leftrightarrow Li_{1-x}H_xNbO_3 + xLi^+ \tag{62}$$

$$LiTaO_3 + xH^+ \leftrightarrow Li_{1-x}H_xTaO_3 + xLi^+ \tag{63}$$

The proton-rich layer produced exhibits a higher (~ 0.1 - 0.14) extraordinary (n_e) and a slightly lower ordinary (n_o) refractive index with respect to the corresponding values of the crystalline substrate. Therefore, it can guide light in one polarization, providing strong optical confinement due to its step-index profile. However, waveguides produced by this pure PE process are characterized by temporal instability at room temperature due to the presence of the metastable β-crystallographic phase, a behavior that is typical of structures containing high proton concentrations [288, 289]. Furthermore, they usually exhibit relatively high propagation losses (up to 1 $dB \cdot cm^{-1}$) [288] caused by surface scattering and have severely degraded non-linear coefficients [290, 291].

These problems can to some extent be solved by annealing in oxygen atmosphere at a temperature between 250 and 450^{o}C [291] to induce diffusion of the protons that have been incorporated in the crystal in the preceding exchange step, deeper into its bulk. The advantages of

this treatment are first, a partial restoration the nonlinear properties of the waveguides [292], and second, a transition from the β-phase to the stress-free α-crystallographic phase [289], which in turn leads to an improvement in their temporal stability and a decrease in their propagation loss. However, the annealing process brings with it some unwanted side effects, such as a decrease in the peak refractive index Δn_e of the waveguides, and an asymmetrization of their index profile, which exhibits a maximum value at the surface and decreases monotonically with increasing depth [293]. This asymmetry inhibits low-loss coupling to optical fibers and can be reduced by immersing the annealed proton exchanged (APE) waveguides in a eutectic melt of a mixture of nitrates ($LiNO_3$: KNO_3:$NaNO_3$) that is maintained at a temperature in the range between 250 and 330 ºC [294, 295]. This initiates an exchange between existing protons at the surface of the waveguide and lithium ions in the melt, a process that is termed reverse proton-exchange (RPE). RPE results in the formation of a two-layer waveguide system consisting of a nearly-proton-free $LiNbO_3$ (or, $LiTaO_3$) surface layer, in which the non-linear properties of the $LiNbO_3$ substrate are restored and acts as an ordinary index waveguide [296, 297], and a deeper layer, which is the extraordinary index waveguide that has been formed earlier by the APE process. This buried layer however, now exhibits a symmetric index profile, low propagation loss (< 1 $dB \cdot cm^{-1}$), and a relatively high refractive index contrast Δn of ~ $2x10^{-2}$.

It should be noted that fabrication of proton-exchanged waveguides can also be accomplished by using acids in vapor phase as proton sources [298-300]. An attractive feature of the vapor phase proton-exchange (VPPE) approach is that it is a single-step process and can yield high-quality waveguides without affecting their nonlinear optical coefficients, thereby bypassing the thermal annealing treatment that usually follows their fabrication.

One potential issue for PE waveguides in rare-earth doped crystals when development of amplifier and laser sources is the intended application is the decrease in the excited state lifetime of the rare-earth ions through non-radiative transitions. Such fluorescence quenching effects

occur due to the large number of high-energy optical phonons associated with O-H bonds that are formed by protons present in the waveguide. This problem is less severe for Nd^{3+} ions, whose fluorescence lifetime can be restored to a value very near to those in the crystal host by thermal annealing. The latter reduces the proton concentration, without causing any significant decrease in the refractive index contrast between the waveguide with the crystal host [301]. However, annealing is less effective in recovering the lifetime of Er^{3+} ions because the nonradiative relaxation in this case can be initiated even with a small number of OH-phonons [302]. Early work on laser sources using PE techniques focused on developing $LiNbO_3$:MgO:Nd waveguides by pure PE [303], which were operated as cw [304], Q-switched [305, 306], and mode locked [307] lasers. Laser oscillation was also demonstrated in channel waveguides produced in $LiTaO_3$:Nd^{3+} [301] bulk crystals and in Yb-indiffused $LiNbO_3$ planar slab waveguides (Fig. 27) by APE [308, 309]. The laser output characteristics and the emission spectrum shown in Fig. 28 originate from a $LiNbO_3$:Yb^{3+} channel waveguide laser fabricated by APE.

6.2.4. Ion/proton beam implantation

Implantation of ions and protons has proven a versatile technique for fabricating surface or buried waveguides with slab or channel geometries in crystals, glasses and other amorphous oxides [310-313], while recently fabrication of channel waveguides with excellent confinement of the propagating light has also been demonstrated in a rare-earth doped ceramic material [314]. In the implantation process, high-energy positive ions or, protons after experiencing acceleration and mass/energy selection, impinge on a substrate through a suitably designed mask and penetrate to a depth of a few microns below its surface, where the come to rest once they have completely lost their energy by exciting electrons along their trajectory. The penetration depth depends on the ion mass and energy as well as on the substrate material and its orientation. Material modification occurs only at the end of the ion track, underneath the surface where,

depending on the type, energy and dose of the ions, the interaction between the latter and lattice atoms can result in lattice disorder or even in amorphization. To ensure penetration depths in the micron range that are typically needed for fabrication of optical waveguides MeV, implantation energies are usually required.

Although waveguides can be formed by implantating optically active dopant ions in existing materials [312, 315], for waveguide lasers the approach usually followed is to define the waveguiding area within a bulk gain medium by implantation of passive ions. In this latter case, implantation in crystalline materials leads to a decrease in the refractive index of the affected areas, although, there are a limited number of papers in the literature reporting on positive index changes in $LiNbO_3$ [316], $KNbO_3$ [317], and YAG:Nd^{3+} [318] crystals. If the net result of implantation is a decrease in the refractive index, the strategy followed to produce waveguides is to create buried layers of reduced refractive index that surround and define the waveguiding area within the bulk crystal by acting as optical barriers. The latter can be broadened with the use of multi-energy implants to a thickness sufficiently large to prevent tunneling losses of the guided light. This process however, is often associated with a degradation of the waveguide quality due to an increase in ionization-induced effects at the crystal surface and along the ion track, which intersects the prospective guiding region. Aside from crystals, this method has also been applied for development of waveguides in glasses, in which the effect of implantation on optical properties strongly depends on their composition. Thus, in germanate and silica glasses it induces a compaction of the implanted areas, which is associated with an increase in refractive index whereas, in silicate, phosphate, and fluoride glasses the net result is a volume expansion of the affected areas and a decrease in their refractive index. Light guidance in this latter case is observed in a narrow layer adjacent to the implanted area that exhibits a relatively higher refractive index. Notably, for silicate, phosphate and fluoride glasses there is no report on waveguide lasers because the multiple energy implantations needed for broadening the optical

barriers in order to improve light confinement, usually result in formation of defects and a decrease in the index contrast between the guiding area and the surrounding area. Most of the reports to date on ion-implanted waveguide lasers are of structures with slab geometry produced in different crystals, including YAG:Nd^{3+} [319-321], YAG:Yb^{3+} [322], GGG:Nd^{3+} [323], $YAlO_3$:Nd^{3+} [324], and $LiNbO_3$:MgO:Nd^{3+} [325]; laser oscillation in channel waveguides was observed in YAG:Nd^{3+} [326], GGG:Nd^{3+} [327], and YVO_4:Nd^{3+} crystals [328]. In contrast, little work has been reported on laser operation of planar waveguides produced by ion-implantation in rare-earth doped glasses, with the only successful demonstration of laser oscillation being that in Tm-doped germanate glass [329]. Most of these laser sources were produced by implantation with helium ions (He^+) [320-327, 329], however successful use of carbon ions (C^+) was also reported [319, 328]. Recently, laser operation was demonstrated in YAG:Nd^{3+} planar waveguides produced by swift heavy-ion implantation, using Ar^{4+} [330] and N^{3+} [331] ions. Swift heavy-ion implantation is carried out with higher energies (typically tens of MeV). As a result, lower irradiation fluences are required for formation of waveguides (~10^{12} cm^{-2}) compared to normal implantation (10^{16}–10^{17} cm^{-2} for light ions and 10^{14}–10^{15} cm^{-2} for heavy ions). Refractive index changes in this case are induced through electronic excitations rather than by nuclear collisions with the target atoms.

Proton implantation has also attracted interest for fabrication of waveguide lasers primarily for its potential to induce deeper damage profiles as a result of the larger depths that protons can penetrate in the substrate compared to higher-mass ions. Furthermore, for many materials the effect of proton implantation on the quality of the guiding region is less detrimental relative to that of higher mass ions, thereby extending the prospects for developing efficient waveguide devices [332].

Although ion/proton implantation allows a great freedom of choice over the waveguide design, it suffers from the drawback that it creates defects in the guiding area, which are

responsible for an increase in propagation loss. To eliminate these defects the waveguides are subjected to high-temperature post-fabrication annealing, which however is undesirable in cases when their integration along with other functional components produced on the same chip in earlier fabrication steps is intended. Buried slab and channel waveguides exhibiting relatively low propagation loss (0.7 and 1 $dB \cdot cm^{-1}$ for the slab and channel structures, respectively) have been nevertheless produced without thermal annealing in undoped sapphire [332, 333] and Ti:sapphire crystals [333, 334]. Figure 29 shows the implantation design of the Ti:sapphire channel waveguide lasers, while in Figs. 30(a) and (b) the simulated and the measured fluorescence intensity profiles of a single-mode, proton-implanted Ti:sapphire channel waveguide are displayed. Proton implantation has also been successfully implemented for development of YAG:Nd^{3+} [319, 335, 336] and GGG:Nd^{3+} [337] slab waveguide lasers.

6.2.5. Proton beam writing

Proton-beam writing (PBW) allows for three-dimensional (3D) micro- / nanostructuring of optical waveguides in various materials. It involves scanning of a focused proton beam typically with MeV energy, and micron or even sub-micron size within the target material [Fig 31(a)] to induce local structural modifications at micron/submicron scales at the end of range of the penetrating protons. This leads to localized alteration of bond polarizability or material density at the nuclear collision volume, and in turn to a refractive index change [338]. An advantageous feature that differentiates this method from conventional ion/proton implantation is that waveguide formation can be accomplished in a single step without masking the substrate. Furthermore, due to energy and momentum mismatch of the incoming protons with the electrons in the target material, the former travel in a straight line and can penetrate in larger depths without inducing any electronic excitations or significant refractive index changes along their trajectory. Buried waveguides are formed within the bulk of the material at a depth that can be

well defined by controlling the beam energy [Fig. 31(b), (c)] [339]. Waveguide amplifiers and lasers have been fabricated using the PBW technique in YAG:Nd^{3+} crystals [340] and Er^{3+}:Yb^{3+} doped phosphate glasses [341].

6.2.6. Optical writing

Optical writing is a relatively new approach for realization of channel waveguides that utilizes a scanned laser beam with a suitably chosen wavelength to permanently modify the local refractive index of a material. This method offers the possibility of single-step fabrication, bypassing the need for photolithographic patterning and is particularly suitable for producing large-area photonic integrated circuits, for which the use of masks is impractical. Furthermore, it has the additional benefit that the characteristics of the waveguide can be precisely tuned by controlling laser parameters such as intensity, fluence and exposure time, thereby enabling optimization of the waveguide laser performance.

In early demonstrations of this technique the photosensitivity of certain types of glasses to ultra-violet (UV) wavelengths was exploited for writing surface channel waveguides with the use of UV cw lasers [342, 343]. For waveguides fabricated with this approach, refractive index contrast values up to ~10^{-2} with respect to the host glass [343], and propagation loss as low as 0.2 dB·cm [344] were reported. UV laser writing has proven successful in accomplishing complex index engineering functions as best exemplified by the demonstration of waveguide writing and encoding Bragg gratings in a single step [345] using the arrangement shown in Fig. 32, an approach that would be useful amongst other potential applications for rapid prototyping of narrow line emitting waveguide lasers. In that context there has been a steadily increasing interest in applying direct UV writing for development of integrated devices, including planar waveguide laser sources. The latter have been realized in different glasses, such as silica [144], germano-borosilicate [216], lead silicate [346], and gallium lanthanum sulphide (GLS) glass [347], using

Nd^{3+} ions as activators. Despite the simplicity and speed of this fabrication method, there are some practical limits to its implementation that include: (i) the insufficient level of photosensitivity that many glasses exhibit to the emission wavelengths of commercially available UV lasers and, (ii) the proximity of their photosensitivity and absorption spectral bands. The latter prevents the laser beam from penetrating into large depths in the material, thereby precluding writing of waveguides embedded in its bulk.

In recent years, a more sophisticated implementation involving processing with tightly focused femtosecond (fs) laser pulses has emerged, permitting rapid device prototyping in both absorptive and transparent substrates [348-350]. An advantage of this method is that it allows three dimensional writing within the bulk of a sample simply by translating the sample with respect to the incident laser beam and changing the focal depth of the latter. One important feature of this process is that the optical energy is absorbed and transferred to the lattice through nonlinear absorption and avalanche ionization on a significantly shorter timescale than that required for heat transfer. This, in combination with the tight focusing, results in highly localized phase or structural modifications and in turn in permanent changes of the refractive index in the focal volume inside the material, without causing any collateral damage to the surrounding areas by thermal diffusion. For transparent substrates, the writing process is independent of the material and therefore, optical waveguides can be realized in compound substrates of different materials. The intensity required for waveguide writing is determined by the duration and energy of the laser pulses and the NA of the focusing objective. Writing with low NA objectives leads to formation of waveguides with elliptical profiles however, a number of approaches to symmetrising the profile have been reported, including pulse shaping prior to its focusing [351], use of a slit aperture [352] or of a two-dimensional deformable mirror [353], and multiple scan writing [354]. Other parameters that affect the writing process are the scanning speed, pulse shape as well as orientation and polarization of the fs-laser beam [355, 356].

The underlying mechanism of waveguide formation by fs laser writing depends on the nature of the processed material. Exposure of glasses to ultra-sort pulses results in melting and re-solidification of the affected areas, the net result of which is a contraction of their volume and an increase in the refractive index, typically in the range 10^{-2}-10^{-3}, that is supportive of light guidance. Propagation loss of less than 0.2 dB·cm^{-1} was demonstrated in waveguides fabricated with this approach [357]. In contrast, fs laser processing of crystals and α-quartz leads to an expansion of the local volume and in turn to a decrease in the local material density and refractive index. Light guidance in these materials is observed along the boundary between the irradiated and the non-irradiated zones, where an increase in the refractive index of the order of 10^{-3} is observed due to the compression induced by the volume expansion of the processed region. However, the rather high propagation loss in this boundary area, which exceeds 2 dB·cm^{-1}, limits significantly the prospects for efficient waveguide laser sources [358].

There has been intensive research activity in producing passive and active waveguide devices in glasses over the last years, resulting in the development of laser sources in rare-earth doped phosphate [359-364], oxyfluoride silicate [365], bismuthate [366] fluorogermanate [367] and fluorozirconate [368] glasses. Fabrication of waveguides that can support laser oscillation in crystals can be more challenging than in glasses, requiring a strategy similar to that followed in fabrication of channel waveguides by ion implantation, namely engineering of low-refractive-index barriers that surround and confine the intended waveguide channel region. Following this approach, depressed cladding buried channel waveguide lasers were produced in YAG:Nd^{3+}crystals [369]. The refractive index change within the laser mode in these waveguides was $\Delta n \sim 4\text{x}10^{-4}$ and the propagation loss about 0.3 dB·cm^{-1}. As shown in Fig. 33 their cross section had a rectangular shape in order to match the mode profile of the laser diode used for pumping. In more recent reports however, waveguides in laser crystals were defined using a simpler approach, involving machining of a pair of parallel closely spaced (on the order of a few

micrometers) tracks in their bulk. Light in this case is confined in between the tracks as a result of the stress-induced birefringence developed in their surrounding regions. Femtosecond laser machining led to the development of channel waveguide lasers in YAG:Nd^{3+} [370, 371], $GdVO_4$:Nd^{3+} [372], YVO4:Nd^{3+} [373] YAG:Yb^{3+} [374], $KGd(WO_4)_2$:Yb^{3+} and $KY(WO_4)_2$:Yb^3 [375] crystals as well as in YAG:Nd^{3+} [376] and YAG:Yb^{3+} [377] bulk ceramics. A microscope image of a pair of tracks produced by fs-laser irradiation in a YAG crystal is displayed in Fig. 34(a), whereas Fig. 34(b) shows a CCD image of a laser mode obtained from a waveguide defined by two such tracks in a YAG:Nd^{3+} crystal. An interesting approach to fabricating waveguides with this technique was implemented in LiF crystals and involved formation of laser active F_2 color centers inside their bulk by exposure to fs-laser pulses. Micro-gratings that were subsequently encoded holographically with the use of fs-laser irradiation led to the development of distributed feedback (DFB) waveguide lasers [378].

Finally, another approach to optically writing channel waveguides is by using the self-focusing effect, induced by permanent refractive index changes through an one-photon or two-photon photosensitivity process in photosensitive glasses [379], or via laser-initiated free radical polymerization in polymers [380] and sol-gel hybrid (organic-inorganic) materials that contain photopolymerizable acrylate monomers [381]. The photopolymerization process can lead to refractive index changes of up to $4x10^{-2}$ [380]. Reports on lasing are of waveguides written in two different photopymerizable organic gain media. These were the resin KAYARAD DF-803N doped with the NK-125 dye (emission band from 700–900 nm) [382, 383], and a copolymer of pentaerythritol triacrylate (PETA) and benzyl acrylate (BA) doped with the LDS798 dye, (emission band from 770 to 830 nm) [384]. In each case, suitable photoinitiators for polymerization at the exposure wavelength were introduced in the precursor solution of the gain medium. Self-written cylindrical waveguides with constant diamenter were fabricated by exposing the gain medium to cw laser irradiation of 488-nm or, 405-nm wavelength for the NK-

125- and the LDS798-doped gain medium, respectively, through two fibers positioned at its opposite sides, as shown in Fig. 35. The typical exposure power and duration were 20 μW and 30 s, respectively. This method has proven capable of producing single mode waveguides [385, 386] and holds therefore promise for fabrication of optical interconnects and three-dimensional waveguide circuitry.

6.3. Surface structuring techniques

Surface structuring is applied to produce channel waveguides of strip, rib, or, strip-loaded type, and is accomplished either by material etching in combination with standard photolithographic techniques or, with the use of imprinting technologies such as soft lithography and nanoimprint lithography or, by laser ablation. Amongst these methods etching is the most established approach, involving a variety of processes that are divided into two categories, dry etching and wet (chemical) etching, depending on whether gaseous or liquid chemical etchants are used for material removal, respectively. Parameters that are considered for choosing the appropriate etching technique are the etching rate and controllability, the material selectivity, as well as the etching anisotropy and damage induced to the material by the etching process.

6.3.1. Dry etching

Dry etching techniques are widely used in conjunction with photolithography in the semiconductor and silica-on-silicon technologies for integrated circuit manufacturing. They are also commonly applied for microfabrication of channel waveguides in a variety of materials for development of laser sources and usually represent the last step of the whole fabrication process that begins with the deposition of an active layer using one of the deposition techniques discussed previously. Dry etching involves selective material removal by means of ion-assisted processes such as ion beam etching (IBE), reactive ion etching (RIE), and inductively coupled plasma (ICP)

etching. These processes are highly anisotropic due to the directionality of the ion bombardment, which is maximized when the incoming ion flux is normal to the surface of incidence. The RIE and ICP apparatus consist of a vacuum chamber with two parallel electrode plates, where the cathode serves as a substrate holder and is powered by a RF supply. By contrast, IBE arrangements are based on a tripode configuration, in which the substrate is placed on a third electrode and is decoupled from the plasma source (termed in this case "remote plasma"). The IBE process is carried out in the presence of a noble gas, typically argon, which is ionized by a glow discharge that is ignited and maintained by the RF field. This generates a stream of accelerated argon ions with relatively high energies (500-800 eV) that bombard the substrate, thereby removing material from its surface through physical sputtering. The argon gas pressure in the chamber is usually quite low, typically about 10^{-4} Torr, resulting in long mean free paths for the ions. The etch rates that can be achieved strongly depend on the ion beam angle with respect to the substrate. One drawback of the IBE process is the extended damage that is often inflicted on the processed sample by the physical sputtering process, which in turn has an impact on the loss level of the waveguide. Furthermore, it is difficult to produce channel waveguides with vertical sidewalls as required by some applications. Other potential limitations of this technique include: (i) the appearance of trenching along the waveguide sidewalls due to the glancing incidence of ions, (ii) redeposition of material removed from the bottom of the grooves that define the channels on the sidewalls, (iii) backscattering of etching products and their redeposition on the substrate (iv) non-uniform etching due to deviation from the perpendicular ion incidence caused by inhomegeneities in the electric field on the substrate [387]. Figure 36 shows a schematic of the steps followed for fabrication of rib waveguides in PLD-grown Ti:sapphire layers using a combination of photolithography and IBE [58]. The ribs produced (Fig. 37) exhibited a propagation loss of 0.2 $dB \cdot cm^{-1}$ with respect to the background loss of the slab host waveguide layer.

In contrast to IBE, the gases utilized in the RIE process are chemically active and typically based on fluorine since this particular gas chemistry provides high etch rates. However, depending on the processed material, also chlorine, bromine or iodine-based gas chemistries can be used. Similar to IBE, the RIE process starts with the formation of plasma through the ignition a glow discharge in the process gas, which dissociates and/or ionizes its molecules. The ions in the plasma are directed to the substrate by the RF-bias and bombard its surface at normal incidence with energies typically in excess of 200 eV, thereby removing material by both chemical reactions with the surface and physical sputtering. The process gas pressures required to ensure self-sustained plasma are considerably higher compared to the IBE process, typically ranging from 10 to 300 mTorr. Consequently, the electron mean free paths are smaller than the distance between the two electrodes, which in turn reduces the anisotropy of the etching process and the aspect ratios that can be achieved. Process optimization requires careful balancing of the physical and chemical etching components and can be achieved by varying a number of parameters, such as RF power and frequency, flow rate and composition of the process gas, background pressure and substrate temperature. Channels with vertical profiles can be obtained by passivation of their sidewalls through a polymer deposition process that is established and occurs in parallel with material etching. For this purpose gaseous etching agents with a composition that supports the polymerization process such as hydrofluorocarbons or, mixtures of chlorofluorocarbons with hydrogen, are introduced to the plasma. The selectivity of the etching process depends critically on the composition of the process gases and improves with the composition approaching the polymerizing point. In RIE the involvement of the second, chemical component in the etching process leads to significantly higher material removal rates with respect to those of the two individual etching components. An example that illustrates this fact is the etch rates of Ti:sapphire crystals obtained by RIE and IBE, which are approximately 45 $nm \cdot min^{-1}$ [388] and 12 $nm \cdot min^{-1}$ [389], respectively. The etch rates attainable in the RIE process can be

further enhanced by increasing the plasma density, however, in practice this would also lead to higher ion energies, since both the plasma density and the ion energy in RIE configurations are modulated by the same RF power. The high ion energies have a detrimental effect on the patterning quality as they can cause excessive damage to the photolithographic mask and degradation of the surface quality of the sample.

ICP etching is an effective way to significantly increasing the etch rate without affecting the surface quality. In a typical ICP configuration (Fig. 38), the plasma is inductively driven by an RF-powered magnetic field, while an RF bias that is controlled separately by another RF generator is applied to the cathode to enhance the anisotropy of the etching process by creating a directional electric field. This mode of plasma excitation leads to larger electron mean free paths compared to RIE thus allowing for use of low ($\leq$ 10 mTorr) process gas pressures, which in turn increases the diffusivity and mobility of the reactive species. This allows use of high ion densities (~10^{11} ions/cm^{-3} as compared to >10^{9} ions/cm^{-3} in RIE) without increasing the ion energy, since the ion-producing electrons are coupled to the magnetic field. The ICP is advantageous for etching of waveguides in dielectric gain media because it ensures enhanced control over the critical dimension, and higher etching rates and aspect ratios compared to the other two ion processes discussed previously. The RIE and ICP techniques are in general capable of producing channel waveguides in different crystalline materials whose dimensions can be several micrometers in height and width and exhibit smooth and vertical sidewalls and very low optical loss. A propagation loss as low as 0.1 dB·cm^{-1} with respect to the background loss of the host film was reported for rib waveguides fabricated in amorphous Al_2O_3 and polycrystalline Y_2O_3 films using ICP etching with BCl_3/HBr (50%:50%) gas plasma [391].

Laser oscillation was demonstrated in rib waveguides fabricated by IBE using Ar^+ ions in a range of materials, such as PLD-deposited Ti:sapphire [14], LPE-grown GGG:Yb^{3+} [74], GGG:Nd^{3+}[75], $KY(WO_4)_2$:Gd^{3+}, Lu^{3+}, Yb^{3+} [82, 83] and $KY(WO_4)_2$:Gd^{3+}, Lu^{3+}, Tm^{3+} layers

[84], and in RF-sputtered $Ta_2O_5:Nd^{3+}$ [191] and $Ta_2O_5:Er^{3+}$ [192] films. There are also a number of reports on laser operation of RIE-microstructured rib waveguides in layers based on Er/Al-doped germanosilicate glass [129, 130] and $Ta_2O_5:Nd^{3+}$ [190], as well as in silicon [42, 43]. Finally, ICP has been successfully implemented for development of $Al_2O_3:Yb^{3+}$ [193] and $Al_2O_3:Er^{3+}$ [194, 195] integrated waveguide lasers based on DBR [193], ring [194], and DFB resonators [195].

6.3.2. Wet chemical etching

Wet chemical etching is applied for fabrication of channel waveguides in various single-crystalline or polycrystalline materials, as well as for cleaning and removal of work damaged areas and roughness from optical surfaces after dry etching. This method does not require any sophisticated apparatus and surface patterning is performed by covering parts of the substrate with suitable masks that are inert to the etchant or exhibit considerably slower etch rates than the material to be etched. The structure is then immersed for a certain time in a suitable etchant solution that is maintained at an appropriate temperature and stirred to eliminate air bubbles. The interaction between the etchant and the exposed surface areas results in material removal at their interface. The most important parameters in chemical etching are bias (undercut), selectivity, feature size control. The etchants that are commonly used are categorized as isotropic, which are solutions of typically nitric (HNO_3), hydrofluoric (HF) and acetic (CH_3COOH) acids, and anisotropic (typically alkaline aqueous solutions). The former etches at an equal rate in all crystallographic directions, which leads to large bias when etching thick films. By contrast, etching with anisotropic etchants results in material removal at different rates depending on the orientation of the exposed crystal plane. The attractive features of wet etching are the enhanced selectivity and speed of the etching process, which for anisotropic etching reaches 0.1 $\mu m \cdot sec^{-1}$, and the limited damage that is induced to the lattice as compared to dry etching. On the other

hand, there are also some downsides such as the need for using undesirable and potentially harmful chemicals and the difficulty to control precisely the etch depth and the profile of the structures produced, in particular to achieve vertical pattern transfer.

Processing of hard crystalline laser hosts poses a challenge as many of these materials are either resistant to all the common etchants or, exhibit significantly lower etch rates than the materials usually employed as masks. This problem can be overcome by inducing localized damage to the crystal lattice prior to wet etching, thereby exploiting the preferentiality exhibited by most acidic solutions to etch with a higher rate the structurally modified areas. A number of approaches to producing areas susceptible to etchants in different crystalline materials have been reported, including exposure to UV pulsed laser irradiation [392], proton exchange [393], and ion beam implantation [394]. Ion beam implantation with light ions such as He^+ followed by wet etching with H_3PO_4 acid was successfully implemented for fabrication of rib channel waveguides in Ti:sapphire thin films with etch depths larger than 1 μm [394].

6.3.3. Soft Lithography and nanoimprint lithography

Soft lithography [395, 396] and nanoimprint lithography (NIL) [397] are mechanical imprint techniques that can replace conventional photolithographic methods for fabrication of optical waveguides and surface relief Bragg gratings in polymers [398, 399], and inorganic-organic hybrid materials produced by sol-gel processing [178-180, 400].

Soft lithography is the collective name used for a group of patterning techniques that are well suited for fabrication of mesoscale structures with sizes ranging from 10 to 100 μm. All these techniques rely on elastomeric molds to print directly onto the surface of the material the reverse of a predefined feature by stamping. The molds are produced with the replica molding technique, which involves casting of an elastomeric material on a master with the desired micro-pattern imprinted in its surface. The use of elastomers is of key importance for the success of the entire

process because they can ensure full, conformal contact on the micrometer scale, even with non-planar surfaces without requiring exertion of significant pressure. This capability was best exemplified by the successful printing of Bragg gratings directly on rib waveguides based on the small molecular-weight semiconductor molecule Alq_3 doped with dye DCM2 [401], as illustrated in Fig. 39. Amongst the various elastomeric materials poly (dimethylsiloxane) (PDMS) is the most commonly used, owing to its chemical inertia and the ease that it can be released from the processed area leaving even complex and fragile structures completely unaffected. Furthermore, PDMS is optically transparent to wavelengths down to 300 nm, allowing cross-linking by UV light exposure of the prepolymers that are being molded.

There are a number of variants of this technique, amongst which micromolding in capillaries (MIMIC), solvent-assisted micromolding (SAMIM), and liquid imprinting have been used for development of waveguide lasers. In MIMIC a PDMS mold makes conformal contact with a surface, thereby forming a pattern with channels on it. A low-viscosity liquid prepolymer is then placed at the open ends of the network of channels, filling them by capillary action. The prepolymer is subsequently cured into a solid and the PDMS mold is removed, leaving the desired pattern on the substrate. Figures 40(a) and (b) show SEM and confocal microscope images of undoped and rhodamine 6G (R6G)-doped mesostructured silica ridge waveguides, respectively, that have been produced by MIMIC. In the doped structures [Fig. 40(b)], amplified spontaneous emission (ASE) [178, 179] and lasing [180] were demonstrated. In SAMIM the PDMS mold used for imprinting is wetted with a suitable solvent and brought into contact with the surface of the polymer, thereby causing a thin layer of the latter to dissolve. The fluid produced conforms to the surface topology of the mold and as the solvent dissipates and evaporates the polymer solidifies to form relief structures of the reversed pattern of that on the surface of the mold. Finally, liquid imprinting entails pressing of the elastomeric mold on a liquid film of a solution of the polymer gain medium, until the solvent has completely evaporated. Both

SAMIM [402] and liquid imprinting [403] have been used for encoding gratings in conjugated polymers to produce DFB waveguide lasers.

There has been considerable interest in using NIL techniques for fabrication of Bragg gratings to develop organic DFB waveguide lasers. For this purpose three different NIL variants were successfully implemented, namely hot embossing [404, 405], ultraviolet NIL (UV-NIL) [180, 224, 400, 406, 407] and room temperature (RT) NIL [408]. Hot embossing is suitable for imprinting on thermoplastic polymers and is accomplished by simultaneously heating the polymer above its glass transition temperature, which depending on the type of polymer could range from 100 to 300°C, and pressing a SiO_2 master mold on its surface. The mold has the grating imprinted on its surface by electron beam or reactive ion etching. The imprinting process is carried out under vacuum or, in an inert atmosphere to prevent degradation of light emission from the prospective polymer laser due to heating. The UV-NIL approach on the other hand, is ideal for processing of UV sensitive polymers and is carried out at room temperature with the use of UV transparent templates. The template with the desired pattern is initially pressed on the polymer surface and exposed to UV light; it is subsequently removed, leaving the imprint of the reverse of their pattern on the polymer surface. Figure 41(a) shows a SEM image of a Bragg grating imprinted in a dye-doped polymer slab waveguide by UV-NIL. The emission spectrum obtained from the DFB laser based on this grating is displayed in Fig. 41(b), together with a picture of the waveguide during laser operation. Finally, with regard to the RT-NIL approach, it has been employed for patterning of waveguides in gain media with poor thermoplastic properties. It is usually carried out with silicon molds in air and has been implemented for fabrication of laser sources based on semiconducting oligothiophene layers [409, 410]. An advantage of RT-NIL over hot embossing is that it allows for successive imprinting different features on the same layer.

In contrast to optical lithography, NIL processes are not affected by spatial resolution limitations, allowing printing of features with significantly smaller size (10 nm or less). Furthermore, they offer the possibility of single-step, 3-D patterning by employing templates with 3-D imprinted structures and can be carried out using hard or soft molds, as required. Soft lithography and NIL have a number of other advantages over optical lithography, such as cost effectiveness, simplicity, speed, and suitability for large-area fabrication. However, as contact lithographic technologies they inevitably introduce greater particle contamination to the processed layers and provide less accurate overlay alignment.

6.3.4. Laser ablation

Surface patterning by material ablation with the use of nanosecond [411-413] or femtosecond [414] pulsed lasers is another method that has been studied for development of channel waveguide lasers. Of key importance for the optical quality of the structures produced is to avoid any dissipation of the deposited energy beyond the volume that is ablated during the pulse. This condition is fulfilled if the thickness of the layer ablated per pulse is on the order of the heat penetration depth or, of the optical penetration depth, depending on which is larger [415]. For materials with high thermal conductivity nanosecond pulses are too long to fulfill this requirement and therefore, the quality and resolution of surface patterning is not as high as with femtosecond pulses. The scale of effort on using laser ablation for fabrication of channel waveguides is rather low since it is perceived to be difficult to overcome problems related to formation of debris on top of the structures, re-deposition of the ablated material and formation sub-wavelength ripples along the side-walls that increase the level of scattering loss in the structures.

7. Conclusions

With the significant improvement in optical quality of planar waveguides over the last years, laser sources based on such structures have started realizing their enormous potential that is associated with their geometry. This geometry concept is largely responsible for a number of unique properties and benefits that waveguide lasers possess and offer, respectively, as compared with other classes of lasers in terms of performance, size, functionality, and practicality. The combination of these characteristics have driven their rapid development and facilitated their penetration into different applications, many of which had been formerly dominated or, could not be addressed by other classes of lasers.

The advances achieved in the field of waveguide lasers have gone hand-in-hand with the development of a broad range of fabrication technologies. The latter have played a critical role in refining several parameters that are important for optimal device performance and provided exactly what these laser sources needed to progress from proof-of-concept demonstrations to practical applications. The fabrication techniques discussed in the preceding sections of this review are diverse in their operational characteristics, capabilities, and materials they can process and either represent adaptations of technologies that have already moved into the stage of maturity or, are new and still remain in a development phase. In many cases, the overall fabrication approach followed for the realization of waveguide gain media combines different techniques, thereby exploiting their individual strengths to achieve specific device characteristics. The broad span of applications and the different requirements they placed upon an ideal waveguide laser source and its operating properties have fuelled interest in introducing novel fabrication processes or, improving existing ones that are approaching their physical limits.

When one contemplates the past two decades of research, it becomes clear that another major contributing factor to the progress in waveguide lasers has been the fruitful entanglement of ideas

from different disciplines, most notably optics, laser physics, materials science and nonlinear optics. The field of waveguide lasers remains an active topic of research and further progress, is also likely to be boosted by combinations of ideas from these disciplines. To underpin future research and development of such sources for specific applications technical advance in their fabrication technology focuses on the following directions:

(i) Downsizing the waveguide laser systems and increasing the scale of their integration with existing semiconductor and optoelectronic circuitry, fiber technology, and various on-chip applications.

(ii) Introducing new gain media to overcome limitations on laser performance imposed by the available material characteristics, and developing suitable fabrication technologies for these materials along with the process equipment and integration required.

(iii) Scaling the output power of waveguide laser sources and expanding the range of both their wavelength coverage and the temporal formats produced. Materials solutions and innovative design concepts for laser cavities are both expected to equally contribute to address these issues.

In conclusion, this paper aimed to highlight the advantages conferred by the planar waveguide geometry for efficient, compact, and functional laser sources, the pursuit of which has inspired a great deal of research in waveguide fabrication technology. It also aimed at setting a context for the second part of this review, in which waveguide gain media that are commonly used or, are currently attracting a lot of research interest are presented. Furthermore, the broad range of operational modes achieved using the waveguide laser technology is also discussed, thereby underlining the advantages that can be gained by combining fabrication with device research.

REFERENCES

[1] E. Snitzer, Phys. Rev. Lett. 7 (1961) 444-446.

[2] R. J. Mears, L. Reekie, I. M. Jauncey, D. N. Payne, Electron. Lett. 23 (1987) 1026-1028.

[3] E. Desurvire, R. J. Simpson, P. C. Becker, Opt. Lett. 12 (1987) 888-890.

[4] K. Okamoto, "*Fundamentals of Optical waveguides"* (Academic Press 2006)

[5] B. E. A. Saleh, M.C. Teich "*Fundamentals of Photonics* " (Wiley 2007)

[6] K. Kubodera, K. Otsuka, J. Appl. Phys., 50 (1979) 653-659.

[7] F. Moulton, IEEE J. Quantum Electron. 21 (1985) 1582-1595.

[8] T. Y. Fan, R. L. Byer, IEEE J. Quant. Electron. 23 (1987) 605-612.

[9] W. P. Risk, J. Opt. Soc. Am. B 5 (1988) 1412-1423.

[10] T. Taira, W. M. Tulloch, R. L. Byer, Appl. Opt. 36 (1997) 1867-1874.

[11] M. J. F. Digonnet, C. J. Gaeta, Appl. Opt. 24 (1985) 333-342.

[12] W. A. Clarkson, D. C. Hanna, J. Mod. Opt., 36 (1989) 483-498.

[13] A. A. Anderson, R. W. Eason, L. M. B. Hickey, M. Jelínek, C. Grivas, D. S. Gill, N. A. Vainos, Opt. Lett. 22 (1997) 1556-1559.

[14] C. Grivas, D. P. Shepherd, T. C. May-Smith, R. W. Eason, M. Pollnau, Opt. Express 13 (2005) 210-215.

[15] N. P. Barnes, IEEE J. Sel. Top. Quantum Electron. 13 (2007) 435-447.

[16] C. L. Bonner, T. Bhutta, D. P. Shepherd, A. C. Tropper, IEEE J. Quantum. Electron. 36 (2000) 236-242.

[17] W. A. Clarkson, J. Phys. D: Appl. Phys. 34 (2001) 2381-2395.

[18] H. Kang, H. Zhang, D. Wang, Appl. Phys. Lett. 95 (2009) 181102.

[19] H. J. Baker, J. R. Lee, D. R. Hall, Opt. Express 10 (2002) 297-302.

[20] D. P. Shepherd, S. J. Hettrick, J. I. MacKenzie, C. Li, R. J. Beach, S. C. Mitchell, H. E. Meissner, J. Phys. D 34 (2001) 2420-2432.

[21] J. M. Eggleston, T. J. Kane, K. Kuhn, J. Unternahrer, R. L. Byer, IEEE J. Quantum Electron. 20 (1984) 289-301.

[22] K. Sueda, H. Takahashi, S. Kawato, T. Kobayashi, Appl. Phys.Lett. 87 (2005) 151110.

[23] J. Webjörn, F. Laurell, G. Arvidsson, IEEE Photonics Technol. Lett. 1 (1989) 316-318.

[24] K. Mizzuchi, K. Yamamoto, Appl. Phys. Lett. 60 (1992) 1283-1285.

[25] C. J. van der Poel, J. D. Bierlein, J. B. Brown, S. Colak, Appl. Phys. Lett. 57 (1990) 2074-2076.

[26] L. A. Eyres, P. J. Tourreau, T. J. Pinguet, C. B. Ebert, J. S. Harris, M. M. Fejer, L. Becouarn, B. Gerard, E. Lallier, Appl. Phys. Lett. 79 (2001) 904-906.

[27] M. Ravaro, L. Lanco, X. Marcadet, S. Duccia, V. Berger, G. Leo, C. R. Physique 8 (2007) 1184-1197.

[28] B. Bijlani, P. Abolghasem, A. S. Helmy, Appl. Phys. Lett. 92 (2008) 101124.

[29] J. A. Armstrong, N. Bloembergen, J. Ducuing, P. S. Pershan, Phys. Rev. 127 (1962) 1918-1939.

[30] M. M. Fejer, G. A. Magel, D. H. Jundt, R. L. Byer, IEEE J. Quantum Electron. 28 (1992) 2631-2654.

[31] Z. Ye, Q. Lou, J. Dong, Y. Wei, L. Lin, Opt. Lett. 30 (2005) 73-74.

[32] M. Fujimura, T. Kodama, T. Suhara, H. Nishihara, IEEE Photonics Technol. Lett. 12 (2000) 1513-1515.

[33] C. Becker, T. Oesselke, J. Pandavenes, R. Ricken, K. Rochhausen, G. Schreiber, W. Sohler, H. Suche, R. Wessel, S. Balsamo, I. Montrosset, D. Sciancalepore, IEEE J. Quantum Electron. 33 (1997) 101-113.

[34] J. Webjorn, S. Siala, D. W. Nam, R. G. Waarts, R. J. Lang, IEEE J. Quantum Electron. 33 (1997) 1673-1686.

[35] G. D. Boyd, D. A. Kleinmann, J. Appl. Phys. 39 (1968) 3597-3639.

[36] K. R. Parameswaran, R. K. Kurz, J. R. Kurz, R. V. Roussev, M. M. Fejer, M. Fujimura, Opt. Lett. 27 (2002) 179-181.

[37] J. S. Levy, A. Gondarenko, M. A. Foster, A. C. Turner-Foster, A. L. Gaeta, M. Lipson, Nature Photon. 4 (2009) 37-40.

[38] L. Razzari, D. Duchesne, M. Ferrera, R. Morandotti, S. Chu, B. E. Little, D. J. Moss, Nature Photon. 4 (2009) 41-45.

[39] R. H. Stolen, J. E. Bjorkholm, IEEE J. Quantum Electron. 18 (1982) 1062-1072.

[40] M. Peccianti, A. Pasquazi, Y. Park, B. E. Little, S. T. Chu, D. J.Moss, R. Morandotti, CLEO/QELS, May 2010, San Jose, California, Conference Digest, paper CPDA9

[41] O. Boyraz, B. Jalali, Opt. Express 12 (2004) 5269-5273.

[42] H. Rong, S. Hu, Y. H. Kao, V. Sih, O. Cohen, O. Raday, M. Paniccia, Nature Photon. 1 (2007) 232-237.

[43] H. Rong, S. Hu, O. Cohen, O. Raday, M. Lee, V. Sih, M. Paniccia, Nature Photon. 2 (2008) 170-174.

[44] H. Byun, D. Pudo, S. Frolov, A. Hanjani, J. Shmulovich, E. P. Ippen, F. X. Kärtner, IEEE Photonics Technol. Lett. 21 (2009) 763-765.

[45] T. W. Baehr-Jones, M. J. Hochberg, J. Phys. Chem. C 112 (2008) 8085-8090.

[46] B. K. Das, R. Ricken, V. Quiring, H. Suche, W. Sohler, Opt. Lett 29 (2004) 165-167.

[47] P. K. Tien, Appl. Opt. 10 (1971) 2395-2413.

[48] R. Claps, V. Raghunathan, D. Dimitropoulos, B. Jalali, Opt. Express 12 (2004) 2774-2780.

[49] R. A. Soref, B. R. Benett, IEEE. J. Quantum Electron. 23 (1987) 123-129.

[50] R. G. Hunsperger, "*Integrated Optics—Theory and Technology*" (Springer, 2002).

[51] E. A. Marcatili, Bell Syst. Tech. J. 48 (1969) 2103-2132.

[52] F. Zernike, J. W. Douglas, D. R. Olson, J. Opt. Soc. Am. 61 (1971) 678.

[53] H. P. Weber, F. A. Dunn, W. N. Leibolt, Appl. Opt. 12 (1973) 755-757.

[54] G. Tittelbach, B. Richter, W. Karthe, Pure Appl. Opt. 2 (1993) 683-706.

[55] C. Florea, K. A. Winick, J. Lightwave Technol. 21 (2003) 246-253.

[56] R. Regener, W. Sohler, Appl. Phys. B 36 (1985) 143-147.

[57] S. Brulisauer, D. Fluck, C. Solcia, T. Pliska, P. Günter, Opt. Lett. 20 (1995) 1773-1775.

[58] C. Grivas, D. P. Shepherd, T. C. May-Smith, R. W. Eason, M. Pollnau, A. Crunteanu, M. Jelínek, IEEE J. Quantum Electron. 39 (2003) 501-507.

[59] N. Nourshargh, E. M. Starr, N. I. Fox, S. G. Jones, Electron. Lett. 21 (1985) 818-820.

[60] Y. Okamura, S. Yoshinaka, S. Yamamoto, Appl. Opt. 22 (1983) 3892-3894.

[61] M. Weisser, F. Thoma, B. Menges, U. Langbein, S. Mittler-Neher, Opt. Commun. 153 (1998) 27–31.

[62] A. Kahn,Y. Kuzminykh, H. Scheife, G. Huber, J. Opt. Soc. Am. B 24 (2007) 1571-1574.

[63] D. Findlay, R. A. Clay, Phys. Lett. 20 (1966) 277-278.

[64] B. Ferrand, B. Chambaz, M. Couchaud, Opt. Mater. 11 (1999) 101-114.

[65] M. Pollnau, Y. E. Romanyuk, F. Gardillou, C. N. Borca, U. Griebner, S. Rivier, V. Petrov IEEE J. Sel. Top. Quantum Electron. 13 (2007) 661-671.

[66] I. Chartier, B. Ferrand, D. Pelenc, S. J. Field, D. C. Hanna, A. C. Large, D. P. Shepherd, A. C. Tropper, Opt. Lett. 17 (1992) 810-812.

[67] W. Bolaňos, J. J. Carvajal, M. C. Pujol, X. Mateos, G. Lifante, M. Aguiló, F. Díaz, Cryst. Growth Des. 9 (2009) 3525-3531.

[68] J. P. van der Ziel, W.A. Bonner, L. Kopf, S. Singh, L. G. van Uitert, Appl. Phys. Lett. 22 (1973) 656-657.

[69] D. C. Hanna, A. C. Large, D. P. Shepherd, A. C. Tropper, I. Chartier, B. Ferrand, D. Pelenc, Opt. Commun. 91 (1992) 229-235.

[70] D. C. Hanna, A. C. Large, D. P. Shepherd, and A. C. Tropper, I. Chartier, B. Ferrand, D. Pelenc, Appl. Phys. Lett. 63 (1993) 7-9.

[71] D. Pelenc, B. Chambaz, I. Chartier, B. Ferrand, C. Wyon, D. P. Shepherd, D. C. Hanna, A. C. Large, A. C. Tropper, Opt. Commun. 115 (1995) 491-497.

[72] A. Rameix, C. Borel, B. Chambaz, B. Ferrand, D. P. Shepherd, T. J. Warburton, D. C. Hanna, A. C. Tropper, Opt. Commun. 142 (1997) 239-243.

[73] D. P. Shepherd, D. Hanna, A. C. Large, A. C. Tropper, T. J. Warburton, C. Borel, B. Ferrand, D. Pelnec, A. Rameix, P. Thony, F. Auzel, D. Meichenin, J. Appl. Phys. 76 (1994) 7651-7653.

[74] M. Shimokozono, N. Sugimoto, A. Tate, Y. Katoh, M. Tanno, S. Fukuda, T. Ryuoh, Appl. Phys. Lett. 68 (1996) 2177-2179.

[75] R. Gerhardt, J. Kleine-Borger, L. Beilschmidt, M. Frommeyer, H. Dotsch, B. Gather, Appl. Phys. Lett. 75 (1999) 1210-1212.

[76] A. Aznar, R. Solé, M. Aguiló, F. Díaz, U. Griebner, R. Grunwald, V. Petrov, Appl. Phys. Lett. 85 (2004) 4313-4315.

[77] Y. E. Romanyuk, C. N. Borca, M. Pollnau, S. Rivier, V. Petrov, U. Griebner, Opt. Lett. 31 (2006) 53-55.

[78] F. Bain, A. Lagatsky, S. Kurilchick, V. Kisel, S. Guretsky, A. Luginets, N.A. Kalanda, I. M. Kolesova, N. V. Kuleshov, W. Sibbett, C. T. A. Brown, Opt. Express 17 (2009) 1666-1670.

[79] S. Rivier, U. X. Mateos, V. Petrov, U. Griebner, Y. E. Romanyuk, C. N. Borca, F. Gardillou, M. Pollnau, Opt. Express 15 (2007) 5885-5892.

[80] O. Silvestre, M. C. Pujol, M. Aguiló, F. Díaz, X. Mateos, V. Petrov, U. Griebner, IEEE J. Quantum Electron. 43 (2007) 257-260.

[81] D. Geskus, S. Aravazhi, E. Bernhardi, C. Grivas, Harkema, K. Wörhoff, M. Pollnau, Laser Phys. Lett. 6 (2009) 800-805.

[82] D. Geskus, S. Aravazhi, C. Grivas, K. Wörhoff, M. Pollnau, Opt. Express 18 (2010) 8853-8858.

[83] D. Geskus, S. Aravazhi, K. Wörhoff, M. Pollnau, Opt. Express 18 (2010) 26107-26112.

[84] W. Bolaños, J. J. Carvajal, X. Mateos, M. Aguiló, F. Díaz, G. S. Murugan, A. Subramanian, J. S. Wilkinson, E. Cantelar, G. Lifante, Opt. Express 18 (2010) 26937-26945.

[85] W. Bolaños, J. J. Carvajal, X. Mateos, E. Cantelar, G. Lifante, U. Griebner, V. Petrov, V. L. Panyutin, G. S. Murugan, J. S. Wilkinson, M. Aguiló, F. Díaz, Opt. Express 18 (2011) 1449-1454.

[86] P. Rogin, J. Hulliger, Opt. Lett. 22 (1997) 1701-1703.

[87] R. W. Eason, S. J. Barrington, C. Grivas, T. C. May-Smith, D. P. Shepherd, *"Optical waveguide growth and applications"* in "*Pulsed Laser Deposition of thin films: applications-lead growth of functional materials*" (Wiley 2006) .

[88] M. Jelínek, J. Lančok, J. Sonsky, J. Oswald, Simeckova, L. Jastrabik, V. Studnicka, C. Grivas, P. Hribek, Czech. J. Phys. 48 (1998) 577-597.

[89] N.A. Vainos, C. Grivas, C. Fotakis, R.W. Eason, A.A. Anderson, D.S. Gill, D.P. Shepherd, M. Jelinek, J. Lancok, J. Sonsky, Appl. Surf. Sci. 127 (1998) 514-519.

[90] A. V. Rode, A. Zakery, M. Samoc, R. B. Charters, E. G. Gamaly, B. Luther-Davies, Appl. Surf. Sci. 197-198 (2002) 481-485.

[91] E. Millon, J. Perriere, R.M. Defourneau, D. Defourneau, O. Albert, J. Etchepare, Appl. Phys. A 77 (2003) 73-80.

[92] M. Jelinek, A. Klini, C. Grivas, L. Lancok, V. Studnicka, J. Chval, A. Mackova, C. Fotakis, Appl. Surf. Sci. 197 (2002) 416-420.

[93] R. W. Eason, T. C. May-Smith, C. Grivas, M. S. B. Darby, D. P. Shepherd, R. Gazia, Appl. Surf. Sci. 255 (2009) 5199-5205.

[94] J. Sonsky, M. Jelinek, P. Hribek, P. J. Oswald, L. Jastrabic, V. Studnicka, C. Fotakis, C. Grivas, Laser Phys. 8 (1998) 285-290.

[95] J. Lancok, M. Jelinek, C. Grivas, F. Flory, E. Lebrasseur, C. Garapon, Thin Solid Films 346 (1999) 284-289.

[96] P. A. Atanasov, R. I. Tomov, J. Perriére, R.W. Eason, N. Vainos, A. Klini, A. Zherikhin, E. Millon, Appl. Phys. Lett. 76 (2000) 2490-2492.

[97] D. S. Gill, A. A. Anderson, R. W. Eason, T. J. Warburton, D. P. Shepherd, Appl. Phys. Lett. 69 (1996) 10-12.

[98] A. A. Anderson, C. L. Bonner, D. P. Shepherd, R. W. Eason, C. Grivas, D. S. Gill, N. A. Vainos, Opt. Commun. 144 (1997) 183-186.

[99] C. L. Bonner, A. A. Anderson, R. W. Eason, D. P. Shepherd, D. S. Gill, C. Grivas, N. A.Vainos, Opt. Lett. 22 (1997) 988-990.

[100] C. Grivas, T. C. May-Smith, D. P. Shepherd, R. W. Eason, Appl. Phys. A 79 (2004) 1203-1206.

[101] T. C. May-Smith, C. Grivas, D. P. Shepherd, R. W. Eason, M. J. F. Healy, Appl. Surf. Sci. 223 (2004) 361-371.

[102] C. Grivas, T. C. May-Smith, D. P. Shepherd, R. W. Eason, Opt. Commun. 229 (2004) 355-361.

[103] A. Kahn, S. Heinrich, H. Kühn, K. Petermann, J. D. B. Bradley, K. Wörhoff, M. Pollnau, G. Huber, Opt. Express 17 (2009) 4412-4418.

[104] H. Kühn, S. Heinrich, A. Kahn, K. Petermann, J. D. B. Bradley, K. Wörhoff, M. Pollnau, G. Huber, Opt. Lett. 34 (2009) 2718-2720.

[105] C. Grivas, W. Eason, J. Phys.: Condens. Matter 20 (2008) 264011.

[106] J. E. Williams, V. V. Fedorov, D. V. Martyshkin, I. S. Moskalev, R. P. Camata, S. B. Mirov, Opt. Express 18 (2010) 25999-26006

[107] S. Mailis, A. A. Anderson, S. J. Barrington, W. S. Brocklesby, R. Greef, H. N. Rutt, R. W. Eason, N. A. Vainos, C. Grivas, Opt. Lett. 23 (1998) 1751-1753.

[108] S. Mailis, C. Riziotis, J. Wang, E. Taylor, A. A. Anderson, S. J. Barrington, H. V. Rutt, R. W. Eason, N. A. Vainos, C. Grivas, Opt. Mater. 12 (1998) 27-33.

[109] S. Mailis, L. Reekie, S. Pissadakis, S. J. Barrington, R. W. Eason, N. A. Vainos, C. Grivas, Appl. Phys. A 69 (1999) S671-S674.

[110] R. J. Curry, A. K. Mairaj, C. C. Huang, R. W. Eason, C. Grivas, D. W. Hewak, J. V. Badding, J. Am. Ceram. Soc. 88 (2005) 2451-2455.

[111] R. Serna, M. Jiménez de Castro, J. A. Chaos, C. N. Afonso, I. Vickridge, Appl. Phys. Lett. 75 (1999) 4073-4075.

[112] R. Serna, M. Jiménez de Castro, J. A. Chaos, A. Suárez-Garcia, C. N. Afonso, M. Fernández, I. Vickridge, J. Appl. Phys. 90, 5120 (2001)

[113] A. Suarez-Garcia, R. Serna, M. Jiménez de Castro, C. N. Afonso, I. Vickridge Appl. Phys. Lett. 84 (2004) 2151-2153.

[114] L.-C. Chen, *"Particulates generated by pulsed laser ablation"* in "*Pulsed Laser Deposition of thin films*", D. B. Chrisey, G. K. Hubler (Eds.), (Wiley 1994).

[115] T. Yoshitake, G. Shiraishi, K. Nagayama, Appl. Surf. Sci. 197–198 (2002) 379–383.

[116] R. Peters, C. Kränkel, K. Petermann, G. Huber, J. Cryst. Growth 310 (2008) 1934-1938.

[117] A. A. Anderson, M. Jelínek, C. Grivas, L. M. B. Hickey, K. Rogers, D. Lane, Thin Solid Films 300 (1997) 68-71.

[118] T. Gün, A. Kahn, B. İleri, K. Petermann, G. Huber, Appl. Phys. Lett. 93 (2008) 053108.

[119] R. Burkhalter, I. Dohnke, J. Hulliger, Prog. Crystal Growth and Charact. 42 (2001) 1-64.

[120] R. A. Betts, C. W. Pitt, Electron. Lett. 21 (1985) 960-962.

[121] R. A. McKee, F. J. Walker, J. R. Conner, E. D. Specht, D. E. Zelmon, Appl. Phys. Lett. 59 (1991) 782-784.

[122] R. A. McFarlane. M. Lui, D. Yap, IEEE J. Sel. Top. Quantum Electron. 1 (1995) 82-91.

[123] L. E. Bausá, R. Legros, A. Muñioz-Yagüe, Appl. Phys. Lett. 59 (1991) 152-154.

[124] E. Daran, R. Legros, A. Muñoz-Yagüe, C. Fontaine, L. E. Bausá, J. Appl. Phys.76 (1994) 270-273.

[125] X. Zhang, F. Lahoz, C. Serrano, G. Lacoste, E. Daran, IEEE J. Quantum Electron. 36 (2000) 243-247.

[126] E. Daran, D. P. Shepherd, T. Bhutta, C. Serrano, Electron. Lett. 35 (1999) 398-400.

[127] T. Bhutta, A. M. Chardon, D. P. Shepherd, E. Daran, C. Serrano, A. Muñoz-Yagüe, IEEE J. Quantum Electron. 37 (2001) 1469-1477.

[128] M. R. Poulsen, P. I. Borel, J. Fage-Pedersen, J. Hübner, M. Kristensen, J. H. Povlsen, K. Rottwitt, M. Svalgaard, W. Svendsen, Opt. Eng. 42 (2003) 2821-2834.

[129] J. Hübner, S. Guldberg-Kjaer, M. Dyngaard, Y. Shen, C. L. Thomsen, S. Balslev, C. Jensen, D. Zauner, T. Feuchter, Appl. Phys. B 73 (2001) 435-438.

[130] S. Guldberg-Kjaer, J. Hübner, M. Kristensen, C. Laurent-Lund, M. Rysholt Poulsen, M. W. Sckerl, Electron. Lett. 32 (1999) 302-303.

[131] C. E. Chryssou, C. W. Pitt, IEEE J. Quantum Electron. 34 (1998) 282-285.

[132] R. Claps, V. Raghunathan, O. Boyraz, P. Koonath, D. Dimitropoulos, B. Jalali, Opt. Express 13 (2005) 2459-2466.

[133] C. E. Chryssou, C. W. Pitt, Appl. Phys. A 65 (1997) 469-475.

[134] H. Y. Ou, Electron. Lett. 39 (2003) 212-213.

[135] M. Kawachi, Opt. Quantum Electron. 22 (1990) 391-416.

[136] M. Kawachi, M. Yasu, T. Edahiro, Electron. Lett. 19 (1983) 583-584.

[137] J. R. Bautista, E. Potkay, D. L. Scatton, Electron. Lett. 23 (1987) 330-331.

[138] R. Tumminelli, E. Hakimi, J. Haavisto, Opt. Lett. 16 (1991) 1098-1100.

[139] J. A. Bebbington, G. Barbarossa, J. R. Bonar, J. S. Aitchison, Appl. Phys. Lett. 62 (1993) 337-339.

[140] J. R. Bonar, J. A. Bebbington, J. S. Aitchison, G. D. Maxwell, B. J. Ainslie, Electron. Lett. 31 (1994) 99-100.

[141] J. E. Townsend, S. B. Poole, D. N. Payne, Electron. Lett. 23 (1987) 330-331.

[142] J. R. Bonar, J. A. Bebbington, J. S. Aitchison, G. D. Maxwell, B. J. Ainslie, Electron. Lett. 30 (1994) 229-230.

[143] K. Hattori, T. Kitagawa, Y. Ohmori, M. Kobayashi, IEEE Photon. Technol. Lett. 3 (1991) 882-884.

[144] D. A. Guilhot, G. D. Emmerson, C. B. E. Gawith, S. P. Watts, D. P. Shepherd, R. B. Williams, P. G. R. Smith, Opt. Lett. 29 (2004) 947-949.

[145] Y. Hibino, T. Kitakawa, M. Shimizu, F. Hanawa, A. Sugita, IEEE Photon. Technol. Lett. 1 (1989) 349-350.

[146] J. Bonar, J. S. Aitchison, IEE Proc.-Optoelectron. 143 (1996) 293-297.

[147] T. Kitagawa, F. Bilodeau, B. Malo, S. Theriault, J. Albert, D. C. Jihnson, K. O. Hill, K. Hattori, Y. Hibino, Electron. Lett. 30 (1994) 1311-1312.

[148] K. Hattori, T. Kitagawa, Y. Ohmori, J. Appl. Phys. 79 (1996) 1238-1243.

[149] H. Dislich, Angew. Chem. Int. Ed. 10 (1971) 363-370.

[150] A. Selvarajan, T. Srinivas, IEEE J. Quant. Electron. 37 (2001) 1117-1126.

[151] S. Bhandarkar, J. Am. Ceram. Soc. 87 (2004) 1180-1199.

[152] M. Benatsou, B. Capoen, M. Bouazaoui, W. Tchana, J. P. Vilcot, Appl. Phys. Lett. 71 (1997) 428-430.

[153] X. Orignac, D. Barbier, X. M. Du, R. M. Almeida, O. McCarthy, E. Yeatman, Opt. Mater. 12 (1999) 1-18.

[154] Y. Sorek, M. Zevin, R. Reisfeld, T. Hurvits, S. Ruschin, Chem. Mater. 9 (1997) 670-676.

[155] C. Strohhöfer, S. Capecchi, J. Fick, A. Martucci, G. Brusatin, M. Guglielmi, Thin Solid Films 326 (1998) 99-105.

[156] X. Orignac, D. Barbier, X. M. Du, R. M. Almeida, Appl. Phys. Lett. 69 (1996) 895-897.

[157] Y. Sorek, R. Reisfeld, I. Finkelstein, S. Ruschin, Appl. Phys. Lett. 66 (1995) 1169-1171.

[158] G. C. Righini, S. Pelli, J. Sol-Gel Sci. Technol. 8 (1997) 991-997.

[159] I. Finkelstein, S. Ruschin, Y. Sorek, R. Reisfeld, Opt. Mater. 7 (1997) 9-13.

[160] X-L. Zhu, D. Lo, Appl. Phys. Lett. 77 (2000) 2747-2749.

[161] D. Lo, L. Shi, J. Wang, G.-X. Zhang X.-L. Zhu, Appl. Phys. Lett. 81 (2002) 2707-2709.

[162] C. Ye, K.Y. Wong Y. He, X. Wang, Opt. Express 15 (2007) 936-944.

[163] F. Chen, J. Wang, C. Ye, D. Lo, X. Zhu, Appl. Phys. Lett. 85 (2004) 4284-4286.

[164] J. Wang, G. Zhang, L. Shi, D. Lo, X. Zhu, Opt. Lett. 28 (2003) 90-92.

[165] C. Ye, J. Wang, D. Lo, Appl. Phys. B 78 (2004) 539-541.

[166] C. Ye, J. Wang, L. Shi, D. Lo, Appl. Phys. B 78 (2004) 189-194.

[167] L. Shi, G. Zhang, J. Wang, D. Lo, J. Opt. A: Pure Appl. Opt. 5 (2003) L1-L4.

[168] X. Zhu, D. Lo, Appl. Phys. Lett. 80 (2002) 917-919.

[169] A. Peled, A. Chiasera, M. Nathan, M. Ferrari, S. Ruschin, Appl. Phys. Lett. 92 (2008) 221104.

[170] M. Guglielmi, G. Brusatin, G. Della Giustina, J. Non-Cryst. Solids 353 (2007) 1681-1687.

[171] Y. Sorek, R. Reisfeld, I. Finkelstein, S. Ruschin, Appl. Phys. Lett. 63 (1993) 3256-3258.

[172] X. M. Du, T. Touam, L. Degachi, J. L. Guilbault, M. P. Andrews, S. I. Najafi, Opt. Eng. 37 (1998) 1101-1104.

[173] F. Chen, J. Wang, C. Ye, W. Ni, J. Chan, Y. Yang, D. Lo, Opt. Express 13 (2005) 1643-1650.

[174] C. Ye, L. Shi, J. Wang, D. Lo, X. Zhu, Appl. Phys. Lett. 83 (2003) 4101-4103.

[175] C. Sanchez, L. Rozes, F. Ribot, C. Laberty-Robert, D. Grosso, C. Sassoye, C. Boissiere, L. Nicole, C. R. Chimie 13 (2010) 3-39.

[176] G. J. de A. A. Soler-Illia, C. Sanchez, B. Lebeau, J. Patarin, Chem. Rev. 102 (2002) 4093-4138.

[177] G. J. de A.A. Soler-Illia, E. L. Crepaldi, D. Grosso, C. Sanchez, Curr. Opin. Coll. Interface Sci. 8 (2003) 109-126.

[178] P. Yang, G. Wirnsberger, H. C. Huang, S. R. Cordero, M. D. McGehee, B. Scott, T. Deng, G. M. Whitesides, B. F. Chmelka, S. K. Buratto, G. D. Stucky, Science 287 (2000) 465-467.

[179] G. Wirnsberger, P. Yang, H. C. Huang, B. Scott, T. Deng, G. M. Whitesides, B. F. Chmelka, G. D. Stucky, J. Phys. Chem. B 105 (2001) 6307-6313.

[180] B. J. Scott, G. Wirnsberger, M. D. McGehee, B. F. Chmelka, G. D. Stucky, Adv. Mater. 13 (2001) 1231-1234.

[181] M. Berggren, A. Dodabalapur, R. E. Slusher, Z. Bao, Nature 389 (1997) 466-469.

[182] V. G. Kozlov, V. Bulovič, P. E. Burrows, M. Baldo, V. B. Khalfin, G. Parthasarathy, S. R. Forrest, Y. You, M. E. Thompson, J. Appl. Phys. 84 (1998) 4096-4108.

[183] V. G. Kozlov, V. Bulovič, P. E. Burrows, S. R. Forrest, Nature 389 (1997) 362-264.

[184] A. Dodabalapur, M. Berggren, R. E. Slusher, Z. Bao, A. Timko, P. Schiortino, E. Laskowski, H. E. Katz, O. Nalamasu, IEEE J. Sel. Top. Quantum Electron. 4 (1998) 67-74.

[185] M. Berggren, A. Dodabalapur, R. E. Slusher, Appl. Phys. Lett. 71 (1997) 2230-2232.

[186] K. Wörhoff, J. D. B. Bradley, F. Ay, D. Geskus, T. P. Blauwendraat, M. Pollnau, IEEE J. Quantum Electron. 45 (2009) 454-461.

[187] G. N. van den Hoven, R. J. I. M. Koper, A. Polman, C. van Dam, J. W. M. van Uffelen, M. K. Smit, Appl. Phys. Lett. 68 (1996) 1886-1888.

[188] J. D. B. Bradley, L. Agazzi, D. Geskus, F. Ay, K. Wörhoff, M. Pollnau, J. Opt. Soc. Am. B 27 (2010) 187-196.

[189] J. D. B. Bradley, M. Costa e Silva, M. Gay, L. Bramerie, A. Driessen, K. Wörhoff, J.-C. Simon, M. Pollnau, Opt. Express 17 (2009) 22201-22208.

[190] B. Unal, M. C. Netti, M. A. Hassan, P. J. Ayliffe, M. D. B. Charlton, F. Lahoz, N. M. B. Perney, D. P. Shepherd, C. Y. Tai, J. S. Wilkinson, G. J. Parker, IEEE J. Quantum Electron. 41 (2005) 1565-1573.

[191] B. Unal, C. Y. Tai, D. P. Shepherd, J. S. Wilkinson, N. M. B. Perney, M. C. Netti, G. J. Parker, Appl. Phys. Lett. 86 (2005) 021110.

[192] A. Z. Subramanian, C. J. Oton, D. P. Shepherd, J. S. Wilkinson, IEEE Photon. Technol. Lett. 22 (2010) 1571-1573.

[193] E. H. Bernhardi, H. A. G. M. van Wolferen, K. Wörhoff, R. M. de Ridder, M. Pollnau, Opt. Lett. 36 (2011) 603-605.

[194] J. D. B. Bradley, R. Stoffer, L. Agazzi, F. Ay, K. Wörhoff, M. Pollnau, Opt. Lett 35 (2010) 73-75.

[195] E. H. Bernhardi, H. A. G. M. van Wolferen, L. Agazzi, M. R. H. Khan, C. G. H. Roeloffzen, K. Wörhoff, M. Pollnau, R. M. de Ridder, Opt. Lett. 35 (2010) 2394-2396.

[196] G. R. J. Robertson, P. E. Jessop, Appl. Opt. 30 (1991) 276-278.

[197] J. Haisma, N. Hattu, J. T. C. M. (Dook) Pulles, E. Steding, J. C. G. Vervest, Appl. Opt. 46 (2007) 6793-6803.

[198] G. A. C. M. Spierings, J. Haisma T. M. Michielsen, Philips J. Res. 49 (1995) 47-63.

[199] C. T. A. Brown, C. L. Bonner, T. J. Warburton, D. P. Shepherd, A. C. Tropper, D. C. Hanna, H. E. Meissner, Appl. Phys. Lett. 71 (1997) 1139-1141.

[200] C. L. Bonner, C. T. A. Brown, D. P. Shepherd, W. A. Clarkson, A. C. Tropper, D. C. Hanna, B. Ferrand, Opt. Lett. 23 (1998) 942-944.

[201] U. Griebner, R. Grunwald, H. Schonnagel, Opt. Commun. 164 (1999) 185-190.

[202] D. P. Shepherd, C. L. Bonner, C. T. A. Brown, W. A. Clarkson, A. C. Tropper, D. C. Hanna, H. E. Meissner, Opt. Commun. 160 (1999) 47-50.

[203] H. J. Baker, A. A. Chesworth, D. Pelaez Millas, D. R. Hall, Opt. Commun. 191 (2001) 125-131.

[204] R. J. Beach, S. C. Mitchell, H. E. Meissner, O. R. Meissner, W. F. Krupke, J. M. McMahon, W. J. Bennet, D. P. Shepherd, Opt. Lett. 26 (2001) 881-883.

[205] J. I. Mackenzie, C. Li, D. P. Shepherd, H. E. Meissner, S. C. Mitchell, Opt. Lett. 26 (2001) 698-700.

[206] J. I. Mackenzie, C. Li, D. P. Shepherd, R. J. Beach, H. E. Meissner, S. C. Mitchell, Electron. Lett. 37 (2001) 898-899.

[207] J. I. Mackenzie, D. P. Shepherd, Opt. Lett. 27 (2002) 2161-2163.

[208] J. I. Mackenzie, C. Li, D. P. Shepherd, IEEE J. Quantum Electron. 39 (2003) 493-500.

[209] C. Li, J. I. Mackenzie, J. Wang, D. P. Shepherd, Opt. Commun. 226 (2003) 317-321.

[210] J. Xu, Opt. Commun. 259 (2006) 251-255.

[211] J. Xu, I. J. Thomson, J. D. R. Valera, H. J. Baker, A. B. Russell, D. R. Hall, IEEE J. Sel. Quantum Electron. 13 (2007) 638-646.

[212] L. Xiao, X. Cheng, J. Xu, Opt. Commun. 281 (2008) 3781-3785.

[213] H.X. Kang, H. Zhang, P. Yan, D.S. Wang, M. Gong, Laser Phys. Lett. 5 (2008) 879-881.

[214] M. Gong, H. Zhang, H. X. Kang, D. S. Wang, L. Huang, P. Yan, Q. Liu, Laser Phys. Lett. 5 (2008) 518-521.

[215] J. I. Mackenzie, Appl. Phys. B 97 (2009) 297-306.

[216] C. B. E. Gawith, T. Bhutta, D. P. Shepherd, P. Hua, J. Wang, G. W. Ross, P. G. R. Smith, Appl. Phys. Lett. 75 (2004) 3747-3749.

[217] U. Griebner, H. Schönnagel, Opt. Lett. 24 (1999) 750-752.

[218] U. Griebner, R. Grunwald, H. Schönnagel, J. Huschke G. Erbert, Appl. Phys. Lett. 77 (2000) 3505-3507.

[219] L. H. Slooff, A. van Blaaderen, A. Polman, G. A. Hebbink, S. I. Klink, F. C. J. M. Van Veggel, D. N. Reinhoudt, J. W. Hofstraat, J. Appl. Phys. 91 (2002) 3955-3980.

[220] J. Yang, M. B. J. Diemeer, C. Grivas, G. Sengo, A. Driessen, M. Pollnau, Laser Phys. Lett. 7 (2010) 650-656.

[221] I. D. W. Samuel, G. A. Turnbull, Chem. Rev. 107 (2007) 1272-1295.

[222] L. Eldada, L. W. Shacklette, IEEE J. Quantum Electron. 6 (2000) 54-68.

[223] A. Costela, I. García-Moreno, R. Sastre, Phys. Chem. Chem. Phys. 5 (2003) 4745-4763.

[224] M. B. Christiansen, M. Schøler, A. Kristensen, Opt. Express 15 (2007) 3931-3939.

[225] C. Grivas, J. Yang, M. B. J. Diemeer, A. Driessen, M. Pollnau, Opt. Lett. 35 (2010) 1983-1985.

[226] R.V. Schmidt, I. P. Kaminov, Appl. Phys. Lett. 25 (1974) 458-460.

[227] J. Crank, *Mathematics of diffusion* (Oxford University press, 2003).

[228] I. Baumann, S. Bosso, R. Brinkmann, R. Corsini, M. Dinand, A. Greiner, K. Schäfer, J. Söchtig, W. Sohler, H. Suche, R. Wessel, IEEE J. Sel. Top. Quantum Electron. 2 (1996) 355-366.

[229] L. M. B. Hickey, E. Martins, J. E. Román, W. S. Brocklesby, J. S. Wilkinson, Opt. Lett. 21 (1996) 597-599.

[230] H. Hu, R. Ricken, W. Sohler, Appl. Phys. B 98 (2010) 677-679.

[231] W. Sohler, B. K. Das, D. Dey, S. Reza, H. Suche, R. Ricken, IEICE Trans. Electron. E88C (2005) 990-997.

[232] W. Sohler, H. Hu, R. Ricken, V. Quiring, C. Vannahme, H. Herrmann, D. Büchter, S. Reza, W. Grundkötter, S. Orlov, H. Suche, R. Nouroozi, Y. Min, Optics & Photonics News 19 (2008) 24-31.

[233] M. Hempstead, J. S. Wilkinson, L. Reekie, IEEE Photon.Technol. Lett. 4 (1992) 852-855.

[234] J. K. Jones, J. P. Desandro, M. Hempstead, D. P. Shepherd, A. C. Large, A. C. Tropper, J. S. Wilkinson, Opt. Lett. 20 (1995) 1477-1479.

[235] J. Amin, J. A. Aust, N. A. Sanford, Appl. Phys. Lett. 69 (1996) 3785-3787.

[236] J. Amin, M. Hempstead, J. E. Román, J. S. Wilkinson Opt. Lett. 19 (1994) 1541-1543.

[237] C. T. A. Brown, J. Amin, D. P. Shepherd, A. C. Tropper, M. Hempstead, J. M. Almeida, Opt. Lett. 22 (1997) 1778-1780.

[238] M. Fujimura, H. Tsugawa, M. S. Khan, H. Nishihara, M. Haruna, Electron. Lett. 34 (1998) 1319-1321.

[239] J. P. de Sandro, J. K. Jones, D. P. Shepherd, M. Hempstead, J. Wang, A. C. Tropper, IEEE Photon. Technol. Lett. 8 (1996) 209-211.

[240] R. E. Di Paolo, E. Cantelar, P. L. Pernas, G. Lifante, F. Cusso Appl. Phys. Lett. 79 (2001) 4088-4090.

[241] M. Domenech, G. Lifante, Appl. Phys. Lett. 84 (2004) 3271-3273.

[242] E. Cantelar, J.A. Sanz-Garcia, G. Lifante, F. Cusso, Appl. Phys. Lett. 86 (2005) 161119.

[243] N. A. Sanford, J. A. Aust, K. J. Malone, D. R. Larson, A. Roshko, Opt. Lett. 17 (1992) 1578-1580.

[244] L. M. B. Hickey, V. Apostolopoulos, R. W. Eason, J. S. Wilkinson, A. A. Anderson, J. Opt. Soc. Am. B 21 (2004) 1452-1462.

[245] T. Izawa, H. Nakagome, Appl. Phys. Lett. 21 (1971) 584-586.

[246] G. Giallorenzi, E. J. West, R. Kirk, R. Ginther, R. A. Andrews, Appl. Opt. 12 (1973) 1240-1244.

[247] R. V. Ramaswamy, I. Srivastava, J. Lightwave Technol. 6 (1988) 984-1002.

[248] G. Jose, G. Sorbello, S. Taccheo, G. Della Valle, E. Cianci, V. Foglietti, P. Laporta, Opt. Mater. 23 (2003) 559-567.

[249] A. Opilski, R. Rogozinski, M. Blahut, P. Karasinski, K. Gut, Z. Opilski, Opt. Eng. 36 (1997) 1625-1638.

[250] M. N. Weiss, R. Srivastava, Appl. Opt. 34 (1995) 455-458.

[251] R. V. Ramaswamy, I. Najafi, IEEE J. Quantum Electron. 22 (1986) 883-891.

[252] P. C. Noutsios, C. L. Yip, Opt. Lett. 15 (1990) 212-214.

[253] G. Della Valle, S. Taccheo, G. Sorbello, E. Cianci, V. Foglietti, P. Laporta, Electron. Lett. 42 (2006) 632-633.

[254] G. Sorbello, S. Taccheo, M. Marano, M. Marangoni, R. Ramponi, R. Osellame N. P. Laporta, Opt. Mater. 17 (2001) 425-435.

[255] G. Della Valle, A. Festa, G. Sorbello, K. Ennser, C. Cassagnetes, D. Barbier, S. Taccheo, Opt. Express 16 (2008) 12334-12334.

[256] S. S. Gevorgyan, Electron. Lett. 26 (1990) 38-39.

[257] G. H. Chartier, P. Jaussaud, A. D. de Oliveira, O. Parriau, Electron. Lett. 14 (1978) 132-134.

[258] H.-J. Lilienhof, E. Voges, D. Ritter, B. Pantschew, IEEE J. Quantum Electron. 18 (1982) 1877-1883.

[259] G. Sorbello, S. Taccheo, P. Laporta, O. Svelto, E. Cianci, V. Foglietti, S. Jiang, N. Peyghambarian, Electron. Lett. 37 (2001) 1014-1015.

[260] D. L. Veasey, D. S. Funk, P. M. Peters, N. A. Sanford, G. E. Obarski, N. Fontaine, M. Young, A. P. Peskin, W.-C. Liu, S. N. Houde-Walter, J. S. Hayden, J. Non-Crystalline Solids, 263/264 (2000) 369-381.

[261] P. Madasamy, G. Nunzi Conti, P. Poyhonen, Y. Hu, M. M. Morrell, D. F. Geraghty, S. Honkanen, N. Peyghambarian, Opt. Eng. 41 (2002) 1084-1086.

[262] K. J. Malone, N. A. Sanford, J. S. Hayden, Electron. Lett 29 (1993) 691-692.

[263] A. Yeniay, J.-M. P. Delavaux, J. Toulouse, D. Barbier, T. A. Strasser, J. R. Pedrazanni, IEEE Photon. Technol. Lett. 9 (1997) 1099-1101.

[264] A. Yeniay, J.-M. P. Delavaux, J. Toulouse, D. Barbier, T. A. Strasser, J. R. Pedrazanni, Electron. Lett. 33 (1997) 1792-1794.

[265] E. R. Thoen, E. M. Koontz, D. J. Jones, D. Barbier, F. X. Kartner, E. P. Ippen, L. A. Kolodziejski, IEEE Photon. Technol. Lett. 12 (2000) 149-151.

[266] A. Yeniay, J.-M. Delavaux, J. Toulouse, W. J. Minford, Appl. Opt. 39 (2000) 1430-1434.

[267] J. B. Schlager, B. E. Callicoatt, R. P. Mirin, N. A. Sanford, IEEE Photon. Technol. Lett. 14 (2002) 1351-1353.

[268] J. B. Schlager, B. C. Callicoatt, R. P. Mirin, N. A. Sanford, D. J. Jones, J. Ye, Opt. Lett. 23 (2003) 241-2413.

[269] S. Blaize, L. Bastard, C. Cassagnètes, J. E. Broquin, IEEE Photon. Technol. Lett. 15 (2003) 516-518.

[270] J. A. Aust, K. J. Malone, D. L. Veasey, N. A. Sanford, A. Roshko, Opt. Lett. 19 (1994) 1849-1851.

[271] S. D. Conzone, J. S. Hayden, D. S. Funk, A. Roshko, D. L. Veasey, Opt. Lett. 26 (2001) 509-511.

[272] P. Madasamy, S. Honkanen, D. F. Geraghty, N. Peyghambarian, Appl. Phys. Lett. 82 (2003) 1332-1334.

[273] D. L. Veasey, D. S. Funk, N. A. Sanford, J. S. Hayden, Appl. Phys. Lett. 74 (1999) 789-791.

[274] P. M. Peters, D. S. Funk, A. P. Peskin, D. L. Veasey, N. A. Sanford, S. N. Houde-Walter, J. S. Hayden, Appl. Opt. 38 (1999) 6879-6886.

[275] C. Florea, K. A. Winick, J. Lightwave Technol. 17 (1999) 1593-1601.

[276] J. E. Roman, K. A. Winick, Appl. Phys. Lett. 61 (1992) 2744-2746.

[277] N. A. Sanford, K. J. Malone, D. R. Larson, Opt. Lett. 15 (1990) 366-368.

[278] N. A. Sanford, K. J. Malone, D. R. Larson, Opt. Lett. 16 (1991) 1095-1097.

[279] G. L. Vossler, C. J. Brooks, K. A. Winick, Electron. Lett. 31 (1995) 1162-1163.

[280] J. E. Roman, P. Camy, M. Hempstead, W. S. Brocklesby, S. Nouh, A. Béguin, C. Lerminiaux, J. S. Wilkinson, Electron. Lett. 31 (1995) 1345-1346.

[281] E. K. Mwarania, J. Wang, J. Lane, J. S. Wilkinson, J. Lightwave Technol. 11 (1993) 1550-1558.

[282] S. J. Hettrick, J. Wang, C. Li, J. S. Wilkinson, D. P. Shepherd, J. Lightwave Technol. 22 (2004) 845-849.

[283] E. K. Mwarania, D. M. Murphy, M. Hempstead, L. Reekie, J. S. Wilkinson, Electron. Lett. 4 (1992) 235-237.

[284] S. J. Hettrick, J. I. Mackenzie, R. D. Harris, J. S. Wilkinson, D. P. Shepherd, A. C. Tropper, Opt. Lett. 25 (2000) 1433-1435.

[285] T. Feuchter, E. K. Mwarania, J. Wang, L. Reekie, J. S. Wilkinson, IEEE Photon. Technol. Lett. 4 (1992) 542-544.

[286] C. B. E. Gawith, T. Bhutta, D. P. Shepherd, P. Hua, J. Wang, G. W. Ross, P. G. R. Smith, Appl. Phys. Lett. 75 (1999) 3757-3759.

[287] J. L. Jackel C. E. Rice, J. J. Veselka, Appl. Phys. Lett. 41 (1982) 607-608.

[288] A. Yi-Yan, Appl. Phys. Lett. 43 (1983) 131-133.

[289] Y. N. Korkishko, V. A. Fedorov, M. P. De Micheli, P. Baldi, K. El Hadi, A. Leycuras, Appl. Opt. 35 (1996) 7065-7060.

[290] F. Laurell, M. G. Roelofs, H. Hsiung, Appl. Phys. Lett. 60 (1992) 301-303.

[291] M. L. Bortz, M. M. Fejer, Opt. Lett. 16 (1991) 1844-1846.

[292] M. L. Bortz, L.A. Eyres, M. M. Fejer, Appl. Phys. Lett. 62 (1993) 2012-2014.

[293] P. G. Suchoski, T. K. Findakly, F. J. Leonberger, Opt. Lett. 13 (1988) 1050-1052.

[294] J. L. Jackel, J. J. Johnson, Electron. Lett. 27 (1991) 1360-1361.

[295] Y. N. Korkishko, V. A. Fedorov, T. M. Morozova, F. Caccavale, F. Gonella, F. Segato, J. Opt. Soc. Am. A 15 (1998) 1838-1842.

[296] J. Rams, J. Olivares, J. M. Cabrera, Electron. Lett. 33 (1997) 322-323.

[297] Y. N. Korkishko, V. A. Fedorov, F. Laurell, IEEE J. Sel. Top. Quantum Electron. 6, (2000) 132-142.

[298] P.J. Masalkar, M. Fujimura, T. Suhara, H. Nishihara, Electron. Lett. 33 (1997) 519-520.

[299] J. Rams, J. M. Cabrera, J. Opt. Soc. Am. B 16 (1999) 401-406.

[300] R. Osellame, R. Ramponi, M. Marangoni, V. Russo, Electron. Lett. 36 (2000) 431-432.

[301] S. Nouh, P. Baldi, K. El Hadi, M. De Micheli, G. Monnom, D. B. Ostrowsky, E. Lallier, M. Papuchon, Opt. Lett. 20 (1995) 1468-1470.

[302] P. Baldi, M. P. De Micheli, K. El Hadi, S. Nouh, A. C. Cino, P. Aschieri, D. B. Ostrowsky, Opt. Eng. 37 (1998) 1193-1202.

[303] E. Lallier, J. P. Pocholle, M. Papuchon, M. P. Demicheli, M. J. Li, Q. He, D. B. Ostrowsky, C. Grezesbesset, E. Pelletier, IEEE J. Quantum Electron. 27 (1991) 618-625.

[304] E. Lallier, J. P. Pocholle, M. Papuchon, Electron. Lett. 25 (1989) 1491-1492.

[305] E. Lallier, D. Papillon, J. P. Pocholle, M. Papuchon, M. Demicheli, D. B. Ostrowksy, Electron. Lett. 29 (1993) 175-176.

[306] E. Lallier, J. P. Pocholle, M. Papuchon, Q. He, M. de Micheli, D. B. Ostrowksy, Electron. Lett. 28 (1992) 1428-1429.

[307] E. Lallier, J. P. Pocholle, M. Papuchon, Q. He, M. Demicheli, D. B. Ostrowsky, C. Grezesbesset, E. Pelletier, Electron. Lett. 27 (1991) 936-937.

[308] M. Fujimura, H. Tsuchimoto, T. Suhara, Jpn. J. Appl. Phys., 46 (2007) 5447-5449.

[309] M. Fujimura, H. Tsuchimoto, T. Suhara, IEEE Photon. Technol. Lett. 17 (2005) 130-132.

[310] P. D. Townsend, P.J. Chandler, L. Zhang, "*Optical effects of ion implantation*" Cambridge Series in Modern Optics, Cambridge Univ. Press, Cambridge, 1994.

[311] F. Chen, X.-L. Wang, K.-M. Wang, Opt. Mater. 29 (2007) 1523-1542.

[312] A. Polman, J. Appl. Phys. 82 (1997) 1-39.

[313] F. Chen, J. Appl. Phys. 106 (2009) 081101.

[314] F. Chen, Y. Tan, D. Jaque, Opt. Lett. 34 (2009) 28-30.

[315] C. E. Chryssou, A. J. Kenyon, T. M. Smeeton, C. J. Humphreys, D. E. Hole, Appl. Phys. Lett. 85 (2004) 5200-5202.

[316] J. Rams, J. Olivares, P. J. Chandler, P. D. Townsend, J. Appl. Phys. 87 (2000) 3199-3202.

[317] F. P. Strohkendl, D. Fluck, P. Günter, R. Irmscher, C. Buchal, Appl. Phys. Lett. 59 (1991) 3354-3356.

[318] P. Moretti, M. F. Joubert, S. Tascu, B. Jacquier, M. Kaczkan, M. Malinowskii, J. Samecki, Opt. Mater. 24 (2003) 315-319.

[319] M. Domenech, G. V. Vázquez, E. Cantelar, G. Lifante, Appl. Phys. Lett. 83 (2003) 4110-4112.

[320] P. J. Chandler, S. J. Field, D. C. Hanna, D. P. Shepherd, P. D. Townsend, A. C. Tropper, L. Zhang, Electron. Lett. 25 (1989) 985-987.

[321] S. J. Field, D. C. Hanna, D. P. Shepherd, A. C. Tropper, P. J. Chandler, P. D. Townsend, L. Zhang, IEEE J. Quantum Electron. 27 (1991) 428-433.

[322] D. C. Hanna, J. K. Jones, A. C. Large, D. P. Shepherd, A. C. Tropper, P. J. Chandler, M. J. Rodman, P. D. Townsend, L. Zhang, Opt. Commun. 99 (1993) 211-215.

[323] S. J. Field, D. C. Hanna, A. C. Large, D. P. Shepherd, A. C. Tropper, P. J. Chandler, P. D. Townsend, L. Zhang, Opt. Commun. 86 (1991) 161-166.

[324] S. J. Field, D. C. Hanna, D. P. Shepherd, A. C. Tropper, P. J. Chandler, P. D. Townsend, L. Zhang, Electron. Lett. 26 (1990) 1826-1827.

[325] S. J. Field, D. C. Hanna, D. P. Shepherd, A. C. Tropper, P. J. Chandler, P. D. Townsend, L. Zhang, Opt. Lett. 16 (1991) 481-483.

[326] S. J. Field, D. C. Hanna, A. C. Large, D. P. Shepherd, A. C. Tropper, P. J. Chandler, P. D. Townsend, L. Zhang, Electron Lett. 27 (1991) 2375-2376.

[327] S. J. Field, D. C. Hanna, A. C. Large, D. P. Shepherd, A. C. Tropper, P. J. Chandler, P. D. Townsend, L. Zhang, Opt. Lett. 17 (1992) 52-54.

[328] M. E. Sánchez-Morales, G. V. Vázquez, E. B. Mejía, H. Márquez, J. Rickards, R. Trejo-Luna, Appl. Phys. B 94 (2009) 215-219.

[329] D. P. Shepherd, D. J. B. Brinck, J. Wang, A. C. Tropper, D. C. Hanna, G. Kakarantzas, P. D. Townsend, Opt. Lett. 19 (1994) 954-956.

[330] Y. Ren, N. Dong, F. Chen, A. Benayas, D. Jaque, F. Qiu, T. Narusawa, Opt. Lett. 35 (2010) 3276–3278.

[331] Y. Ren, N. Dong, F. Chen, D. Jaque, Opt. Express 19 (2011) 5522-5527.

[332] L. Laversenne, P. Hoffmann, M. Pollnau, P. Moretti, J. Mugnier, Appl. Phys. Lett. 85 (2004) 5167-5169.

[333] M. Pollnau, C. Grivas, L. Laversenne, J. S. Wilkinson, R. W. Eason, D. P. Shepherd, Laser Phys. Lett. 4 (2007) 560-571.

[334] C. Grivas, L. Laversenne, C. N. Borca, P. Moretti, D. P. Shepherd, R. W. Eason, M. Pollnau, Opt. Lett. 31 (2006) 3450-3452.

[335] E. Flores-Romero, G. V. Vazquez, H. Marquez, R. Rangel-Rojo, J. Rickards, R. Trejo-Luna, Opt. Express 12 (2004) 2264-2269.

[336] M. Domenech, G. V. Vazquez, E. Flores-Romero, E. Cantelar, G. Lifante, Appl. Phys. Lett. 86 (2005) 151108.

[337] Y. Ren, N. Dong, Y. Tan, J. Guan, F. Chen, Q. Lu, J. Lightwave Technol. 28 (2010) 3578–3581.

[338] A. A. Bettiol, S.Y. Chiam, E. J. Teo, C. Udalagama, S. F. Chan, S. K. Hoi, J. A. van Kan, M. B. H. Breese, F. Watt, Nucl. Instr. Meth. Phys. Res. B 267 (2009) 2280-2284.

[339] A. Benayas, D. Jaque, Y. Yao, F. Chen, A. A. Bettiol, A. Rodenas, A. K. Kar, Opt. Lett. 35 (2010) 3898-3900.

[340] Y. Yao, Y. Tan, N. Dong, F. Chen, A. A. Bettiol, Opt. Express 18 (2010) 24516-24521.

[341] K. Liu, E. Y. B. Puna, T. C. Sum, A. A. Bettiol, J. A. van Kan, F. Watt, Appl. Phys. Lett. 84 (2004) 684-686.

[342] M. Svalgaard, C. V. Poulsen, A. Bjarklev, O. Poulsen, Electron. Lett. 30 (1994) 1401–1403.

[343] V. Mizrahi, P. J. Lemaire, T. Erdogan, W. A. Reed, D. J. Di Giovanni, R. M. Atkins, Appl. Phys. Lett. 63 (1993) 1727-1729.

[344] D. Zauner, K. Kulstad, J. Rathje, M. Svalgaard, Electron. Lett. 34 (1998) 1582-1584.

[345] G. D. Emmerson, C. B. E. Gawith, S. P. Watts, R. B. Williams, P. G. R. Smith, S. G. McMeekin, J. R. Bonar, R. I. Laming, IEE Proc.-Optoelectron. 151 (2004) 119-122.

[346] A. K. Mairaj, X. Feng, D. P. Shepherd, D. W. Hewak, Appl. Phys. Lett.. 85 (2004) 2727-2729.

[347] A. K. Mairaj, A. M. Chardon, D. P. Shepherd, D. W. Hewak, J. Sel. Top. Quantum Electron. 8 (2002) 1381-1388.

[348] K. Miura, J. R. Qiu, H. Inouye, T. Mitsuyu, K. Hirao, Appl. Phys. Lett. 71 (1997) 3329-3331.

[349] R. R. Gattass, E. Mazur, Nature Photon. 2 (2008) 219-225.

[350] M. Ams, G. D. Marshall, P. Dekker, J. A. Piper, M. J. Withford, Laser & Photon. Rev. 3 (2009) 535-544.

[351] R. Osellame, S. Taccheo, M. Marangoni, R. Ramponi, P. Laporta, D. Polli, S. De Silvestri, G. Cerullo, J. Opt. Soc. Amer. B 20 (2003) 1559-1567.

[352] M. Ams, G. D. Marshall, D. J. Spence, M. J. Withford, Opt. Express 13 (2005) 5676-5681.

[353] J. R. Liu, Z.Y. Zhang, C. Flueraru, X. P. Liu, S. D. Chang, C. P. Grover, IEEE J. Sel. Top. Quantum Electron. 10 (2004) 169-173.

[354] R. R. Thomson, A. S. Bockelt, E. Ramsay, S. Beecher, A. H. Greenaway, A. K. Kar, D. T. Reid, Opt. Express 16 (2008) 12786-12793.

[355] P. G. Kazansky, W. Yang, E. Bricchi, J. Bovatsek, A. Arai, Y. Shimotsuma, K. Miura, K. Hirao, Appl. Phys. Lett. 90 (2007) 151120.

[356] W. Yang, P. G. Kazansky, Y. P. Svirko, Nature Photon. 2 (2008) 99-104.

[357] W. Yang, C. Corbari, P. G. Kazansky, K. Sakaguchi, I. C. S. Carvalho, Opt. Express 16 (2008) 16215-16226

[358] V. Apostolopoulos, L. Laversenne, T. Colomb, C. Depeursinge, R. P. Salathé, M. Pollnau, R. Osellame, G. Cerullo, P. Laporta, Appl. Phys. Lett. 85 (2005) 1122-1124.

[359] G. D. Marshall, P. Dekker, M. Ams, J. A. Piper, M. J. Withford, Opt. Lett. 33 (2008) 956-958.

[360] M. Ams, P. Dekker, G. D. Marshall, M. J. Withford, Opt. Lett. 33 (2009) 247-249.

[361] R. Osellame, N. Chiodo, G. Della Valle, G. Cerullo, R. Ramponi, P. Laporta, A. Killi, U. Morgner, O. Svelto, J. Sel. Top. Quantum Electron. 12 (2006) 277-285.

[362] G. Della Valle, S. Taccheo, R. Osellame, A. Festa, G. Cerullo, P. Laporta, Opt. Express 15 (2007) 3190-3194.

[363] S. Taccheo, G. Della Valle, R. Osellame, G. Cerullo, N. Chiodo, P. Laporta, O. Svelto, A. Killi, U. Morgner, M. Lederer, D. Kopf, Opt. Lett. 29 (2004) 2626-2628.

[364] G. Della Valle, R. Osellame, G. Galzerano, N. Chiodo, G. Cerullo, P. Laporta, O. Svelto, U. Morgner, A. G. Rozhin, V. Scardaci, A. C. Ferrari, Appl. Phys. Lett. 89 (2006) 231115.

[365] N. D. Psaila, R. R. Thomson, H. T. Bookey, N. Chiodo, S. Shen, R. Osellame, G. Cerullo, A. Jha, A. K. Kar, IEEE Photon. Technol. Lett. 20 (2008) 126-128.

[366] S. J. Beecher, R. R. Thomson, N. D. Psaila, Z. Sun, T. Hasan, A. G. Rozhin, A. Ferrari, A. K. Kar. Appl. Phys. Lett. 97 (2010) 111114.

[367] F. Fusari, R. R. Thomson, G. Jose, F. M. Bain, A. A. Lagatsky, N. D. Psaila, A. K. Kar, A. Jha, W. Sibbett, C. T.A. Brown Opt. Lett. 36 (2011) 1566-1568.

[368] D. G. Lancaster, S. Gross, H. Ebendorff-Heidepriem, K. Kuan, T. M. Monro, M. Ams, A. Fuerbach, M. J. Withford, Opt. Lett. 36 (2011) 1587-1589.

[369] A. G. Okhrimchuk, A.V. Shestakov, I. Khrushchev, J. Mitchell, Opt. Lett. 30 (2005) 2248-2250.

[370] J. Siebenmorgen, K. Petermann G. Huber, K. Rademaker, S. Nolte, A. Tünnermann, Appl. Phys. B 97 (2009) 251-255.

[371] T. Calmano, J. Siebenmorgen, O. Hellmig, K. Petermann, G. Huber, Appl. Phys. B 100 (2010) 131-135.

[372] Y. Tan, A. Rodenas, F. Chen, R. R. Thomson, A. K. Kar, D. Jaque, Q. Lu, Opt. Express 18 (2010) 24994-24999.

[373] Y. Tan, F. Chen, J. R. Vázquez de Aldana, G. A. Torchia, A. Benayas, D. Jaque, Appl. Phys. Lett. 97 (2010) 031119.

[374] J. Siebenmorgen, O. Hellmig, K. Petermann, G. Huber, Opt. Express 18 (2010) 16035-16041.

[375] F. M. Bain, A. A. Lagatsky, R. R. Thomson, N. D. Psaila, N. V. Kuleshov, A. K. Kar, W. Sibbett, C. T. A. Brown, Opt. Express 17 (2009) 22417-22422.

[376] G. A. Torchia, A. Rodenas, A. Benayas, E. Cantelar, L. Roso, D. Jaque, Appl. Phys. Lett. 92 (2008) 111103.

[377] T. Calmano, A.-G. Paschke, J. Siebenmorgen, S.T. Fredrich-Thornton, H. Yagi, K. Petermann, G. Huber, Appl. Phys. B 103 (2011) 1-4.

[378] K. Kawamura, M. Hirano, T. Kurobori, D. Takamizu, T. Kamiya, H. Hosono, Appl. Phys. Lett. 84 (2004) 311-313.

[379] T. M. Monro, D. Moss, M. Bazylenko, C. M. de Sterke, L. Poladian, Phys. Rev. Lett. 80 (1998) 4072-4075.

[380] A. S. Kewitsch, A. Yariv, Opt. Lett. 21 (1996) 24-26.

[381] K. Saravanamuttu, M. P. Andrews, Opt. Lett. 27 (2002) 1342-1344.

[382] K. Yamashita, A. Kitanobou, M. Ito, E. Fukuzawa, K. Oe, Appl. Phys. Lett. 92 (2008) 143305.

[383] K. Yamashita, M. Ito, E. Fukuzawa, H. Okada, K. Oe, J. Lightwave Technol. 27 (2009) 4570-4574.

[384] K. Yamashita, M. Ito, S. Sugimoto, T. Morishita, K. Oe, Opt. Express 18 (2010) 24092-24100.

[385] O. Sugihara, H. Tsuchie, H. Endo, N. Okamoto, T. Yamashita, M. Kagami, T. Kaino, IEEE Photon. Technol. Lett. 16 (2004) 804-806.

[386] K. Yamashita, T. Kuro, K. Oe, K. Mune, T. Hikita, A. Mochizuki, IEEE Photon. Technol. Lett. 17 (2005) 786-788.

[387] M. J. Madou, "*Fundamentals of Microfabrication: The Science of Miniaturization"* 2nd ed., Boca Raton, FL. (2002).

[388] A. Crunteanu, M. Pollnau, G. Jänchen, C. Hibert, P. Hoffmann, R. P. Salathé, R. W. Eason, C. Grivas, D. P. Shepherd, Appl. Phys. B 75 (2002) 15-17.

[389] C. Grivas, T. C. May-Smith, D. P. Shepherd, R. W. Eason, M. Pollnau, M. Jelínek, Appl. Phys. A 79 (2004) 1195-1998.

[390] Z. Ren, P. J. Heard, J. M. Marshall, P. A. Thomas, S. Yu, J. Appl. Phys. 103 (2008) 034109.

[391] J. D. B. Bradley, F. Ay, K. Wörhoff, M. Pollnau, Appl. Phys. B 67 (1998) 311-318.

[392] S. Mailis, G. W. Ross, L. Reekie, J. A. Abernethy, R. W. Eason, Electron. Lett. 36 (2000) 1801-1803.

[393] F. Laurell, J. Webjorn, G. Arvidsson, J. Holmberg, J. Lightwave Technol. 10 (1992) 1606-1609.

[394] A. Crunteanu, G. Jänchen, P. Hoffmann, M. Pollnau, C. Buchal, A. Petraru, R. W. Eason, D. P. Shepherd, Appl. Phys. A 76 (2003) 1109-1112.

[395] Y. Xia, G. M. Whitesides, Angew. Chem. Int. Ed. 37 (1998) 550-575.

[396] B. D. Gates, Q. Xu, C. Love, D. B. Wolfe, G. M. Whitesides, Annu. Rev. Mater. Res. 34 (2004) 339-372.

[397] S. Y. Chou, P. R. Krauss, P. J. Renstrom, Science 272 (1996) 85-87.

[398] H. Ma, A. K.-Y. Jen, L. R. Dalton, Adv. Mater. 14 (2002) 1339-1365.

[399] E. Menard, M. A. Meitl, Y. Sun, J.-U. Park, D. J.-L. Shir, Y.-S. Nam, S. Jeon, J. A. Rogers, Chem. Rev. 107 (2007) 1117-1160.

[400] W.-S. Kim, J.-H. Lee, S.-Y. Shin, B.-S. Bae, Y.-C. Kim, IEEE Photon. Technol. Lett. 16 (2004) 1888-1890.

[401] J. A. Rogers, M. Meier, A. Dodabalapur, E. J. Laskowski, M. A. Cappuzzo, Appl. Phys. Lett. 74 (1999) 3257-3259.

[402] J. R. Lawrence, G. A. Turnbull, I. D. W. Samuel, Appl. Phys Lett. 82 (2003) 4023-4025.

[403] M. Gaal, C. Gadermaier, H. Plank, E. Moderegger, A. Pogantsch, G. Leising, E. J. W. List, Adv. Mater. 15 (2003) 1165-1167.

[404] E. B. Namdas, M. Tong, P. Ledochowitsch, S. R. Mednick, J. D. Yuen, D. Moses, A. J. Heeger, Adv. Mater. 21 (2009) 799-802.

[405] M. Ichikawa, Y. Tanaka, N. Suganuma, T. Koyama, Y. Taniguchi, Jpn. J. Appl. Phys. 42 (2003) 5590-5593.

[406] K. Yamashita, M. Arimatsu, M. Takayama, K. Oe, H. Yanagi, Appl. Phys. Lett. 92 (2008) 243306.

[407] K. Yamashita, N. Takeuchi, K. Oe, H. Yanagi, Opt. Lett. 35 (2010) 2451-2453.

[408] D. Pisignano, L. Persano, M. F. Raganato, P. Visconti, R. Cingolani, G. Barbarella, L. Favaretto, G. Gigli, Adv. Mater. 16 (2004) 525-529.

[409] D. Pisignano, L. Persano, P. Visconti, R. Cingolani, G. Gigli, G. Barbarella, L. Favaretto, Appl. Phys. Lett. 83 (2003) 2545-2548.

[410] D. Pisignano, L. Persano, E. Mele, P. Visconti, M. Anni, G. Gigli, R. Cingolani, L. Favaretto, G. Barbarella, Synth. Met. 153 (2005) 237-240.

[411] J. Lančok, M. Jelínek, J. Bulír, P. Macháč, Laser Phys. 8 (1998) 303-306.

[412] J. Gottmann, L. Moiseev, I. Vasilief, D. Wortmann, Mat. Sci. Eng. B 146 (2008) 245-251.

[413] A. J. Pedraza, Nucl. Instrum. Methods B 141 (1998) 709-718.

[414] J. Gottmann, D. Wortmann, I. Vasilief, L. Moiseev, D. Ganser, Appl. Surf. Sci. 254 (2007) 1105-1110.

[415] D. Bäuerle "*Lasers processing and chemistry"* (Springer-Verlag, 2000).

FIGURES CAPTIONS

Figure 1: Geometry of: (a) an asymmetric slab waveguide ($n_1 > n_2 > n_0$), and, (b) a symmetric slab waveguide with its refractive index profile and a propagating light ray in its core.

Figure 2: Different types of channel waveguides: (a) embedded, (b) strip, (c) rib or, ridge, and (d) strip-loaded.

Figure 3: Output power from two Ti:sapphire waveguide lasers, with channel (rib) and slab geometry, respectively, as a function of absorbed power for ~4.6% outcoupling. Both lasers have comparable losses and exhibit similar slope efficiencies however, the rib source has a considerably lower lasing threshold (~ 475 mW) than the slab one (~ 1030 mW), largely due to the better overlap of the pump and laser beams [13, 14].

Figure 4: Calculated maximum temperature increase $\Delta T_{\max}$ in a microthickness YAG:Yb^{3+} slab laser as a function of pump power P_p for various width (w) to thickness (d) aspect ratios. The slab cross section $S = w \cdot d$ was assumed to be 2 mm [22]. (Reprinted with permission from K. Sueda, H. Takahashi, S. Kawato, T. Kobayashi, "High-efficiency laser-diodes-pumped microthickness Yb:$Y_3Al_5O_{12}$ slab laser," Applied Physics Letters vol. 87, 151110, Copyright 2005, American Institute of Physics).

Figure 5: Measured and calculated cw SHG tuning curve for a 3.3-cm-long $LiNbO_3$ waveguide, indicating a peak normalized conversion efficiency of approximately $150\%/W \cdot cm^2$. The nearly ideal $sinc^2$ shape of the curve suggests that phase matching is maintained throughout the device length [36]. (Reprinted with permission from Optics Letters, K. R. Parameswaran, R. K. Kurz, J. R. Kurz, R. V. Roussev, M. M. Fejer, M. Fujimura, "Highly efficient second-harmonic generation

in buried waveguides formed by annealed and reverse proton exchange in periodically poled lithium niobate," vol. 27, pp. 179-181, © 2002 Optical Society of America).

Figure 6: a) Scanning electron microscope (SEM) micrograph of an on-chip OPO based on a silicon nitride (Si_3N_4) microring resonator coupled to a bus waveguide. b) Optical parametric oscillation leading to emission at numerous precisely defined wavelengths was achieved in this device by tuning the emission wavelength of the pump laser to the resonance of the microring [37]. (Reprinted by permission from Macmillan Publishers Ltd: Nature Photonics, www.nature.com/nphoton/index.html, J. S. Levy, A. Gondarenko, M. A. Foster, A. C. Turner-Foster, A. L. Gaeta, M. Lipson, "CMOS-compatible multiple-wavelength oscillator for on-chip optical interconnects," vol. 4, pp. 37-40, Copyright 2009).

Figure 7: (a) Layout of the cavity of an integrated femtosecond waveguide laser consisting of two sections: a 5-cm (Er)-doped alumino–silicate waveguide with group-velocity dispersion (GVD) of 30 fs^2/mm, and a 20-cm of phosphorous-doped silica waveguide with GVD of -25 fs^2/mm. The latter is used to obtain net anomalous intracavity dispersion for soliton mode-locking operation. The inset shows the reflection and dispersion spectra of the saturable Bragg reflector (SBR) element that was used to start the mode-locking and stabilize the soliton. (b) Picture of the laser setup. (c) RF spectrum (3-GHz span, 10-MHz resolution), indicating an operating repetition rate of 394 MHz. (d) Background free autocorrelation trace showing that the pulses produced had a duration of 438 fs [44]. (Reprinted with permission from IEEE Photonics Technology Letters, vol. 21, H. Byun, D. Pudo, S. Frolov, A. Hanjani, J. Shmulovich, E. P. Ippen, F. X. Kärtner, "Integrated Low-Jitter 400-MHz Femtosecond Waveguide Laser," pp. 763-765, © 2009 IEEE).

Figure 8: Schematic of an integrated DFB–DBR coupled cavity laser based on a single-mode channel waveguide. It was fabricated by thermal indiffusion of titanium ions into an Er:$LiNbO_3$ section (DBR laser) and an Er:Fe:$LiNbO_3$ section (DFB laser) of the same crystal. The abbreviations AR and WDM stand for antireflection and wavelength division demultiplexer, respectively [46]. (Reprinted with permission from Optics Letters, B. K. Das, R. Ricken, V. Quiring, H. Suche, W. Sohler, "Distributed feedback distributed Bragg reflector coupled cavity laser with a Ti:(Fe:)Er:$LiNbO_3$ waveguide," vol. 29, pp. 165-167, © 2004 Optical Society of America).

Figure 9: (a) Output power as a function of launched pump power for the Ti:Er:$LiNbO_3$ waveguide laser with the integrated DFB–DBR coupled cavity shown in Fig. 8. (b) Single-frequency emission of one DFB mode in resonance with one DBR cavity mode. FSR=15 GHz is the free spectral range of the Fabry–Perot spectrum analyzer used to record the spectrum [46]. (Reprinted with permission from Optics Letters, B. K. Das, R. Ricken, V. Quiring, H. Suche, W. Sohler, "Distributed feedback distributed Bragg reflector coupled cavity laser with a Ti:(Fe:)Er:$LiNbO_3$ waveguide," vol. 29, pp. 165-167, © 2004 Optical Society of America).

Figure 10: Experimental set-up for loss measurements in Ti:sapphire rib waveguides using the SPPC technique. In this arrangement, L1 and L2, are a pair of cylindrical lenses for pump-beam shaping, WBS 1, 2 are wedged beam splitters and PD 3, 4 and PD 1, 2 are photodiodes for detection of the incident and phase-conjugate signals before and after their passing through the rib waveguides, respectively [58].

Figure 11: Typical arrangement for loss measurements in active waveguides using the fluorescence imaging technique. The filter shown in the set-up is employed to block the

excitation light and in combination with a lock-in amplifier it ensures that only the fluorescence light is detected [62]. (Reprinted with permission from Journal of Optical Society of America B, A. Kahn,Y. Kuzminykh, H. Scheife, G. Huber, "Nondestructive measurement of the propagation losses in active planar waveguides," vol. 24, pp. 1571-1574, © 2007 Optical Society of America).

Figure 12: Schematic of a LPE arrangement used for growth of monoclinic double tungstate waveguide layers, in particular $KY(WO_4)$ [65]. (Reprinted with permission from IEEE Journal of Selected Topics in Quantum Electronics, vol. 13, M. Pollnau, Y. E. Romanyuk, F. Gardillou, C. N. Borca, U. Griebner, S. Rivier, V. Petrov, "Double Tungstate Lasers: From Bulk Toward On-Chip Integrated Waveguide Devices," pp. 661-671 © 2007 IEEE).

Figure 13: Lattice-matched $KY_{0.59}Gd_{0.19}Lu_{0.22}(WO_4)_2$ layers grown on $KY(WO_4)_2$ substrates: (a) scheme of the atomic percentage of Y, Gd and Lu across the substrate and the epitaxial layer as calculated from the EPMA results. Optimization of the relative concentrations of Y, Gd, and Lu is critical for achieving lattice-matched growth. (b) ESEM picture of a $KY_{0.59}Gd_{0.19}Lu_{0.22}(WO_4)_2$/ $KY(WO_4)_2$ interface obtained using backscattered electrons, and (c) photograph of the planar $KY_{0.59}Gd_{0.19}Lu_{0.22}(WO_4)_2/KY(WO_4)_2$ structure [67]. (Reprinted with permission from Crystal Growth and Design, W. Bolaňos, J. J. Carvajal, M. C. Pujol, X. Mateos, G. Lifante, M. Aguiló, F. Díaz, "Epitaxial Growth of Lattice Matched KY_{1-x-y} $Gd_xLu_y(WO_4)_2$ Thin Films on $KY(WO_4)_2$ Substrates for Waveguiding Applications," vol. 9, pp. 3525-3531, Copyright 2009, American Chemical Society).

Figure 14: PLD configuration for growth of Ti:sapphire and doped GGG:Nd^{3+} waveguide layers. To prevent contamination through desorption from the walls of the vacuum chamber due to the

high temperatures involved in the deposition process (~ 1000ºC), localized substrate heating was provided by scanning a 100-W CO_2 laser beam on the substrate [14, 102].

Figure 15: (a) Schematic of a target-substrate arrangement for combinatorial PLD experiments, comprising a rotating substrate heater and a three-beam, three-target assembly. (b) SEM micrograph of a 5-layer garnet crystal structure produced by combinatorial PLD [93]. (Reprinted from Applied Surface Science, 255, R. W. Eason, T. C. May-Smith, C. Grivas, M. S. B. Darby, D. P. Shepherd, R. Gazia, "Current state-of-the-art of pulsed laser deposition of optical waveguide structures: Existing capabilities and future trends," pp. 5199-5205, Copyright 2009, with permission from Elsevier).

Figure 16: Schematic of a PECVD apparatus employed for deposition of Al_2O_3 films. A carrier gas (argon) was used to transport the precursor trimethyl-amine alane $(CH_3)_3NAlH_3$ (TMAA) to the reaction site, where it reacted with N_2O to produce a solid Al_2O_3 layer on a heated (300 ºC) substrate [133]. (With kind permission from Springer Science + Business Media: Applied Physics A, "Al_2O_3 thin films by plasma-enhanced chemical vapour deposition using trimethyl-amine alane (TMAA) as the Al precursor," vol. 65, 1997, pp. 469-475, C. E. Chryssou, C. W. Pitt, Fig . 1).

Figure 17: (a) Schematic of an array of four waveguide lasers based on channels with different widths, where one of the output sides is combined using Y splitters. The array was produced by a combination of PECVD and RIE, and a pair of gratings was inscribed over each channel by exposure to UV irradiation through a single phase mask. (b) A laser spectrum as obtained from the array, where the differences in lasing wavelengths indicated are entirely determined by the waveguide width [128]. (Reprinted with permission from: Optical Engineering, M. R. Poulsen, P.

I. Borel, J. Fage-Pedersen, J. Hübner, M. Kristensen, J. H. Povlsen, K. Rottwitt, M. Svalgaard, W. Svendsen, "Advances in silica-based integrated optics," vol. 42 pp. 2821-2834, Copyright 2003, SPIE-International Society for Optical Engineering).

Figure 18: Typical set-up for FHD fabrication of planar optical waveguides. A mixture of vapour precursors is fed into an oxy/hydrogen torch and films are deposited on silica glass substrates placed on a turn-table [136]. (Reprinted with permission from Electronic Letters, vol. 19, M. Kawachi, M. Yasu, T. Edahiro, "Fabrication of SiO_2-TiO_2 glass planar optical waveguides by flame hydrolysis deposition," pp. 583-584, © 1983 IEEE).

Figure 19: Schematic of FHD configurations used for deposition of: (a) Nd-doped silica layers with inclusions of Al_2O_3 using a vapour delivery system. The Nd-ion precursor is the high-vapour-pressure organic compound $Nd(thd)_3$ [138]. (Reprinted with permission from Optics Letters, R. Tumminelli, E. Hakimi, J. Haavisto, "Integrated-optic Nd:glass laser fabricated by flame hydrolysis deposition using chelates," vol. 16, pp. 1098-1100, © 1991 Optical Society of America). (b) Nd- and Er-doped silica layers with inclusions of P_2O_5 using aerosol doping. The chlorides $SiCl_4$ and PCl_3 served as precursors of SiO_2 and P_2O_5, respectively, and nitrogen was used as a carrier gas to atomize the solution and deliver the resultant aerosol droplets to the burner [139]. (Reprinted with permission from: J. A. Bebbington, G. Barbarossa, J. R. Bonar, J. S. Aitchison, "Rare earth doped silica waveguides on Si fabricated by flame hydrolysis deposition and aerosol doping," Applied Physics Letters, vol. 62, pp. 337-339, (1993), Copyright 1993, American Institute of Physics).

Figure 20: Schematic illustrating the high versatility of the sol–gel technique in terms of chemical processes involved in fabrication, nature of the precursor materials, and shape of the

composite devices produced [151]. (Reprinted figure with permission from Journal of American Ceramic Society, S. Bhandarkar, "Sol-Gel Processing for Optical Communication Technology," vol. 87, pp.1180-1199, Copyright 2004, John Wiley and Sons).

Figure 21: Laser emission spectra obtained from a DBR laser based on the organic semiconducting gain medium Alq_3:DCM2 by pumping with power densities of a 6 kW/cm^2 (bottom) and 20 kW/cm^2 (top). The inset shows the schematic of the DBR laser, which had a cavity length of 2 mm. The gratings were formed by etching the SiO_2 substrate; the gain medium was then deposited on the substrate by thermal sublimation [185]. (Reprinted with permission from: M. Berggren, A. Dodabalapur, R. E. Slusher, "Stimulated emission and lasing in dye-doped organic thin films with Forster transfer," Applied Physics Letters, vol. 71, pp. 2230-2232, Copyright 1997, American Institute of Physics).

Figure 22: (a) Top view of the extended cavity of a diode side-pumped YAG:Yb^{3+} channel waveguide laser fabricated by diffusion bonding. A micrograph of the polished end face of the YAG:Yb^{3+} channel waveguide (cross section 100 x 80 μm^2) surrounded by a 300-μm-thick YAG cladding is also shown. (b) Output power from the YAG:Yb^{3+} channel waveguide laser as a function of absorbed pump power [217]. (Reprinted with permission from Optics Letters, U. Griebner, H. Schönnagel, "Stimulated emission and lasing in dye-doped organic thin films with Forster transfer," vol. 24, pp. 750-752, © 1999 Optical Society of America).

Figure 23: (a) Chemical structure of the $Nd(TTA)_3$phen complex [220]. (b) Laser emission spectra obtained from a $Nd(TTA)_3$phen complex-doped polymer channel waveguide for the quasi-three-level ($^4F_{3/2} \rightarrow {}^4I_{9/2}$) and four-level ($^4F_{3/2} \rightarrow {}^4I_{11/2}$) transitions near 878.0 nm and 1060.2 nm, respectively. The peaks in the bands correspond to longitudinal cavity modes [225].

Figure 24: SEM micrographs of ridges of 6.5-μm height fabricated by wet etching in a $LiNBO_3$ crystal (a) before and (b) after their indiffusion with titanium ions at 1060ºC. As a result of the high temperatures used for the diffusion process the in-diffused ridge exhibits improved sidewall smoothness and a propagation loss as low as 0.08 $dB \cdot cm^{-1}$. (c) Mode distributions obtained from a ridge waveguide with 7-μm top width for the TE (top) and the TM-polarization (bottom), respectively [230]. (With kind permission from Springer Science + Business Media: Applied Physics B, "Low-loss ridge waveguides on lithium niobate fabricated by local diffusion doping with titanium," vol. 98, 2010, pp. 677-679, H. Hu, R. Ricken, W. Sohler, Figs. 2, 3)

Figure 25: (a) Refractive index profile of a channel waveguide produced by Ag-Na ion exchange in an Er:Yb co-doped phosphate glass substrate and then buried by applying to the latter a transversal electric field. (b) Typical near-field mode profiles of a waveguide produced with this approach (green lines) compared to near-field mode profiles of a standard single-mode fiber at 1550 nm (blue lines) [255]. (Reprinted with permission from Optics Express, G. Della Valle, A. Festa, G. Sorbello, K. Ennser, C. Cassagnetes, D. Barbier, S. Taccheo, "Single mode and high power waveguide lasers fabricated by ion-exchange" vol. 16, pp. 12334-12341, © 2008 Optical Society of America).

Figure 26: Set-up for high-power laser experiments of ion-exchanged Er:Yb-coped phosphate glass channel waveguides. The abbreviations PC, and HR FBG stand for polarization controller and high-reflective fiber Bragg grating, respectively. The picture at the center shows one of these waveguides with a length of 45-mm under double-end pumping through fibers (each containing a FBG) that were butt-coupled to its two end-faces [255]. (Reprinted with permission from Optics Express, G. Della Valle, A. Festa, G. Sorbello, K. Ennser, C. Cassagnetes, D. Barbier, S.

Taccheo, “Single mode and high power waveguide lasers fabricated by ion-exchange” vol. 16, pp. 12334-12341, © 2008 Optical Society of America).

Figure 27: Schematic of a $LiNbO_3:Yb^{3+}$ waveguide laser fabricated by annealed proton exchange in a slab waveguide produced by indiffusion of a $LiNbO_3$ crystal with Yb-ions [308]. (Reproduced with permission from Japanese Journal of Applied Physics: vol. 46, issue 8B, pp. 5447-5449, 2007. M. Fujimura, H. Tsuchimoto, T. Suhara, Copyright 2007, Japanese Society of Applied Physics).

Figure 28: (a) Output power as a function of incident pump power, and (b) emission spectrum, both originating from a $LiNbO_3:Yb^{3+}$ channel waveguide laser produced by annealed proton exchange in a thermally indiffused $LiNbO_3:Yb^{3+}$ slab waveguide [308]. (Reproduced with permission from Japanese Journal of Applied Physics: vol. 46, issue 8B, pp. 5447-5449, M. Fujimura, H. Tsuchimoto, T. Suhara, Copyright 2007, Japanese Society of Applied Physics).

Figure 29: Schematic (not to scale) of the implantation design of channel waveguides in a Ti:sapphire crystal. The channels had different cross sections, namely 10 x 5 μm^2, 15 x 5 μm^2, and 25 x 5 μm^2, and were defined by optical barriers (indicated by red stripes) formed by multiple implants with different energies. The distances of these barriers from the top surface of the sample are also indicated [334].

Figure 30: (a) Simulated and (b) measured fundamental transmission mode intensity profiles of the output from a 5-μm-deep and 10-μm-wide buried proton-implanted Ti:sapphire channel waveguide obtained by coupling a fundamental-mode laser beam of 800-nm wavelength [334].

Figure 31: (a) Schematic of the waveguide writing process in YAG:Nd^{3+} crystals using the focused PBW technique. Also in the same figure, images of near-field intensity distributions of TE modes at 632 nm obtained from YAG:Nd^{3+} channel waveguides fabricated using an implantation dose of 2×10^{16} ions/cm^3 and energies of (b) 1 MeV and (c) 2 MeV (Reprinted figure with permission from [339]). (Reprinted with permission from Optics Letters, A. Benayas, D. Jaque, Y. Yao, F. Chen, A. A. Bettiol, A. Rodenas, A. K. Kar, "Microstructuring of Nd:YAG crystals by proton-beam writing," vol. 35, pp. 3898-3900, © 2010 Optical Society of America).

Figure 32: Schematic of the configuration used for one-step, simultaneous direct writing of channel waveguides and encoding of Bragg grating structures in glass substrates using cw UV irradiation. Bragg gratings of certain periodicity in the waveguide are formed by modulating the frequency of the UV light so as to match the scanning speed and their strength is modulated by slightly detuning the modulation frequency of the UV light [345]. (Reprinted with permission from IEE Proceedings Optoelectronics, vol. 151, G. D. Emmerson, C. B. E. Gawith, S. P. Watts, R. B. Williams, P. G. R. Smith, S. G. McMeekin, J. R. Bonar, R. I. Laming, "All-UV-written integrated planar Bragg gratings and channel waveguides through single-step direct grating writing," pp. 119-122, © 2004 IEEE).

Figure 33: Picture of the endface of a depressed cladding waveguide produced by femtosecond (fs) laser writing in a YAG:Nd^{3+} crystal. The core, which has a size of 100 μm x 13 μm, was defined by fs-laser-written tracks, whose refractive index averaged across their cross section is smaller relative to that of the host crystal [369]. (Reprinted with permission from Optics Letters, A. G. Okhrimchuk, A.V. Shestakov, I. Khrushchev, J. Mitchell, "Depressed cladding, buried waveguide laser formed in a YAG:Nd^{3+} crystal by femtosecond laser writing," vol. 30, pp. 2248-2250, © 2005 Optical Society of America).

Figure 34: (a) Microscope image obtained under crossed polarizers of the cross section of a pair of tracks written in an undoped 45-μm-thick YAG crystal using femtosecond laser pulses. (b) Near-field image of the guided laser mode from a channel waveguide inscribed in a YAG:Nd^{3+} crystal as recorded by a CCD camera [370]. (With kind permission from Springer Science + Business Media: Applied Physics B, "Femtosecond laser written stress-induced Nd:$Y_3Al_5O_{12}$ (Nd:YAG) channel waveguide laser," vol. 97, 2009, pp. 251-255, J. Siebenmorgen, K. Petermann G. Huber, K. Rademaker, S. Nolte, A. Tünnermann, Figs. 4c, 10).

Figure 35: Schematic of the fabrication process and operation of a self-written channel waveguide laser with Fabry-Perot (FP) cavity. (a) The fibers used for writing are aligned and positioned within two grooves and the FP-cavity is formed by two the half-mirrors placed into the gap between fibers; the gain medium is then casted in-between these mirrors. (b) Channel waveguide writing in the dye-doped polymer by launching UV light through the two fiber tips. (c) Lasing operation under optical pumping; the uncured part of the gain medium was removed [383]. (Reprinted with permission from Journal of Lightwave Technology, vol. 27, K. Yamashita, M. Ito, E. Fukuzawa, H. Okada, K. Oe, "Device Parameter Analyses of Solid-State Organic Laser Made by Self-Written Active Waveguide Technique," pp. 4570-4574, © 2009 IEEE).

Figure 36: Schematic of the steps followed for fabrication of rib waveguides in PLD-deposited Ti:sapphire films using a combination of photolithography and IBE: (a) spin coating of the Ti:sapphire layer by a negative photoresist, (b) exposure to UV light through a photolithographic mask, (c) development of the photoresist to produce stripped photoresist patterns, (d) IBE of the uncovered Ti:sapphire surfaces, (e) removal of the photoresist remnants to obtain rib structures. The inset shows details of the resulting structures [58].

Figure 37: SEM image of Ar^+-beam-structured rib waveguides in a 10-μm-thick PLD-grown Ti:sapphire layer obtained following the process displayed in Fig. 36 [389].

Figure 38: Schematic of a typical configuration for inductively coupled plasma (ICP) etching [390]. (Reprinted with permission from: Z. Ren, P. J. Heard, J. M. Marshall, P. A. Thomas, S. Yu, "Etching characteristics of $LiNbO_3$ in reactive ion etching and inductively coupled plasma" Journal of Applied Physics vol. 103, 034109, (2008), Copyright 2008, American Institute of Physics).

Figure 39: Schematic of the UV-NIL fabrication flow of Bragg gratings on top of Alq_3:DCM2 ridge waveguides to produce DFB resonators. An elastomeric mold transparent at 337 nm was used for imprinting [401]. (Reprinted with permission from: J. A. Rogers, M. Meier, A. Dodabalapur, E. J. Laskowski, M. A. Cappuzzo, "Distributed feedback ridge waveguide lasers fabricated by nanoscale printing and molding on nonplanar substrates," Applied Physics Letters vol. 74, pp. 3257-3259, (1999), Copyright 1999, American Institute of Physics).

Figure 40: (a) SEM image of a waveguide array fabricated in a hexagonal mesostructured silica-$EO_{20}PO_{70}EO_{20}$ composite layer using MIMIC. (b) Laser scanning confocal microscopy image of a waveguide array produced by MIMIC in a Rh6G-doped mesostructured silica-$EO_{20}PO_{70}EO_{20}$ layer as obtained by pumping at 514 nm [178]. (From: P. Yang, G. Wirnsberger, H. C. Huang, S. R. Cordero, M. D. McGehee, B. Scott, T. Deng, G. M. Whitesides, B. F. Chmelka, S. K. Buratto, G. D. Stucky, "Mirrorless Lasing from Mesostructured Waveguides Patterned by Soft Lithography," Science vol. 287, 2000, pp. 465-467. Reprinted with permission from AAAS.)

Figure 41: (a) SEM image of a DFB grating, imprinted by UV-NIL into a thin film of the UV-curable resin PAC-01-CL doped with the laser dye Rhodamine 610. (b) Laser spectrum obtained from the DFB waveguide laser by pulsed pumping at 337 nm with an optical pumping density of ~1.2 mJ/cm^2. The inset shows the DFB device under optical pumping [406]. (Reprinted with permission from: K. Yamashita, M. Arimatsu, M. Takayama, K. Oe, H. Yanagi, "Simple fabrication technique of distributed-feedback polymer laser by direct photonanoimprint lithography," Applied Physics Letters, vol. 92, 243306, (2008), Copyright 2008, American Institute of Physics).

FIGURES

C. Grivas "***Optically pumped planar waveguide lasers Part I: fundamentals and fabrication techniques***"

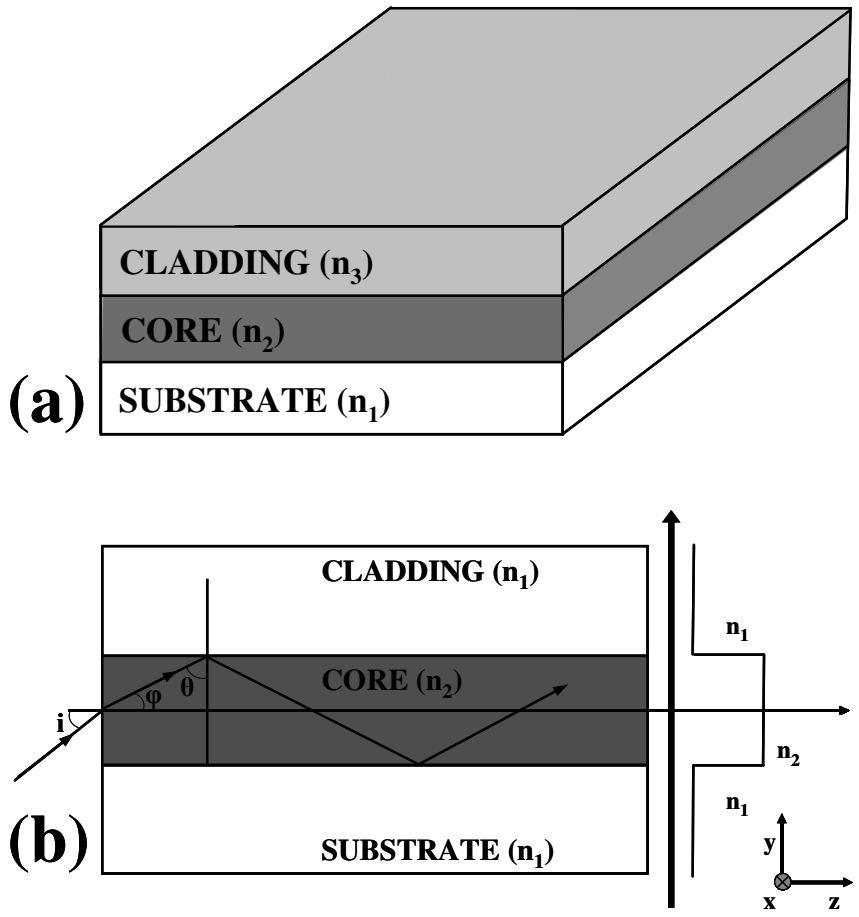

Figure 1: Geometry of: (a) an asymmetric slab waveguide ($n_1 > n_2 > n_0$), and, (b) a symmetric slab waveguide with its refractive index profile and a propagating light ray in its core.

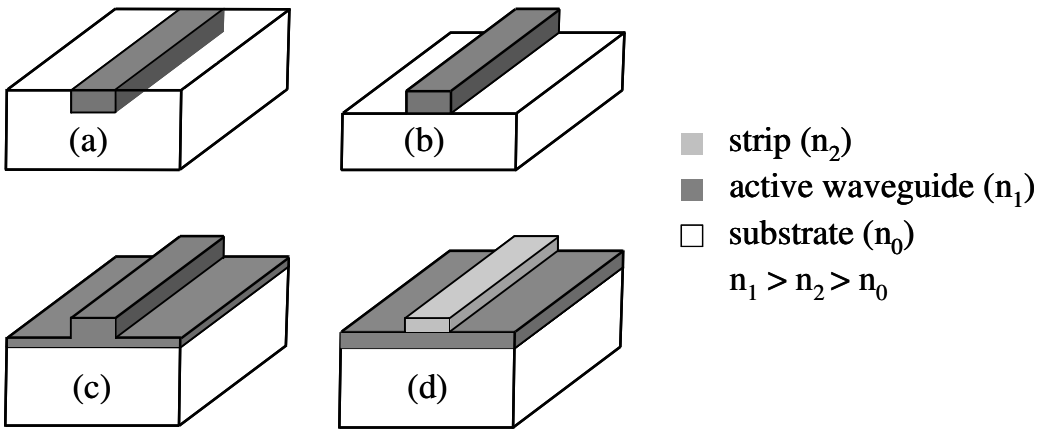

Figure 2: Different types of channel waveguides: (a) embedded, (b) strip, (c) rib or, ridge, and (d) strip-loaded.

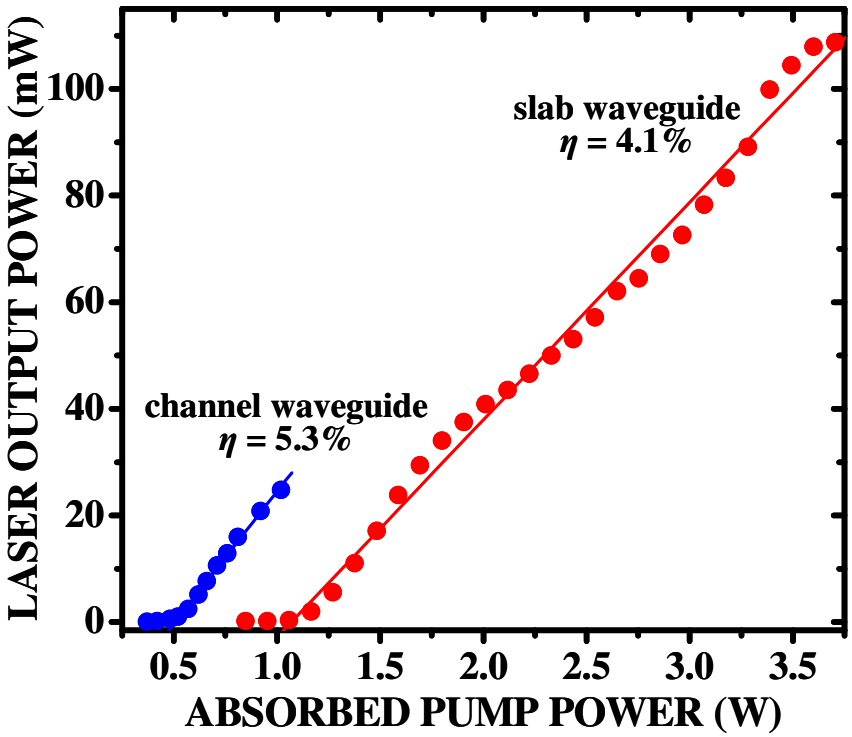

Figure 3: Output power from two Ti:sapphire waveguide lasers, with channel (rib) and slab geometry, respectively, as a function of absorbed power for ~4.6% outcoupling. Both lasers have comparable losses and exhibit similar slope efficiencies however, the rib source has a considerably lower lasing threshold (~ 475 mW) than the slab one (~ 1030 mW), largely due to the better overlap of the pump and laser beams [13, 14].

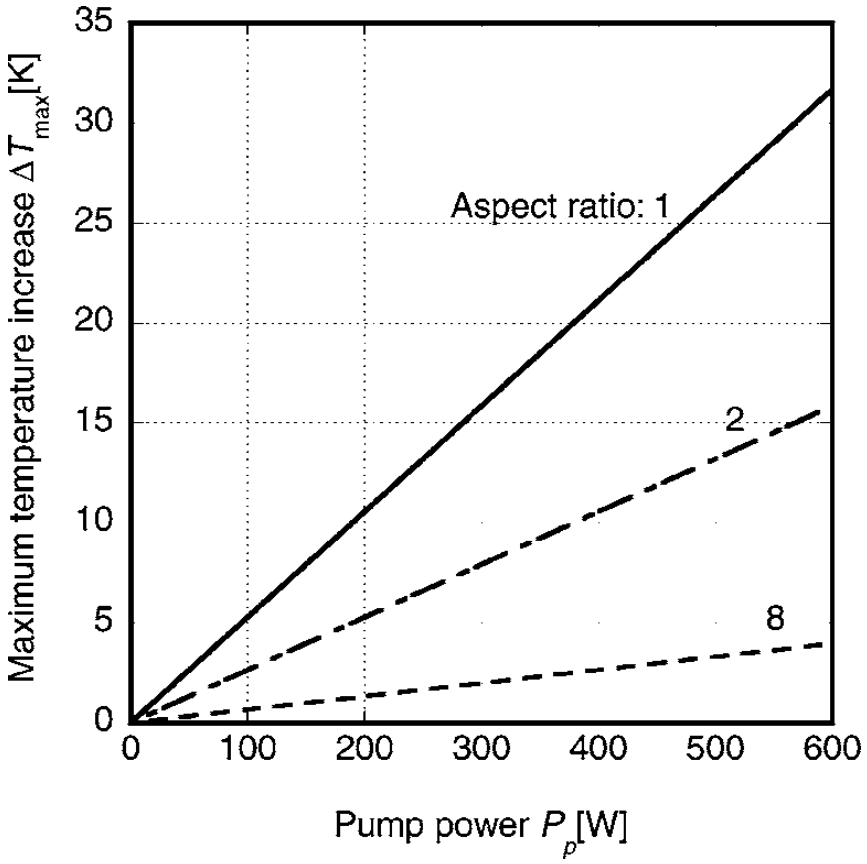

Figure 4: Calculated maximum temperature increase $\Delta T_{\max}$ in a microthickness YAG:Yb^{3+} slab laser as a function of pump power P_p for various width (w) to thickness (d) aspect ratios. The slab cross section $S = w \cdot d$ was assumed to be 2 mm [22]. (Reprinted with permission from K. Sueda, H. Takahashi, S. Kawato, T. Kobayashi, "High-efficiency laser-diodes-pumped microthickness Yb:$Y_3Al_5O_{12}$ slab laser," Applied Physics Letters vol. 87, 151110, Copyright 2005, American Institute of Physics).

C. Grivas, "*Optically pumped planar waveguide lasers Part I: fundamentals and fabrication techniques*"

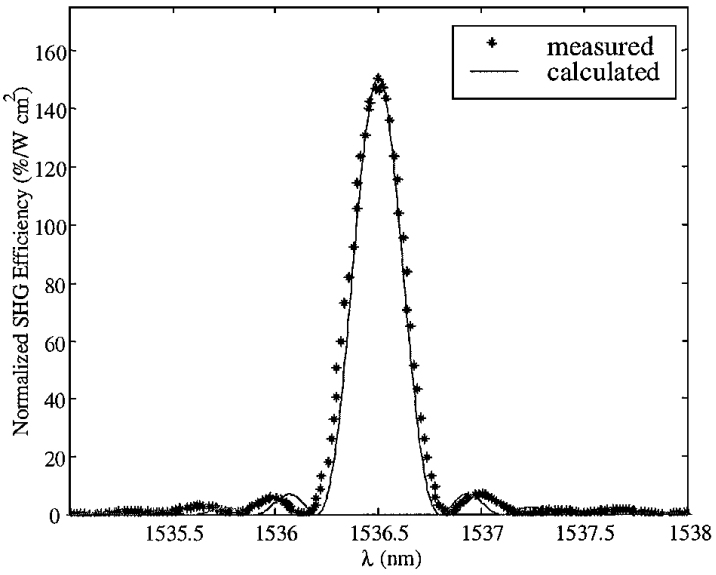

Figure 5: Measured and calculated cw SHG tuning curve for a 3.3-cm-long $LiNbO_3$ waveguide, indicating a peak normalized conversion efficiency of approximately $150\%/W \cdot cm^2$. The nearly ideal $sinc^2$ shape of the curve suggests that phase matching is maintained throughout the device length [36]. (Reprinted with permission from Optics Letters, K. R. Parameswaran, R. K. Kurz, J. R. Kurz, R. V. Roussev, M. M. Fejer, M. Fujimura, "Highly efficient second-harmonic generation in buried waveguides formed by annealed and reverse proton exchange in periodically poled lithium niobate," vol. 27, pp. 179-181, © 2002 Optical Society of America).

C. Grivas, "*Optically pumped planar waveguide lasers Part I: fundamentals and fabrication techniques*"

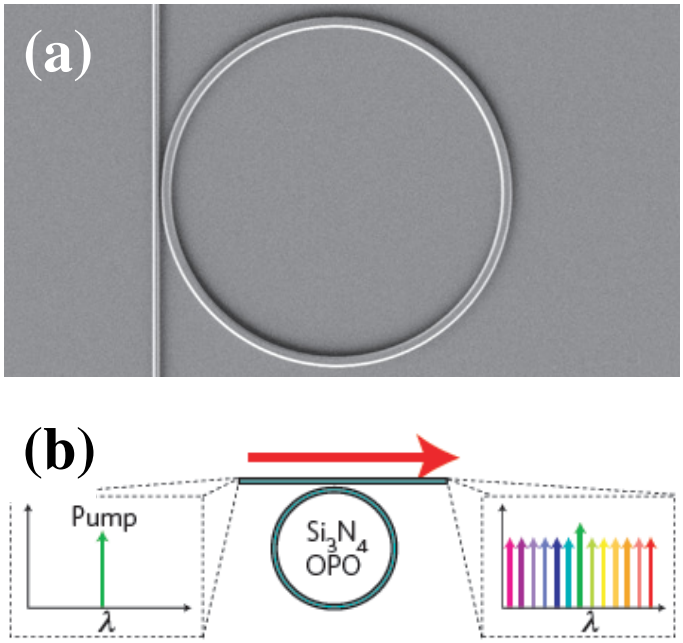

Figure 6: a) Scanning electron microscope (SEM) micrograph of an on-chip OPO based on a silicon nitride (Si_3N_4) microring resonator coupled to a bus waveguide. b) Optical parametric oscillation leading to emission at numerous precisely defined wavelengths was achieved in this device by tuning the emission wavelength of the pump laser to the resonance of the microring [37]. (Reprinted by permission from Macmillan Publishers Ltd: Nature Photonics, www.nature.com/nphoton/index.html, J. S. Levy, A. Gondarenko, M. A. Foster, A. C. Turner-Foster, A. L. Gaeta, M. Lipson, "CMOS-compatible multiple-wavelength oscillator for on-chip optical interconnects," vol. 4, pp. 37-40, Copyright 2009)

C. Grivas, "*Optically pumped planar waveguide lasers Part I: fundamentals and fabrication techniques*"

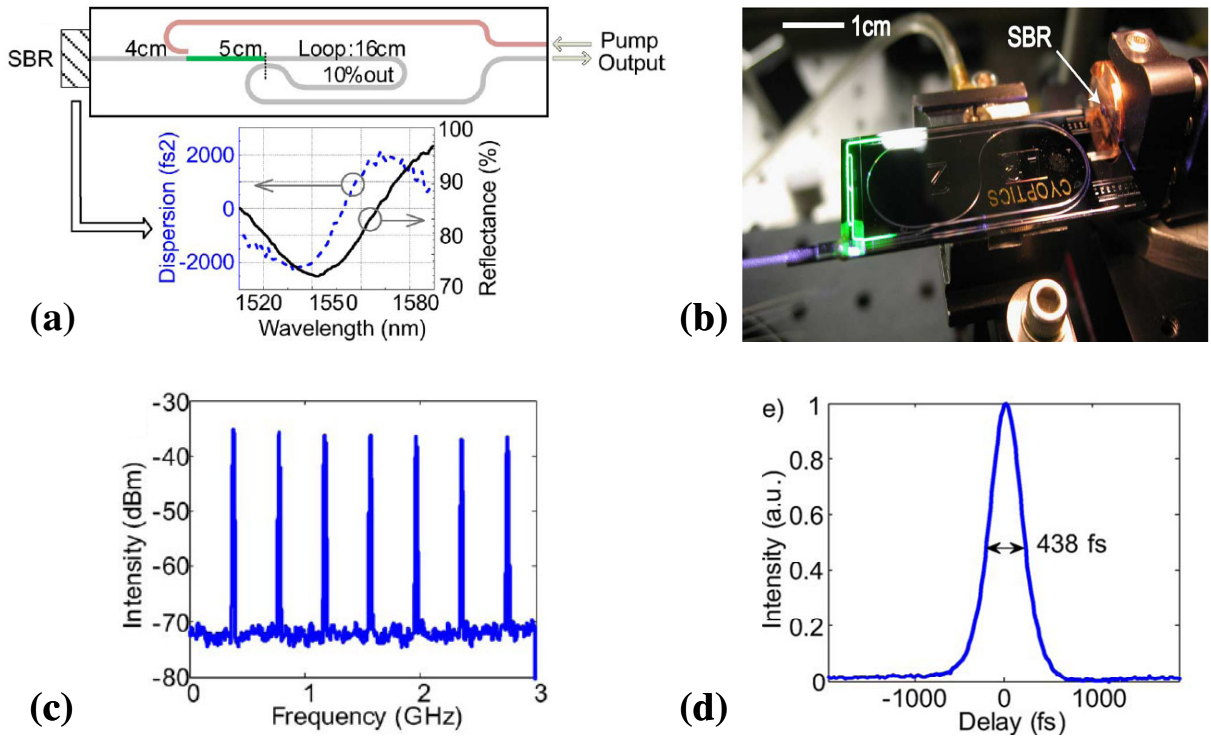

Figure 7: (a) Layout of the cavity of an integrated femtosecond waveguide laser consisting of two sections: a 5-cm (Er)-doped alumino–silicate waveguide with group-velocity dispersion (GVD) of 30 fs^2/mm, and a 20-cm of phosphorous-doped silica waveguide with GVD of -25 fs^2/mm. The latter is used to obtain net anomalous intracavity dispersion for soliton mode-locking operation. The inset shows the reflection and dispersion spectra of the saturable Bragg reflector (SBR) element that was used to start the mode-locking and stabilize the soliton. (b) Picture of the laser setup. (c) RF spectrum (3-GHz span, 10-MHz resolution), indicating an operating repetition rate of 394 MHz. (d) Background free autocorrelation trace showing that the pulses produced had a duration of 438 fs [44]. (Reprinted with permission from IEEE Photonics Technology Letters, vol. 21, H. Byun, D. Pudo, S. Frolov, A. Hanjani, J. Shmulovich, E. P. Ippen, F. X. Kärtner, "Integrated Low-Jitter 400-MHz Femtosecond Waveguide Laser," pp. 763-765, © 2009 IEEE).

C. Grivas, "*Optically pumped planar waveguide lasers Part I: fundamentals and fabrication techniques*"

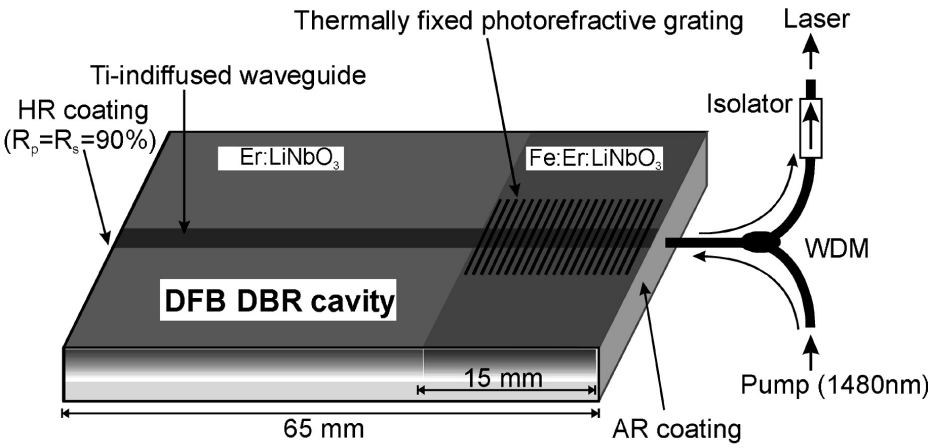

Figure 8: Schematic of an integrated DFB–DBR coupled cavity laser based on a single-mode channel waveguide. It was fabricated by thermal indiffusion of titanium ions into an Er:$LiNbO_3$ section (DBR laser) and an Er:Fe:$LiNbO_3$ section (DFB laser) of the same crystal. The abbreviations AR and WDM stand for antireflection and wavelength division demultiplexer, respectively [46]. (Reprinted with permission from Optics Letters, B. K. Das, R. Ricken, V. Quiring, H. Suche, W. Sohler, "Distributed feedback distributed Bragg reflector coupled cavity laser with a Ti:(Fe:)Er:$LiNbO_3$ waveguide," vol. 29, pp. 165-167, © 2004 Optical Society of America).

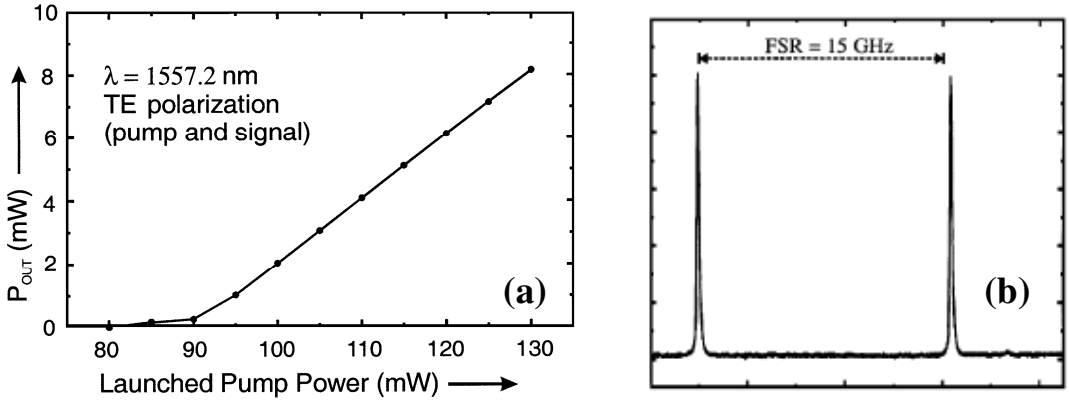

Figure 9: (a) Output power as a function of launched pump power for the Ti:Er:$LiNbO_3$ waveguide laser with the integrated DFB–DBR coupled cavity shown in Fig. 8. (b) Single-frequency emission of one DFB mode in resonance with one DBR cavity mode. FSR=15 GHz is the free spectral range of the Fabry–Perot spectrum analyzer used to record the spectrum [46]. (Reprinted with permission from Optics Letters, B. K. Das, R. Ricken, V. Quiring, H. Suche, W. Sohler, "Distributed feedback distributed Bragg reflector coupled cavity laser with a Ti:(Fe:)Er:$LiNbO_3$ waveguide," vol. 29, pp. 165-167, © 2004 Optical Society of America).

C. Grivas, "*Optically pumped planar waveguide lasers Part I: fundamentals and fabrication techniques*"

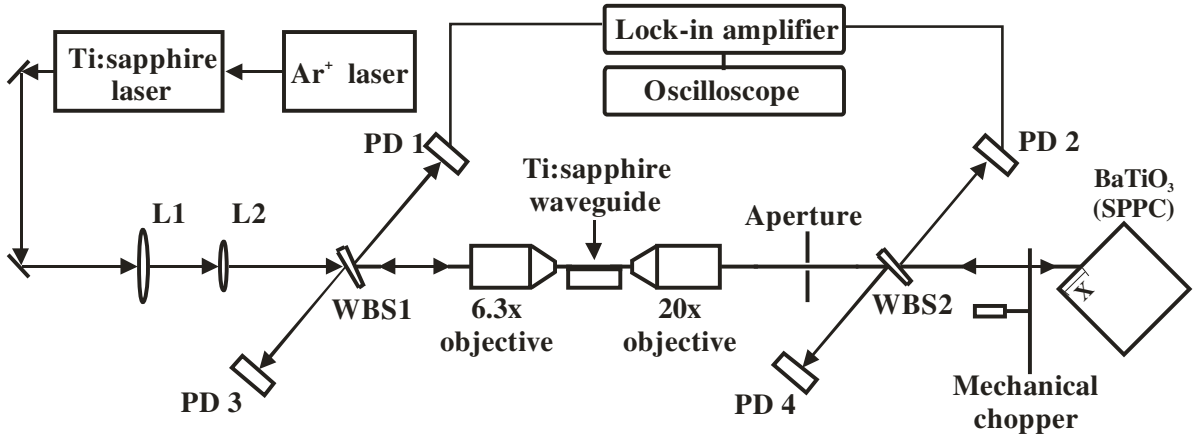

Figure 10: Experimental set-up for loss measurements in Ti:sapphire rib waveguides using the SPPC technique. In this arrangement, L1 and L2, are a pair of cylindrical lenses for pump-beam shaping, WBS 1, 2 are wedged beam splitters and PD 3, 4 and PD 1, 2 are photodiodes for detection of the incident and phase-conjugate signals before and after their passing through the rib waveguides, respectively [58].

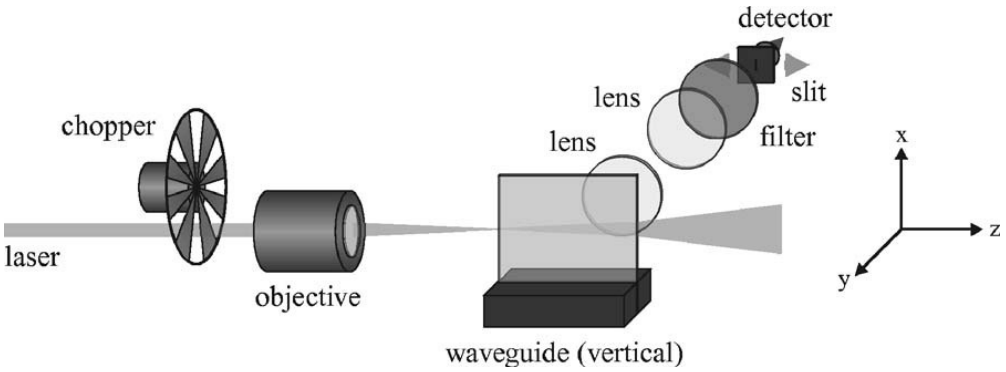

Figure 11: Typical arrangement for loss measurements in active waveguides using the fluorescence imaging technique. The filter shown in the set-up is employed to block the excitation light and in combination with a lock-in amplifier it ensures that only the fluorescence light is detected [62]. (Reprinted with permission from Journal of Optical Society of America B, A. Kahn,Y. Kuzminykh, H. Scheife, G. Huber, "Nondestructive measurement of the propagation losses in active planar waveguides," vol. 24, pp. 1571-1574, © 2007 Optical Society of America).

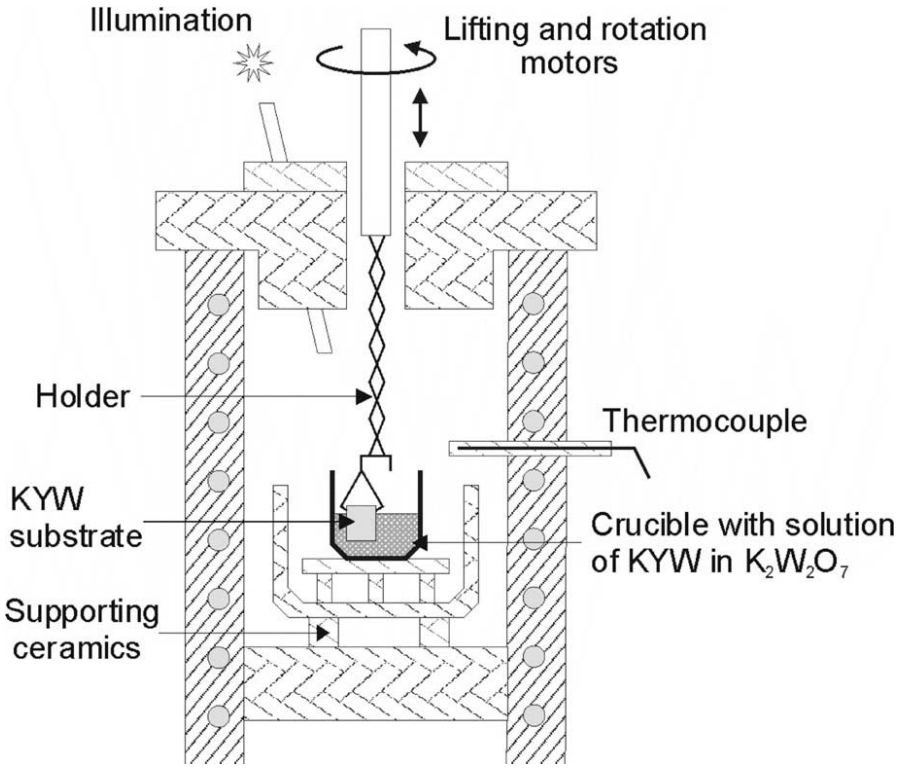

Figure 12: Schematic of a LPE arrangement used for growth of monoclinic double tungstate waveguide layers, in particular $KY(WO_4)$ [65]. (Reprinted with permission from IEEE Journal of Selected Topics in Quantum Electronics, vol. 13, M. Pollnau, Y. E. Romanyuk, F. Gardillou, C. N. Borca, U. Griebner, S. Rivier, V. Petrov, "Double Tungstate Lasers: From Bulk Toward On-Chip Integrated Waveguide Devices," pp. 661-671 © 2007 IEEE).

C. Grivas, "*Optically pumped planar waveguide lasers Part I: fundamentals and fabrication techniques*"

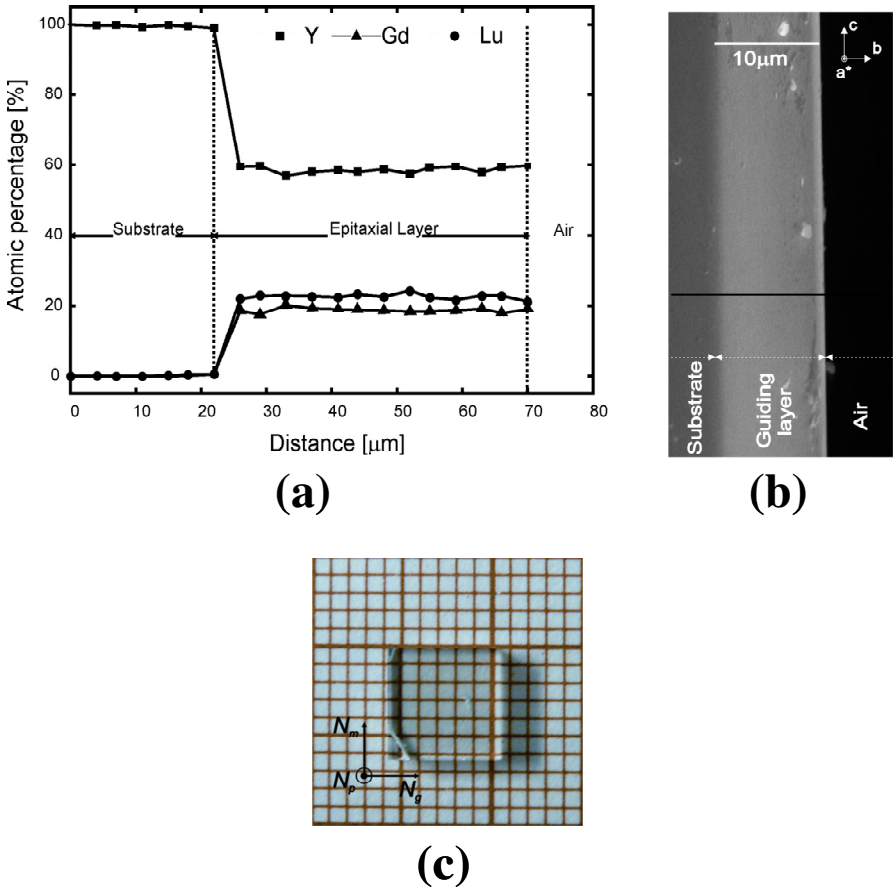

Figure 13: Lattice-matched $KY_{0.59}Gd_{0.19}Lu_{0.22}(WO_4)_2$ layers grown on $KY(WO_4)_2$ substrates: (a) scheme of the atomic percentage of Y, Gd and Lu across the substrate and the epitaxial layer as calculated from the EPMA results. Optimization of the relative concentrations of Y, Gd, and Lu is critical for achieving lattice-matched growth. (b) ESEM picture of a $KY_{0.59}Gd_{0.19}Lu_{0.22}(WO_4)_2$/ $KY(WO_4)_2$ interface obtained using backscattered electrons, and (c) photograph of the planar $KY_{0.59}Gd_{0.19}Lu_{0.22}(WO_4)_2/KY(WO_4)_2$ structure [67]. (Reprinted with permission from Crystal Growth and Design, W. Bolaňos, J. J. Carvajal, M. C. Pujol, X. Mateos, G. Lifante, M. Aguiló, F. Díaz, "Epitaxial Growth of Lattice Matched KY_{1-x-y} $Gd_xLu_y(WO_4)_2$ Thin Films on $KY(WO_4)_2$ Substrates for Waveguiding Applications," vol. 9, pp. 3525-3531, Copyright 2009, American Chemical Society).

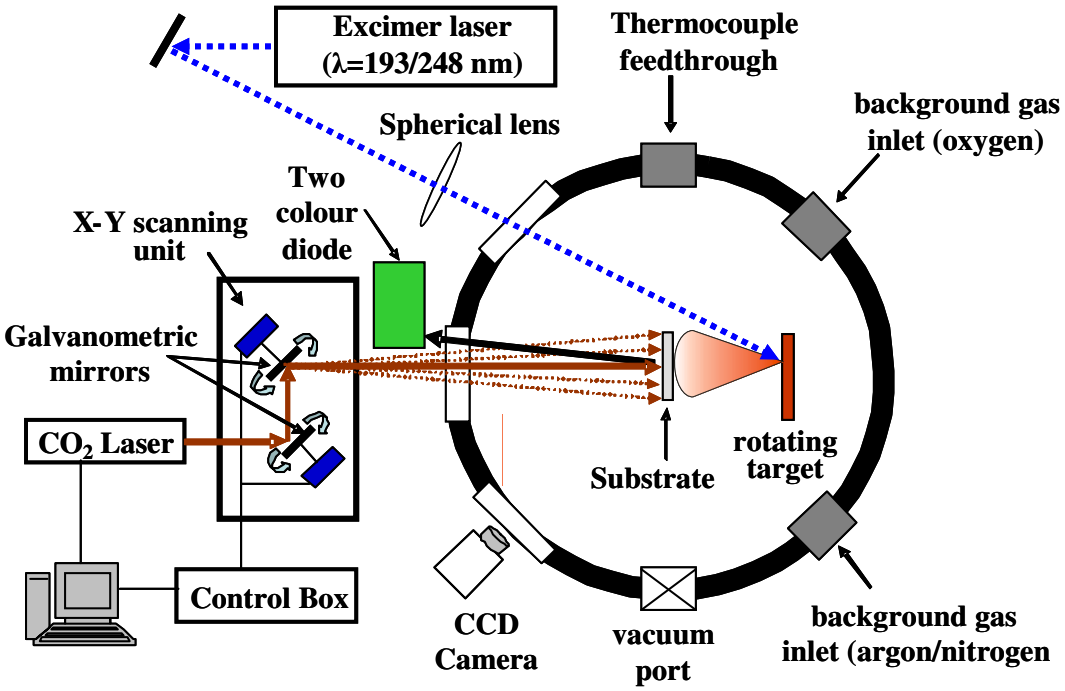

Figure 14: PLD configuration for growth of Ti:sapphire and doped GGG:Nd^{3+} waveguide layers. To prevent contamination through desorption from the walls of the vacuum chamber due to the high temperatures involved in the deposition process (~ 1000ºC), localized substrate heating was provided by scanning a 100-W CO_2 laser beam on the substrate [14, 102].

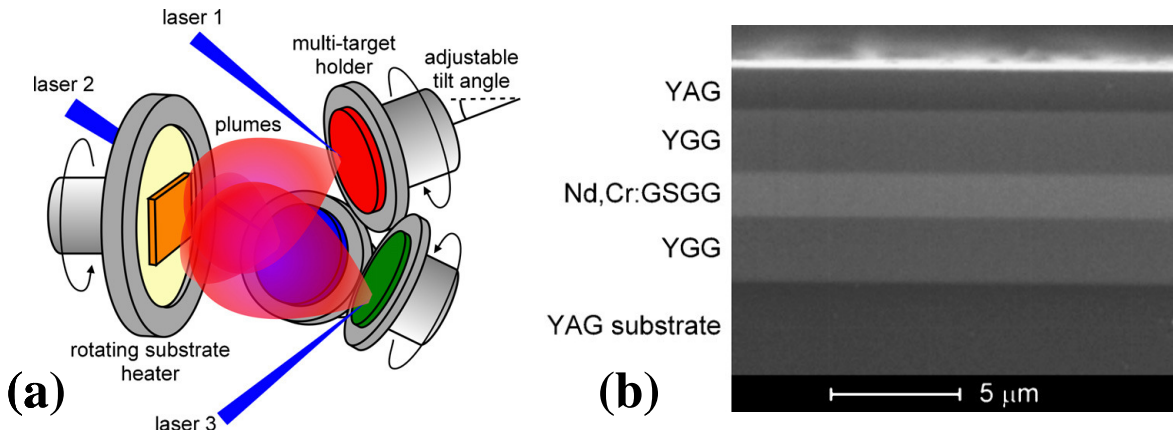

Figure 15: (a) Schematic of a target-substrate arrangement for combinatorial PLD experiments, comprising a rotating substrate heater and a three-beam, three-target assembly. (b) SEM micrograph of a 5-layer garnet crystal structure produced by combinatorial PLD [93]. (Reprinted from Applied Surface Science, 255, R. W. Eason, T. C. May-Smith, C. Grivas, M. S. B. Darby, D. P. Shepherd, R. Gazia, "Current state-of-the-art of pulsed laser deposition of optical waveguide structures: Existing capabilities and future trends," pp. 5199-5205, Copyright 2009, with permission from Elsevier).

C. Grivas, "*Optically pumped planar waveguide lasers Part I: fundamentals and fabrication techniques*"

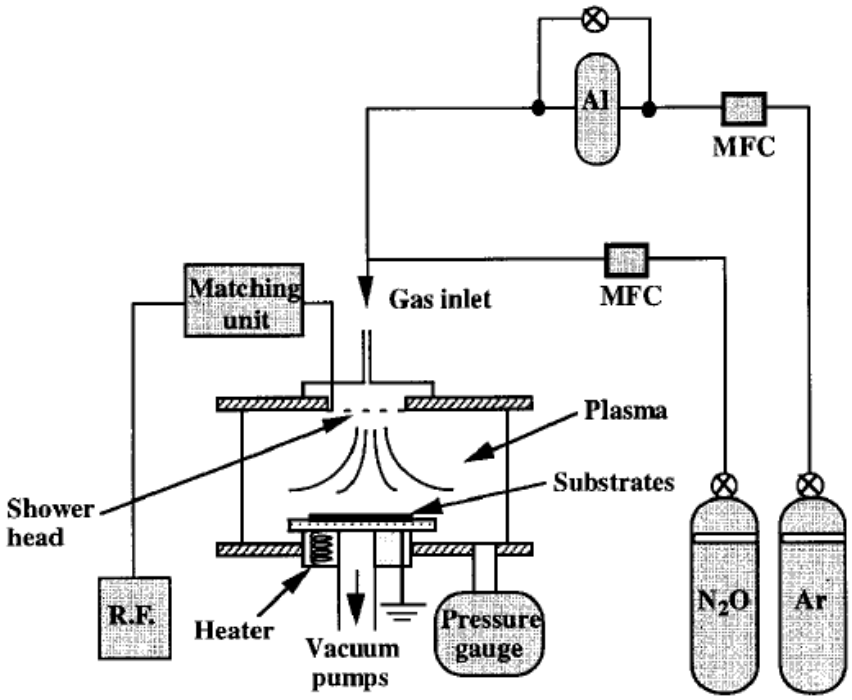

Figure 16: Schematic of a PECVD apparatus employed for deposition of Al_2O_3 films. A carrier gas (argon) was used to transport the precursor trimethyl-amine alane $(CH_3)_3NAlH_3$ (TMAA) to the reaction site, where it reacted with N_2O to produce a solid Al_2O_3 layer on a heated (300 ºC) substrate [133]. (With kind permission from Springer Science + Business Media: Applied Physics A, "Al_2O_3 thin films by plasma-enhanced chemical vapour deposition using trimethyl-amine alane (TMAA) as the Al precursor," vol. 65, 1997, pp. 469-475, C. E. Chryssou, C. W. Pitt, Fig . 1).

C. Grivas, "*Optically pumped planar waveguide lasers Part I: fundamentals and fabrication techniques*"

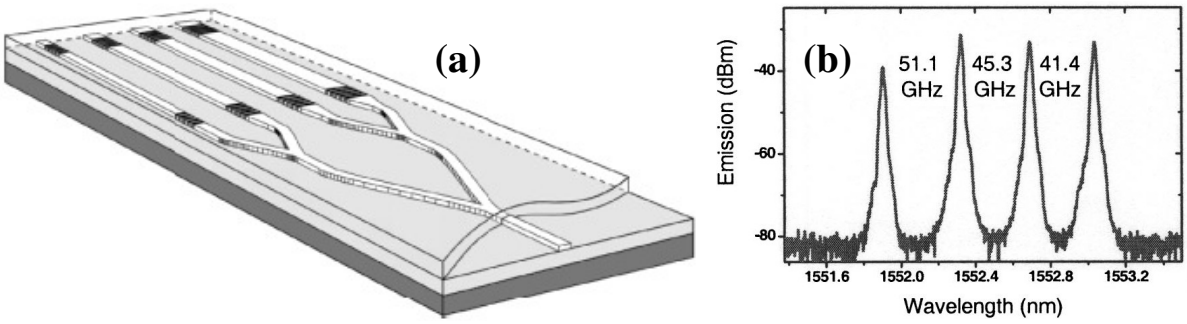

Figure 17: (a) Schematic of an array of four waveguide lasers based on channels with different widths, where one of the output sides is combined using Y splitters. The array was produced by a combination of PECVD and RIE, and a pair of gratings was inscribed over each channel by exposure to UV irradiation through a single phase mask. (b) A laser spectrum as obtained from the array, where the differences in lasing wavelengths indicated are entirely determined by the waveguide width [128]. (Reprinted with permission from: Optical Engineering, M. R. Poulsen, P. I. Borel, J. Fage-Pedersen, J. Hübner, M. Kristensen, J. H. Povlsen, K. Rottwitt, M. Svalgaard, W. Svendsen, "Advances in silica-based integrated optics," vol. 42 pp. 2821-2834, Copyright 2003, SPIE-International Society for Optical Engineering).

C. Grivas, "*Optically pumped planar waveguide lasers Part I: fundamentals and fabrication techniques*"

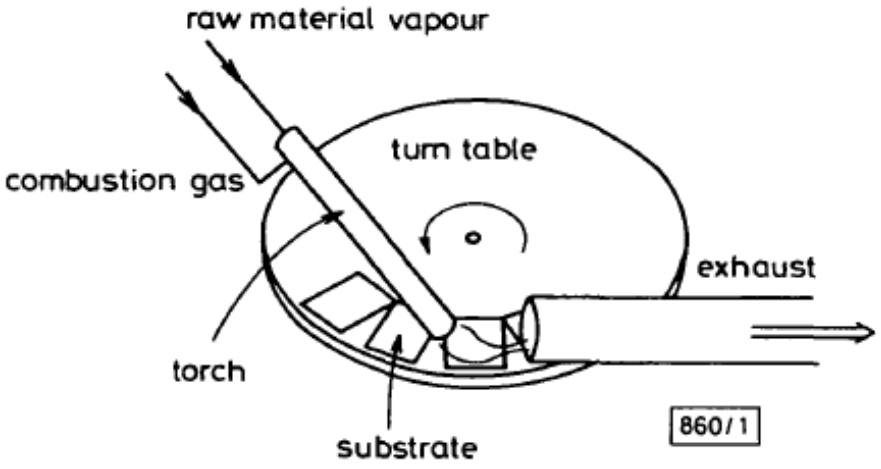

Figure 18: Typical set-up for FHD fabrication of planar optical waveguides. A mixture of vapour precursors is fed into an oxy/hydrogen torch and films are deposited on silica glass substrates placed on a turn-table [136]. (Reprinted with permission from Electronic Letters, vol. 19, M. Kawachi, M. Yasu, T. Edahiro, "Fabrication of SiO_2-TiO_2 glass planar optical waveguides by flame hydrolysis deposition," pp. 583-584, © 1983 IEEE).

C. Grivas, "*Optically pumped planar waveguide lasers Part I: fundamentals and fabrication techniques*"

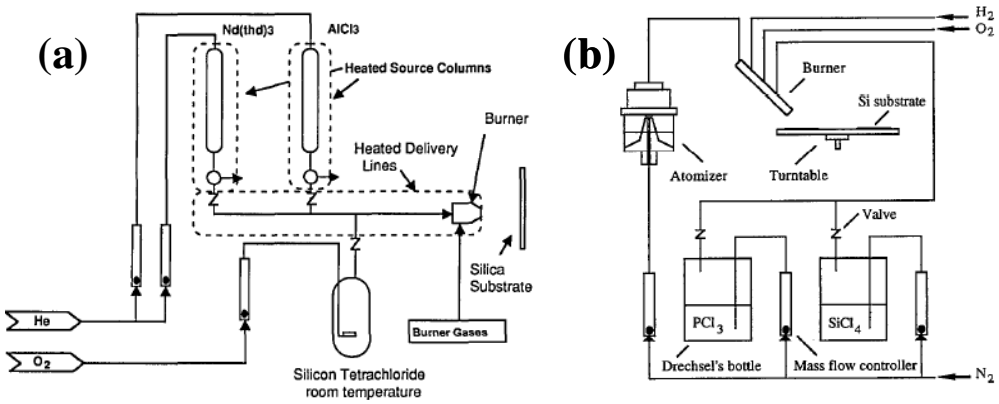

Figure 19: Schematic of FHD configurations used for deposition of: (a) Nd-doped silica layers with inclusions of Al_2O_3 using a vapour delivery system. The Nd-ion precursor is the high-vapour-pressure organic compound $Nd(thd)_3$ [138] (Reprinted with permission from Optics Letters, R. Tumminelli, E. Hakimi, J. Haavisto, "Integrated-optic Nd:glass laser fabricated by flame hydrolysis deposition using chelates," vol. 16, pp. 1098-1100, © 1991 Optical Society of America). (b) Nd- and Er-doped silica layers with inclusions of P_2O_5 using aerosol doping. The chlorides $SiCl_4$ and PCl_3 served as precursors of SiO_2 and P_2O_5, respectively, and nitrogen was used as a carrier gas to atomize the solution and deliver the resultant aerosol droplets to the burner [139]. (Reprinted with permission from: J. A. Bebbington, G. Barbarossa, J. R. Bonar, J. S. Aitchison, "Rare earth doped silica waveguides on Si fabricated by flame hydrolysis deposition and aerosol doping," Applied Physics Letters, vol. 62, pp. 337-339, (1993), Copyright 1993, American Institute of Physics).

C. Grivas, "*Optically pumped planar waveguide lasers Part I: fundamentals and fabrication techniques*"

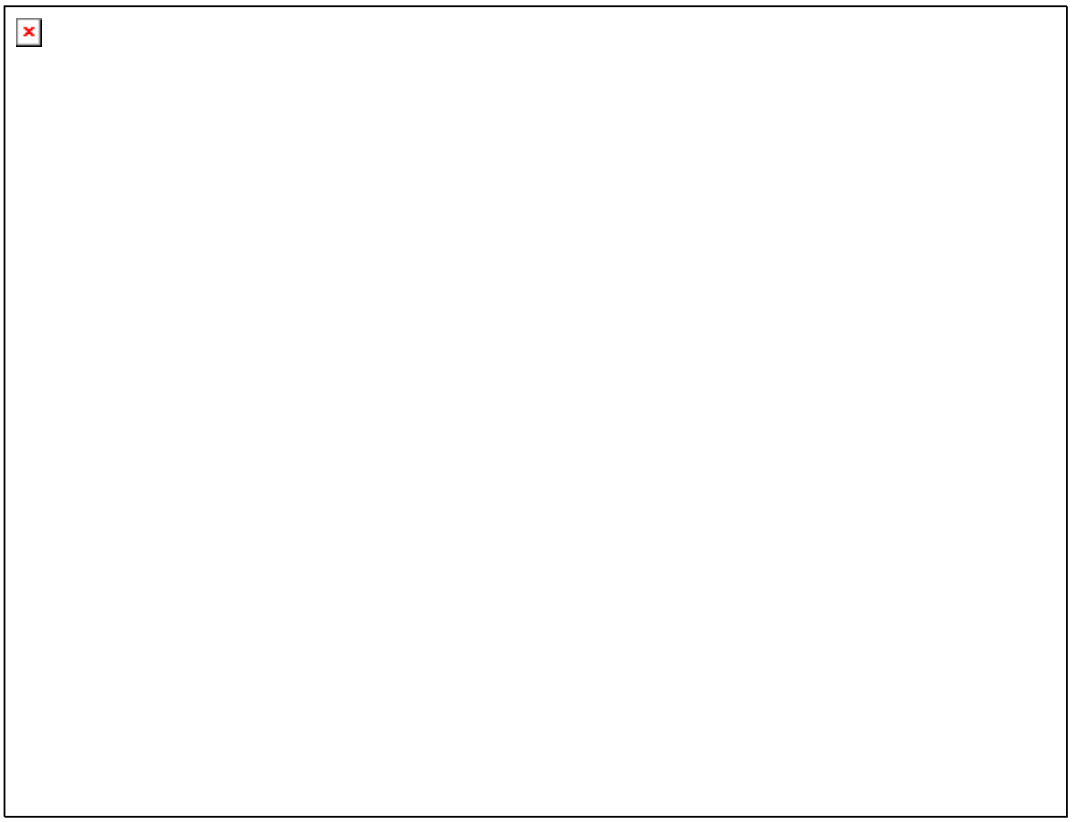

Figure 20: Schematic illustrating the high versatility of the sol–gel technique in terms of chemical processes involved in fabrication, nature of the precursor materials, and shape of the composite devices produced [151]. (Reprinted figure with permission from Journal of American Ceramic Society, S. Bhandarkar, "Sol-Gel Processing for Optical Communication Technology," vol. 87, pp.1180-1199, Copyright 2004, John Wiley and Sons).

C. Grivas, "*Optically pumped planar waveguide lasers Part I: fundamentals and fabrication techniques*"

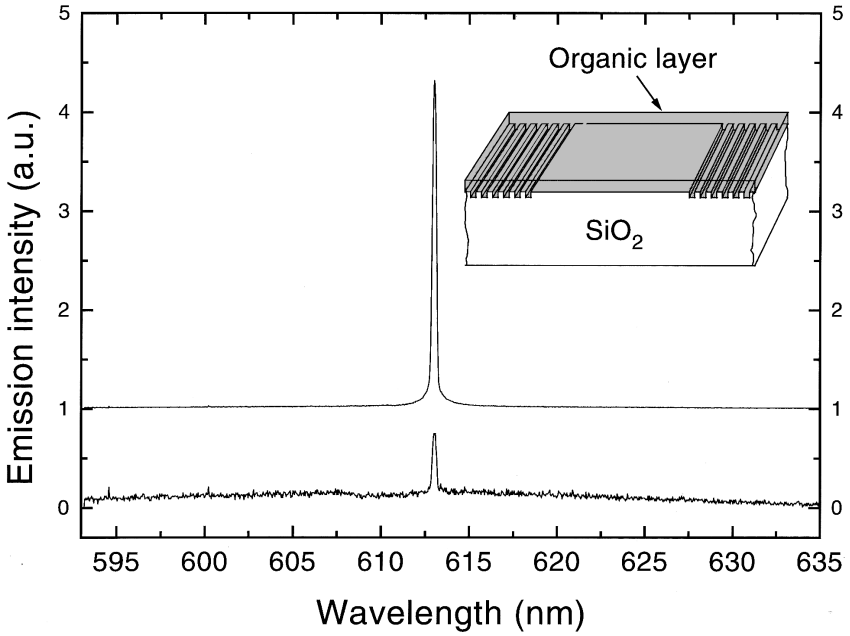

Figure 21: Laser emission spectra obtained from a DBR laser based on the organic semiconducting gain medium Alq_3:DCM2 by pumping with power densities of a 6 kW/cm^2 (bottom) and 20 kW/cm^2 (top). The inset shows the schematic of the DBR laser, which had a cavity length of 2 mm. The gratings were formed by etching the SiO_2 substrate; the gain medium was then deposited on the substrate by thermal sublimation [185]. (Reprinted with permission from: M. Berggren, A. Dodabalapur, R. E. Slusher, "Stimulated emission and lasing in dye-doped organic thin films with Forster transfer," Applied Physics Letters, vol. 71, pp. 2230-2232, Copyright 1997, American Institute of Physics).

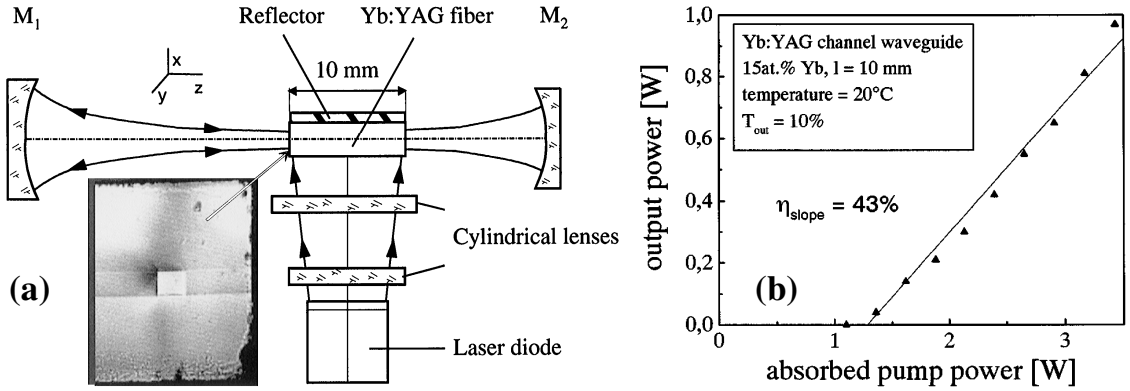

Figure 22: (a) Top view of the extended cavity of a diode side-pumped YAG:Yb^{3+} channel waveguide laser fabricated by diffusion bonding. A micrograph of the polished end face of the YAG:Yb^{3+} channel waveguide (cross section 100 x 80 μm^2) surrounded by a 300-µm-thick YAG cladding is also shown. (b) Output power from the YAG:Yb^{3+} channel waveguide laser as a function of absorbed pump power [217]. (Reprinted with permission from Optics Letters, U. Griebner, H. Schönnagel, "Stimulated emission and lasing in dye-doped organic thin films with Forster transfer," vol. 24, pp. 750-752, © 1999 Optical Society of America).

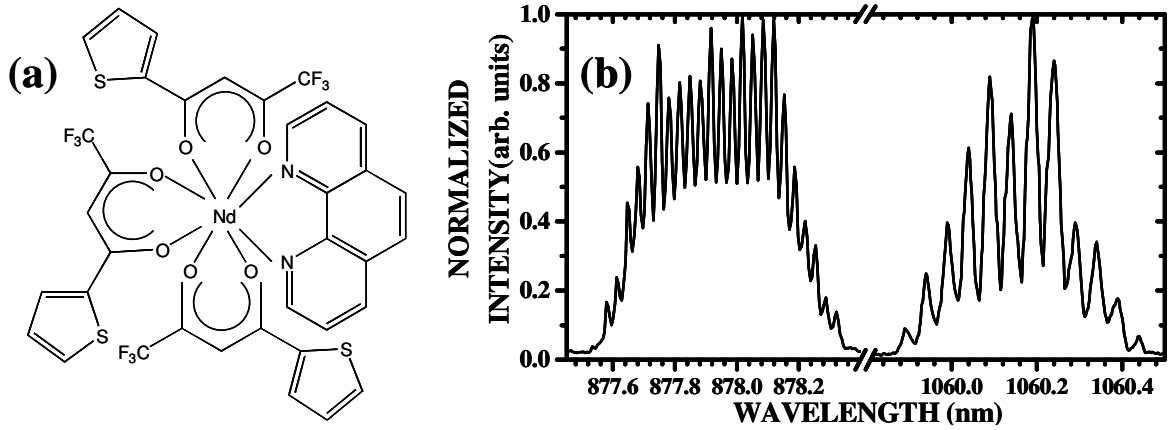

Figure 23: (a) Chemical structure of the $Nd(TTA)_3phen$ complex [220]. (b) Laser emission spectra obtained from a $Nd(TTA)_3phen$ complex-doped polymer channel waveguide for the quasi-three-level ($^4F_{3/2} \rightarrow {}^4I_{9/2}$) and four-level ($^4F_{3/2} \rightarrow {}^4I_{11/2}$) transitions near 878.0 nm and 1060.2 nm, respectively. The peaks in the bands correspond to longitudinal cavity modes [225].

C. Grivas, "*Optically pumped planar waveguide lasers Part I: fundamentals and fabrication techniques*"

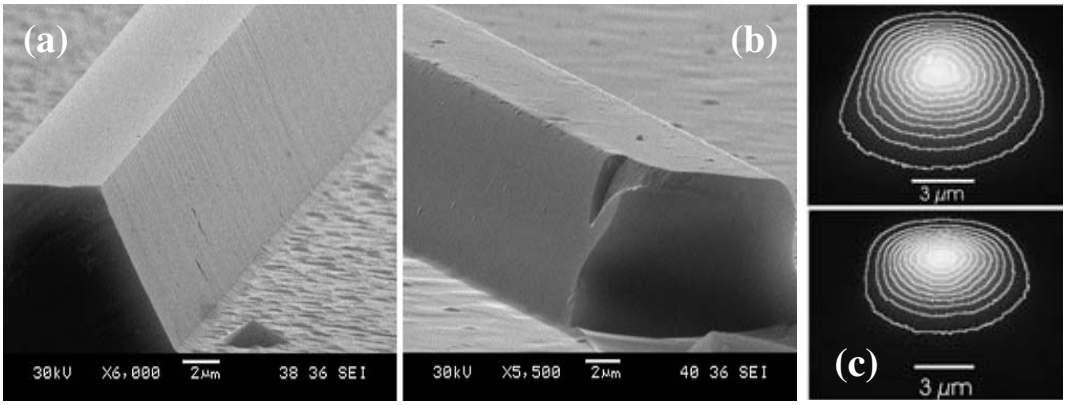

Figure 24: SEM micrographs of ridges of 6.5-μm height fabricated by wet etching in a $LiNBO_3$ crystal (a) before and (b) after their indiffusion with titanium ions at 1060ºC. As a result of the high temperatures used for the diffusion process the in-diffused ridge exhibits improved sidewall smoothness and a propagation loss as low as 0.08 $dB \cdot cm^{-1}$. (c) Mode distributions obtained from a ridge waveguide with 7-μm top width for the TE (top) and the TM-polarization (bottom), respectively [230]. (With kind permission from Springer Science + Business Media: Applied Physics B, "Low-loss ridge waveguides on lithium niobate fabricated by local diffusion doping with titanium," vol. 98, 2010, pp. 677-679, H. Hu, R. Ricken, W. Sohler, Figs. 2, 3)

C. Grivas, "*Optically pumped planar waveguide lasers Part I: fundamentals and fabrication techniques*"

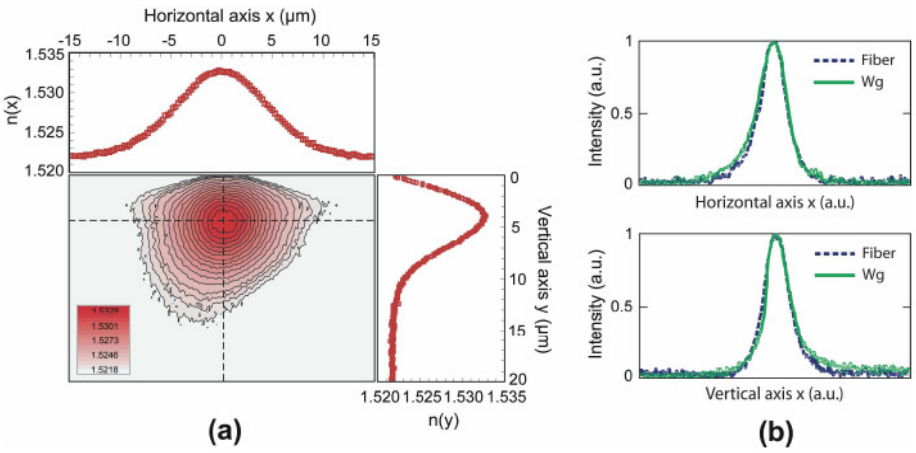

Figure 25: (a) Refractive index profile of a channel waveguide produced by Ag-Na ion exchange in an Er:Yb co-doped phosphate glass substrate and then buried by applying to the latter a transversal electric field. (b) Typical near-field mode profiles of a waveguide produced with this approach (green lines) compared to near-field mode profiles of a standard single-mode fiber at 1550 nm (blue lines) [255]. (Reprinted with permission from Optics Express, G. Della Valle, A. Festa, G. Sorbello, K. Ennser, C. Cassagnetes, D. Barbier, S. Taccheo, "Single mode and high power waveguide lasers fabricated by ion-exchange" vol. 16, pp. 12334-12341, © 2008 Optical Society of America).

C. Grivas, "*Optically pumped planar waveguide lasers Part I: fundamentals and fabrication techniques*"

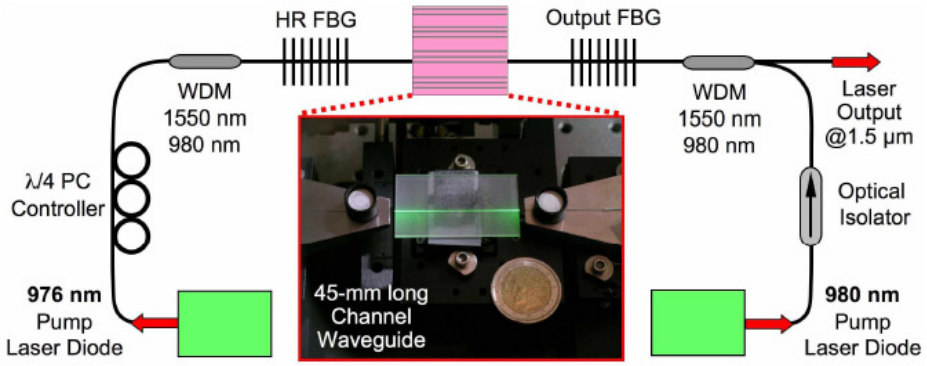

Figure 26: Set-up for high-power laser experiments of ion-exchanged Er:Yb-coped phosphate glass channel waveguides. The abbreviations PC, and HR FBG stand for polarization controller and high-reflective fiber Bragg grating, respectively. The picture at the center shows one of these waveguides with a length of 45-mm under double-end pumping through fibers (each containing a FBG) that were butt-coupled to its two end-faces [255]. (Reprinted with permission from Optics Express, G. Della Valle, A. Festa, G. Sorbello, K. Ennser, C. Cassagnetes, D. Barbier, S. Taccheo, "Single mode and high power waveguide lasers fabricated by ion-exchange" vol. 16, pp. 12334-12341, © 2008 Optical Society of America).

C. Grivas, "*Optically pumped planar waveguide lasers Part I: fundamentals and fabrication techniques*"

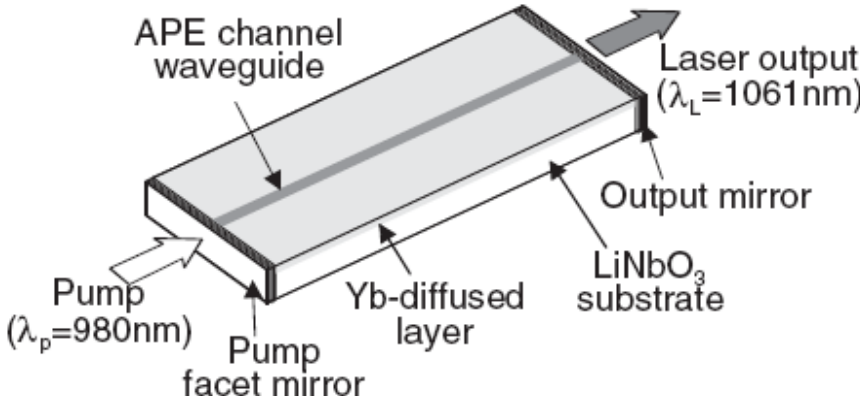

Figure 27: Schematic of a $LiNbO_3$:Yb^{3+} waveguide laser fabricated by annealed proton exchange in a slab waveguide produced by indiffusion of a $LiNbO_3$ crystal with Yb-ions [308]. (Reproduced with permission from Japanese Journal of Applied Physics: vol. 46, issue 8B, pp. 5447-5449, 2007. M. Fujimura, H. Tsuchimoto, T. Suhara, Copyright 2007, Japanese Society of Applied Physics).

C. Grivas, "*Optically pumped planar waveguide lasers Part I: fundamentals and fabrication techniques*"

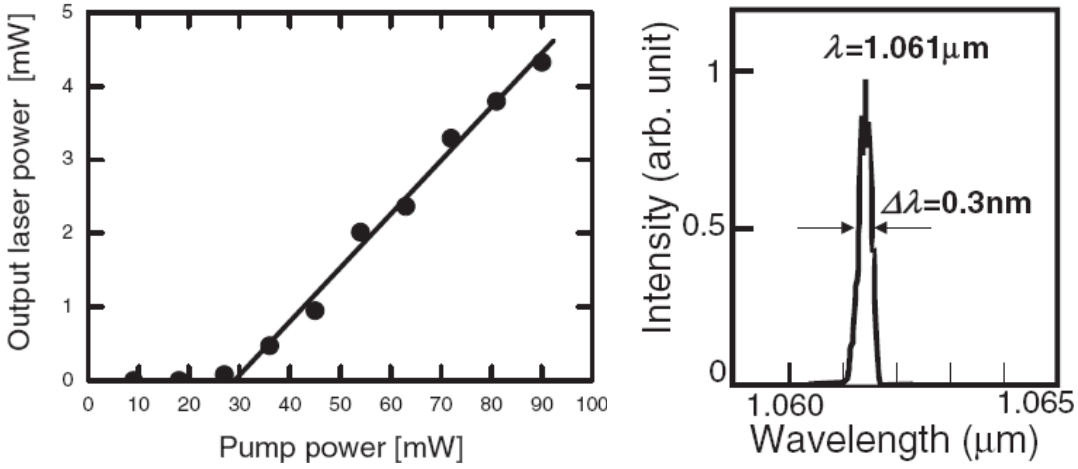

Figure 28: (a) Output power as a function of incident pump power, and (b) emission spectrum, both originating from a $LiNbO_3:Yb^{3+}$ channel waveguide laser produced by annealed proton exchange in a thermally indiffused $LiNbO_3:Yb^{3+}$ slab waveguide [308]. (Reproduced with permission from Japanese Journal of Applied Physics: vol. 46, issue 8B, pp. 5447-5449, M. Fujimura, H. Tsuchimoto, T. Suhara, Copyright 2007, Japanese Society of Applied Physics).

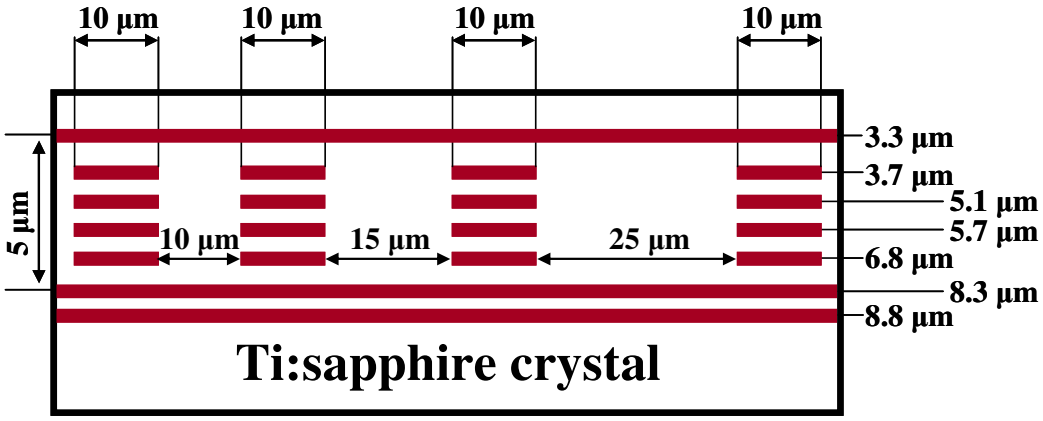

Figure 29: Schematic (not to scale) of the implantation design of channel waveguides in a Ti:sapphire crystal. The channels had different cross sections, namely 10 x 5 μm^2, 15 x 5 μm^2, and 25 x 5 μm^2, and were defined by optical barriers (indicated by red stripes) formed by multiple implants with different energies. The distances of these barriers from the top surface of the sample are also indicated [334].

C. Grivas, "*Optically pumped planar waveguide lasers Part I: fundamentals and fabrication techniques*"

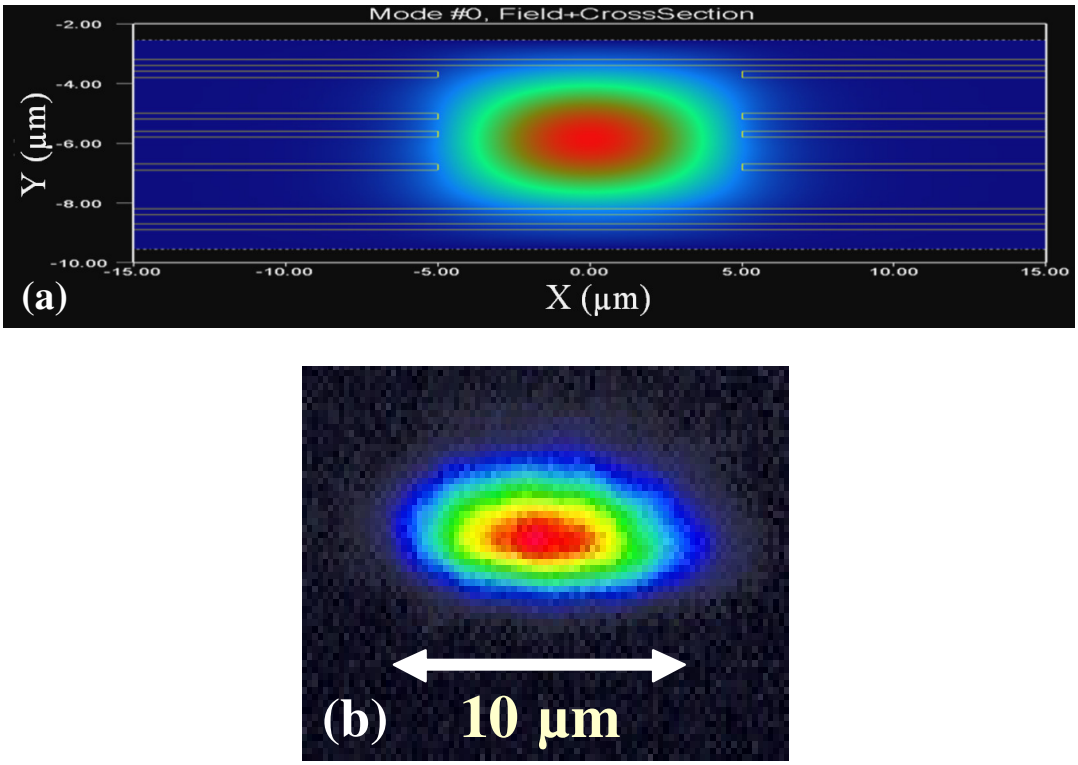

Figure 30: (a) Simulated and (b) measured fundamental transmission mode intensity profiles of the output from a 5-µm-deep and 10-µm-wide buried proton-implanted Ti:sapphire channel waveguide obtained by coupling a fundamental-mode laser beam of 800-nm wavelength [334].

C. Grivas, "*Optically pumped planar waveguide lasers Part I: fundamentals and fabrication techniques*"

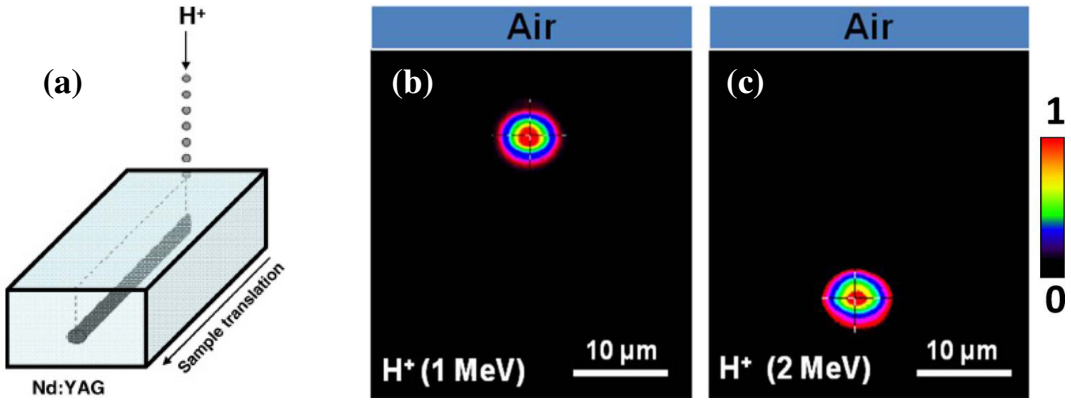

Figure 31: (a) Schematic of the waveguide writing process in YAG:Nd^{3+} crystals using the focused PBW technique. Also in the same figure, images of near-field intensity distributions of TE modes at 632 nm obtained from YAG:Nd^{3+} channel waveguides fabricated using an implantation dose of 2×10^{16} ions/cm^3 and energies of (b) 1 MeV and (c) 2 MeV (Reprinted figure with permission from [339]). (Reprinted with permission from Optics Letters, A. Benayas, D. Jaque, Y. Yao, F. Chen, A. A. Bettiol, A. Rodenas, A. K. Kar, "Microstructuring of Nd:YAG crystals by proton-beam writing," vol. 35, pp. 3898-3900, © 2010 Optical Society of America).

C. Grivas, "*Optically pumped planar waveguide lasers Part I: fundamentals and fabrication techniques*"

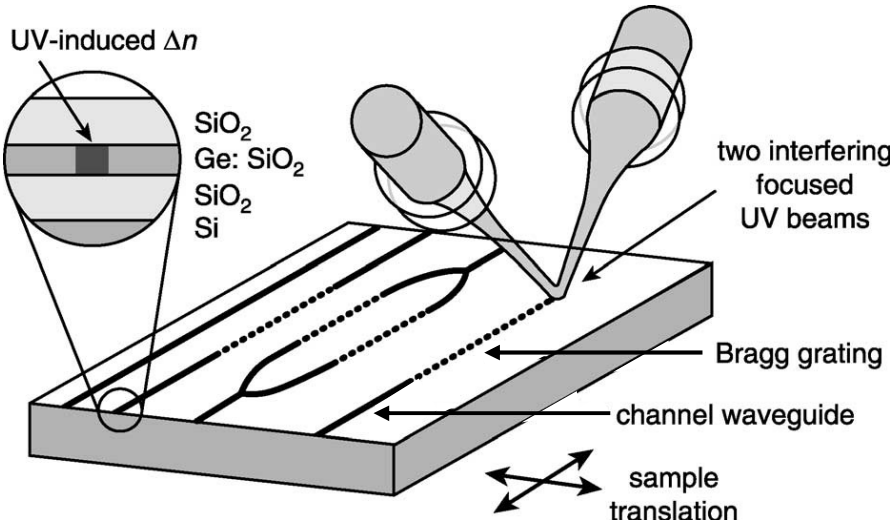

Figure 32: Schematic of the configuration used for one-step, simultaneous direct writing of channel waveguides and encoding of Bragg grating structures in glass substrates using cw UV irradiation. Bragg gratings of certain periodicity in the waveguide are formed by modulating the frequency of the UV light so as to match the scanning speed and their strength is modulated by slightly detuning the modulation frequency of the UV light [345]. (Reprinted with permission from IEE Proceedings Optoelectronics, vol. 151, G. D. Emmerson, C. B. E. Gawith, S. P. Watts, R. B. Williams, P. G. R. Smith, S. G. McMeekin, J. R. Bonar, R. I. Laming, "All-UV-written integrated planar Bragg gratings and channel waveguides through single-step direct grating writing," pp. 119-122, © 2004 IEEE).

C. Grivas, "*Optically pumped planar waveguide lasers Part I: fundamentals and fabrication techniques*"

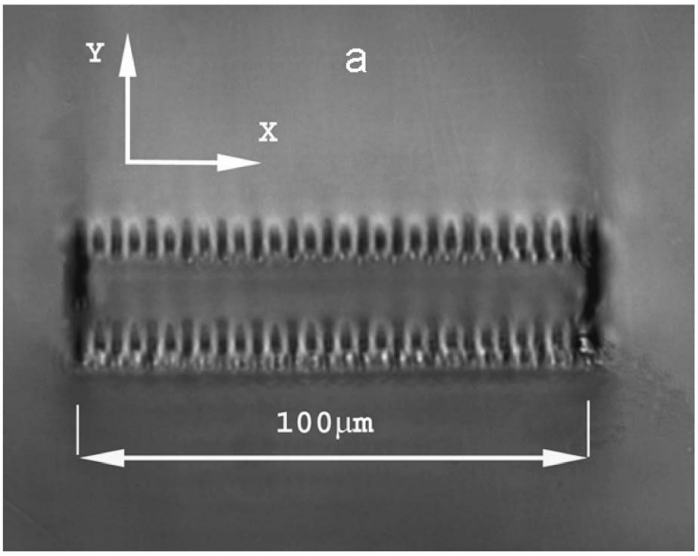

Figure 33: Picture of the endface of a depressed cladding waveguide produced by femtosecond (fs) laser writing in a YAG:Nd^{3+} crystal. The core, which has a size of 100 μm x 13 μm, was defined by fs-laser-written tracks, whose refractive index averaged across their cross section is smaller relative to that of the host crystal [369]. (Reprinted with permission from Optics Letters, A. G. Okhrimchuk, A.V. Shestakov, I. Khrushchev, J. Mitchell, "Depressed cladding, buried waveguide laser formed in a YAG:Nd^{3+} crystal by femtosecond laser writing," vol. 30, pp. 2248-2250, © 2005 Optical Society of America).

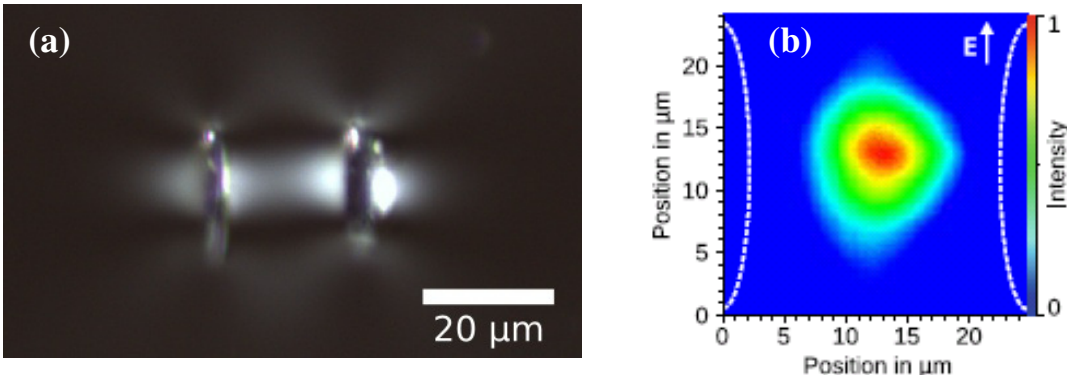

Figure 34: (a) Microscope image obtained under crossed polarizers of the cross section of a pair of tracks written in an undoped 45-µm-thick YAG crystal using femtosecond laser pulses. (b) Near-field image of the guided laser mode from a channel waveguide inscribed in a YAG:Nd^{3+} crystal as recorded by a CCD camera [370]. (With kind permission from Springer Science + Business Media: Applied Physics B, "Femtosecond laser written stress-induced Nd:$Y_3Al_5O_{12}$ (Nd:YAG) channel waveguide laser," vol. 97, 2009, pp. 251-255, J. Siebenmorgen, K. Petermann G. Huber, K. Rademaker, S. Nolte, A. Tünnermann, Figs. 4c, 10).

C. Grivas "*Optically pumped planar waveguide lasers Part I: fundamentals and fabrication techniques*"

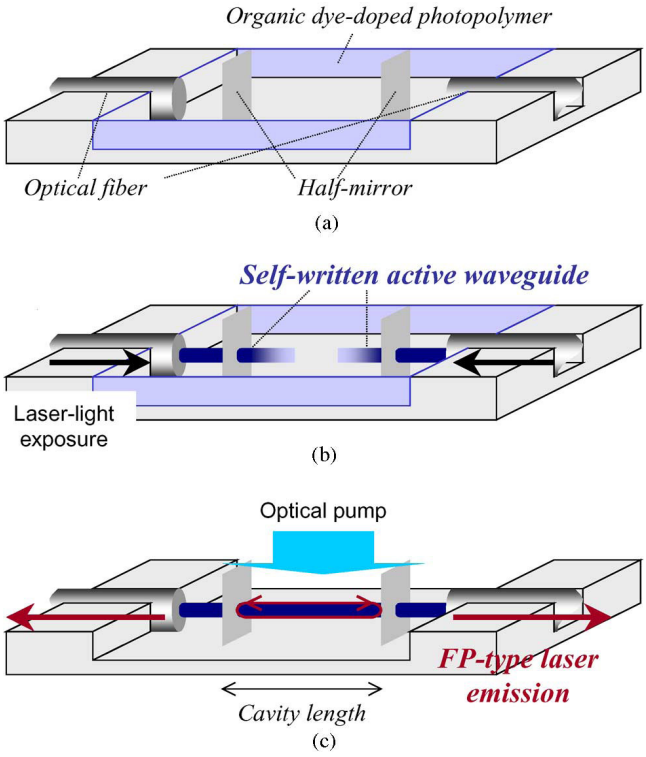

Figure 35: Schematic of the fabrication process and operation of a self-written channel waveguide laser with Fabry-Perot (FP) cavity. (a) The fibers used for writing are aligned and positioned within two grooves and the FP-cavity is formed by two the half-mirrors placed into the gap between fibers; the gain medium is then casted in-between these mirrors. (b) Channel waveguide writing in the dye-doped polymer by launching UV light through the two fiber tips. (c) Lasing operation under optical pumping; the uncured part of the gain medium was removed [383]. (Reprinted with permission from Journal of Lightwave Technology, vol. 27, K. Yamashita, M. Ito, E. Fukuzawa, H. Okada, K. Oe, "Device Parameter Analyses of Solid-State Organic Laser Made by Self-Written Active Waveguide Technique," pp. 4570-4574, © 2009 IEEE).

C. Grivas "*Optically pumped planar waveguide lasers Part I: fundamentals and fabrication techniques*"

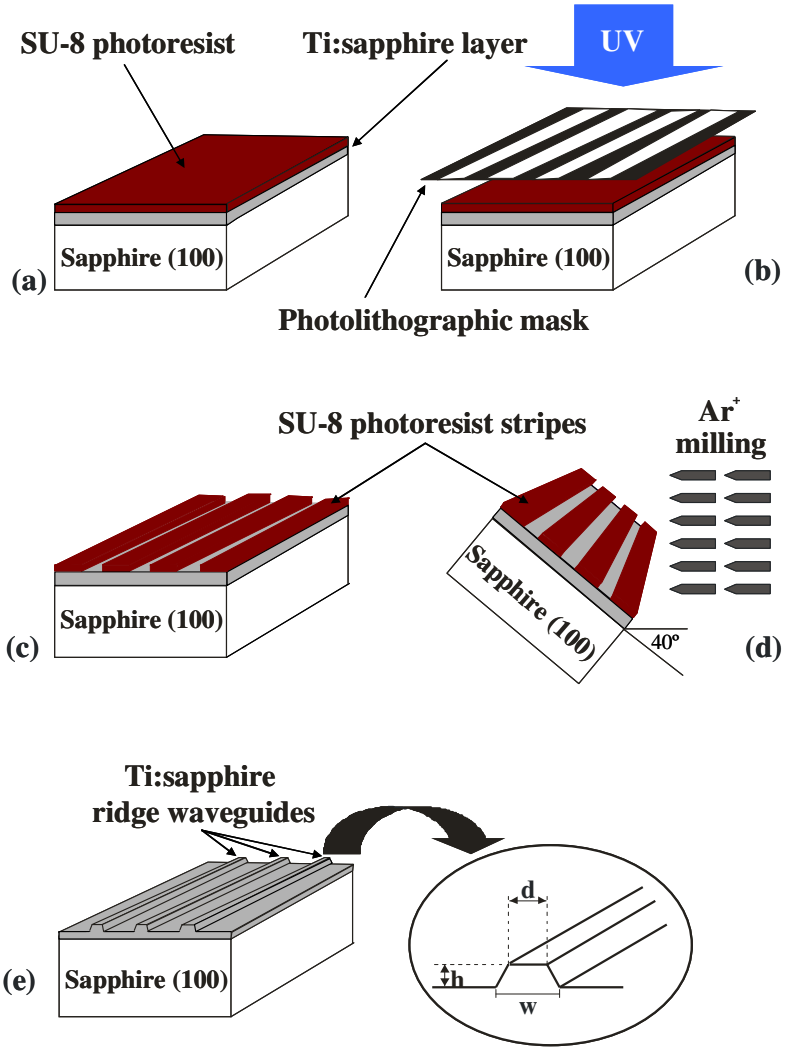

Figure 36: Schematic of the steps followed for fabrication of rib waveguides in PLD-deposited Ti:sapphire films using a combination of photolithography and IBE: (a) spin coating of the Ti:sapphire layer by a negative photoresist, (b) exposure to UV light through a photolithographic mask, (c) development of the photoresist to produce stripped photoresist patterns, (d) IBE of the uncovered Ti:sapphire surfaces, (e) removal of the photoresist remnants to obtain rib structures. The inset shows details of the resulting structures [58].

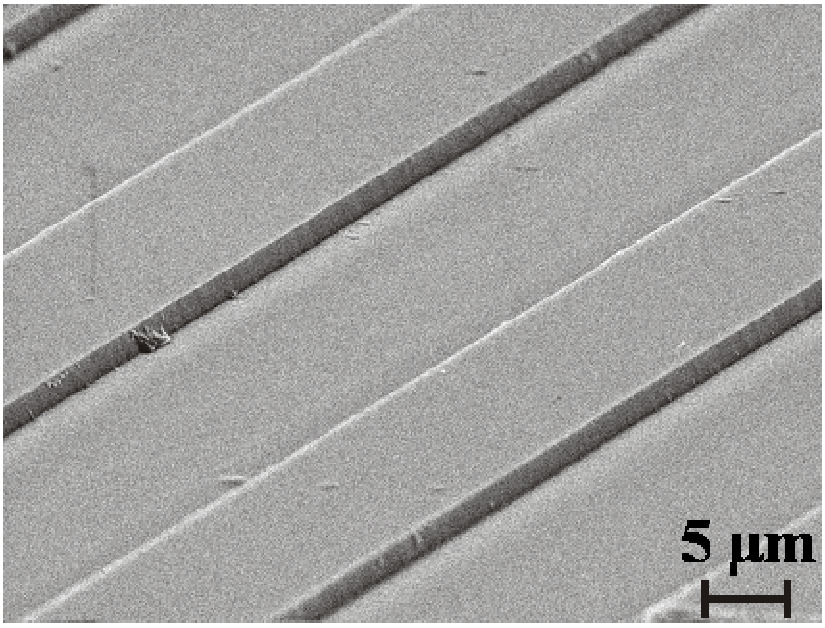

Figure 37: SEM image of Ar^+-beam-structured rib waveguides in a 10-µm-thick PLD-grown Ti:sapphire layer obtained following the process displayed in Fig. 36 [389].

C. Grivas, "*Optically pumped planar waveguide lasers Part I: fundamentals and fabrication techniques*"

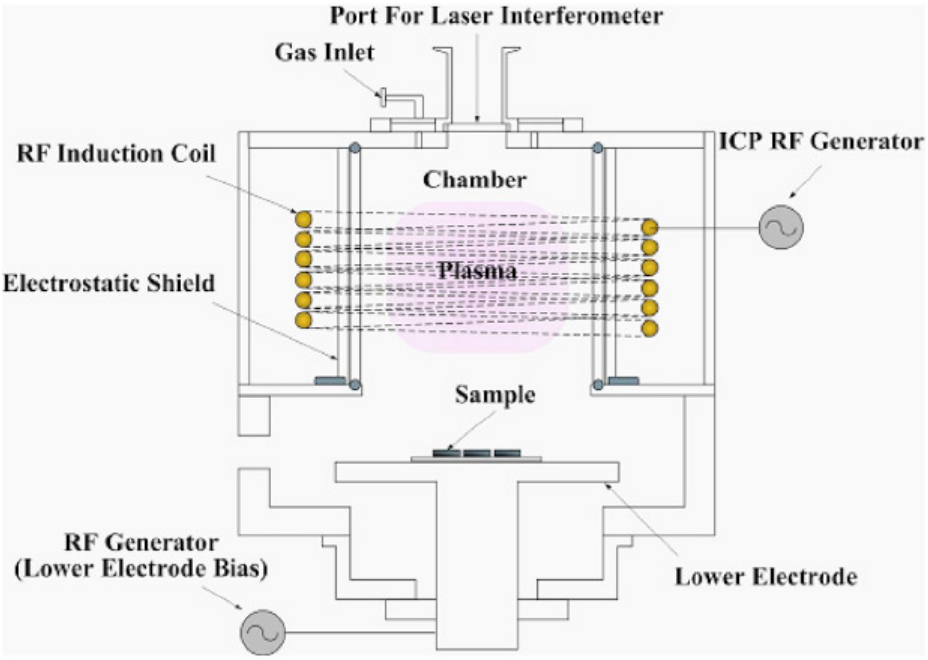

Figure 38: Schematic of a typical configuration for inductively coupled plasma (ICP) etching [390]. (Reprinted with permission from: Z. Ren, P. J. Heard, J. M. Marshall, P. A. Thomas, S. Yu, "Etching characteristics of $LiNbO_3$ in reactive ion etching and inductively coupled plasma" Journal of Applied Physics vol. 103, 034109, (2008), Copyright 2008, American Institute of Physics).

C. Grivas, "*Optically pumped planar waveguide lasers Part I: fundamentals and fabrication techniques*"

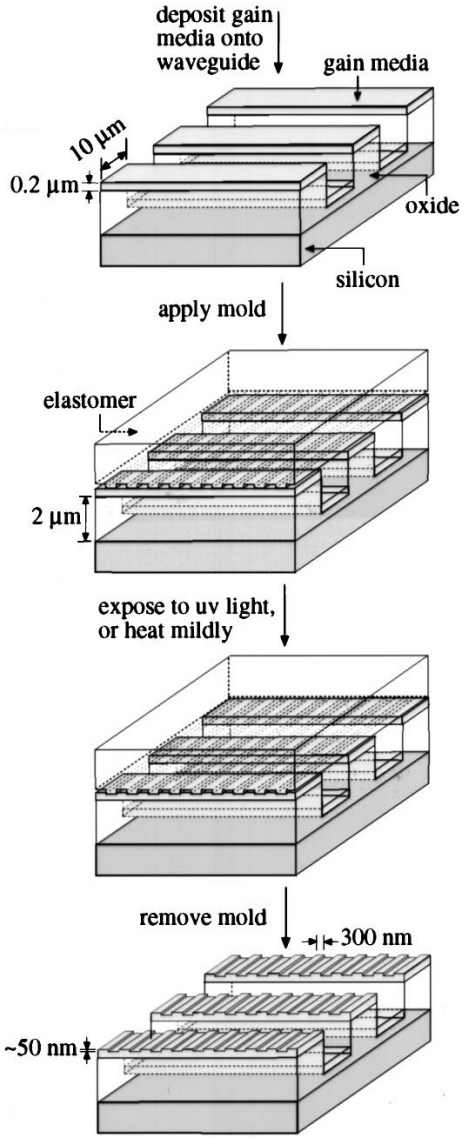

Figure 39: Schematic of the UV-NIL fabrication flow of Bragg gratings on top of Alq_3:DCM2 ridge waveguides to produce DFB resonators. An elastomeric mold transparent at 337 nm was used for imprinting [401]. (Reprinted with permission from: J. A. Rogers, M. Meier, A. Dodabalapur, E. J. Laskowski, M. A. Cappuzzo, "Distributed feedback ridge waveguide lasers fabricated by nanoscale printing and molding on nonplanar substrates," Applied Physics Letters vol. 74, pp. 3257-3259, (1999), Copyright 1999, American Institute of Physics).

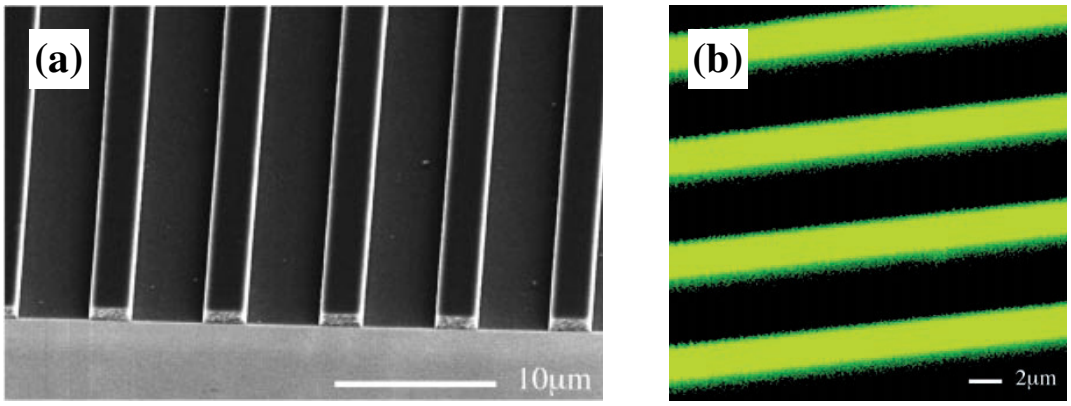

Figure 40: (a) SEM image of a waveguide array fabricated in a hexagonal mesostructured silica-$EO_{20}PO_{70}EO_{20}$ composite layer using MIMIC. (b) Laser scanning confocal microscopy image of a waveguide array produced by MIMIC in a Rh6G-doped mesostructured silica-$EO_{20}PO_{70}EO_{20}$ layer as obtained by pumping at 514 nm [178]. (From: P. Yang, G. Wirnsberger, H. C. Huang, S. R. Cordero, M. D. McGehee, B. Scott, T. Deng, G. M. Whitesides, B. F. Chmelka, S. K. Buratto, G. D. Stucky, "Mirrorless Lasing from Mesostructured Waveguides Patterned by Soft Lithography," Science vol. 287, 2000, pp. 465-467. Reprinted with permission from AAAS.)

.

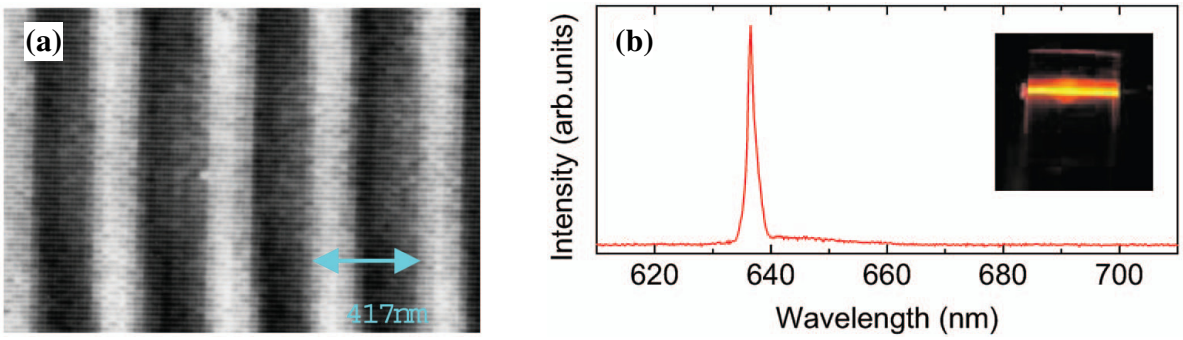

Figure 41: (a) SEM image of a DFB grating, imprinted by UV-NIL into a thin film of the UV-curable resin PAC-01-CL doped with the laser dye Rhodamine 610. (b) Laser spectrum obtained from the DFB waveguide laser by pulsed pumping at 337 nm with an optical pumping density of ~1.2 mJ/cm^2. The inset shows the DFB device under optical pumping [406]. (Reprinted with permission from: K. Yamashita, M. Arimatsu, M. Takayama, K. Oe, H. Yanagi, "Simple fabrication technique of distributed-feedback polymer laser by direct photonanoimprint lithography," Applied Physics Letters, vol. 92, 243306, (2008), Copyright 2008, American Institute of Physics).